City Research Online

City, University of London Institutional Repository

Citation: Monteiro, P. M. L. (2003). An investigation of tilt, decentration and defocusing errors in videokeratoscopy. (Unpublished Doctoral thesis, City, University of London)

This is the accepted version of the paper.

This version of the publication may differ from the final published version.

Permanent repository link: https://openaccess.city.ac.uk/id/eprint/30720/

Link to published version:

Copyright: City Research Online aims to make research outputs of City, University of London available to a wider audience. Copyright and Moral Rights remain with the author(s) and/or copyright holders. URLs from City Research Online may be freely distributed and linked to.

Reuse: Copies of full items can be used for personal research or study, educational, or not-for-profit purposes without prior permission or charge. Provided that the authors, title and full bibliographic details are credited, a hyperlink and/or URL is given for the original metadata page and the content is not changed in any way.

City Research Online: http://openaccess.city.ac.uk/ publications@city.ac.uk

An investigation of tilt, decentration and defocusing errors in videokeratoscopy

A Thesis

Submitted by

Pedro Miguel Lourenço Monteiro

For the degree of

Doctor of Philosophy

City University London

Department of Optometry and Visual Science

City University, London

April 2003

Contents

1 Introduction 24

1.1 Synopsis 25

2 Literature review 29

2.1 Keratoscopy 29

2.2 Faceplate design 30

2.3 Reconstruction algorithms for Placido disk based systems 32

2.3.1 Telecentric videokeratoscope principle 32

2.3.2 Gullstrand's algorithm 33

2.3.3 Wittenberg and Ludlam algorithm 34

2.3.4 Townsley and Ridge algorithm 35

2.3.5 El Hage's algorithm 35

2.3.6 Fry's algorithm 36

2.3.7 Doss et al algorithm 36

2.3.8 Klyce's algorithm 38

2.3.9 Spherical Biased 38

2.3.10 Edmund and Sjontoft algorithm 41

2.3.11 Wang et al algorithm 41

2.3.12 Mammone et al algorithm 42

2.3.13 Gersten et al algorithm 43

2.3.14 van Saarloos and Constable algorithm 43

2.3.15 Klein's algorithm 44

2.3.16 Andersen et al algorithm 45

2.3.17 Laskin and Puryayev algorithm 46

2.3.18 Halstead et al algorithm 46

2.3.19 Brenner's algorithm 47

2.3.20 Campbell's algorithm 48

2.4 Keratoscope alignment 49

2.5 Decentring, tilt and focus errors 50

3 Computer modelling of a videokeratoscope system 63

3.1 Faceplate Model 63

3.1.1 General properties of conics and conoids 63
3.1.2 Faceplate parameters 72
3.1.3 Object point selection on the faceplate 74
3.2 Reflecting surface 79
3.3 Axis systems 80
3.4 Decentring the reflecting surface 86
3.5 Tilt limits 87
3.6 Ray tracing equations for reflection 94
3.6.1 The parameter Δ 96
3.6.2 Special case: Initial ray perpendicular to the surface z axis (N=0) 101
3.6.3 Ray tracing with a tilted reflecting surface 104
3.7 Finding a transmitted ray through the faceplate pupil 105
3.7.1 Special case: Edge ray fails to intersect the pupil plane. 108
3.8 Pupil exploration in the meridional plane. 109
3.9 Pencil of rays from an object point, ray density 111
3.9.1 Retracing a pencil of rays with higher density 119
3.9.2 Special case: pencil of rays with central ray in the y axis direction. 120
3.9.3 The central ray 121
3.9.4 Limiting the pencil of rays from an object point 124
3.10 Central reference point of the ring images 125
3.11 Videokeratoscope alignment simulation 127
3.12 Focus 132
3.12.1 Focus parameters 132
3.12.2 Best focus for a centred reflecting surface 134
3.12.3 Best focus for a non-centred reflecting surface 137
3.13 Image relative irradiance 140
3.13.1 Image display on screen 141
3.13.2 Image magnification for a centred reflecting surface 143

3.13.3 Transforming screen coordinates to array elements for a centred reflecting surface. 145
3.13.4 Image magnification for a non-centred reflecting surface 146
3.13.5 Transforming screen coordinates to array elements for a non-centred reflecting surface. 154
3.13.6 Automatic ray density calculation 154
3.14 Ring edge detection 158
3.14.1 Centred reflecting surface 158
3.14.2 Non-centred reflecting surface 160
3.15 Reconstruction algorithms adaptation 162
3.15.1 Adaptation of the spherical biased algorithm. 162
3.15.2 Adaptation of the van Saarloos algorithm 163
3.16 Difference maps 174
4 Methods 177
4.1 Determination of best faceplate design 178
4.2 Influence of faceplate design on radius of curvature maps 181
4.3 Effect of reflecting surface decentration on r.c. maps 183
4.4 Effect of reflecting surface tilt on radius of curvature maps 183
5 Results 186
5.1 Determination of best faceplate design 186
5.2 Influence of faceplate design on radius of curvature maps 187
5.3 Effect of reflecting surface decentration on r.c. maps 195
5.4 Effect of reflecting surface tilt on radius of curvature maps 198
6 Discussion 203
6.1 Determination of best faceplate design 203
6.2 Influence of faceplate design on radius of curvature maps 204
6.3 Effect of reflecting surface decentration on r.c. maps 206
6.4 Effect of reflecting surface tilt on radius of curvature maps 207
7 Conclusions 209
8 Bibliography 212

List of tables

Table 3.1 - Values of the parameters e and p relating to the curvature change from the centre to the periphery of a conic arranged by curve type.

Table 3.2 - Expressions for the number of ray intersections (n_k) on a ring area (k) limited by radius R_k and R_{k-1} where $R_k=R_0+kaR_0$.

Table 5.1 - Minimum blur sums for the tested surfaces.

Table 5.2 - Frequency table for differences (Δ) from the smallest minimum blur sum.

List of figures

Figure 2.1 - Telecentric videokeratoscope principle. A stop is placed at the second principal focus of the objective lens to block all rays non-parallel to the optical axis. The height of the reflection point in analysis (h) will then be the same as the height of the image point in the image plane.

Figure 2.2 - Calibration graph for a 9 ring keratoscope for use with the spherical biased algorithm. If the inner edge of the 5th image ring is in analysis in a keratograph then the line corresponding to this edge is selected. Supposing that the ring mire image of this ring edge has an hemi-chord height of h_5 then the corresponding radius of curvature in the reflection area is R_5.

Figure 2.3 - Cone shaped faceplate of the Mastervue videokeratoscope. All rings are located on the faceplate inner surface except for ring 10. This ring is located in an inner cone with the same apical angle as the faceplate and with opposite base.

Figure 3.1 - Family of conics with the same apical radius of curvature. Each curve is associated with a p value (number displayed near each curve) that relates to the way the curvature changes from the centre to the periphery.

Figure 3.2 - Arc length of a circle between two z coordinates.

Figure 3.3 - Schematic representation of the model for a videokeratoscopy system used for this research. The main axis system is also represented along with the model parameters.

Figure 3.4 - Three-dimensional representation of the four faceplate geometries used. The pupil size limits the area of the surface. For a cone (**c**) and a conoid (**d**) a part of the surface is removed so that it starts at the specified pupil diameter.

Figure 3.5 - Intersection possibilities of a line with a conic curve.

Figure 3.6 - Section of a cylinder with light (*L*) and dark (*D*) rings defined by the intersection of lines at equal angle intervals. If a light ring falls in the corner, the cylinder base can be increased or decreased (long dashed sections) to avoid this situation keeping the number of rings constant.

Figure 3.7 - Definition of a point P in polar coordinates for the global (ρ,φ) and the image system (ρ,σ) and their relations.

Figure 3.8 – a) The axis system was rotated in the *xy* plane to define the tilt plane. The reflecting surface vertex was centred at the origin of *xyz* but wasn't rotated along with the axis. **b)** A new axis rotation was executed in the plane defined by $\hat{e}_r$ and $\hat{e}_\theta$. The unit vector $\hat{e}_\varphi$ remained on the *xy* plane. The surface was then rotated by θ and $\hat{e}_r$ is the rotated surface z-axis. **c)** This is the axis system developed for this research where $\hat{e}_\theta$ is represented just for reference. The unit vectors $\hat{e}_r$ and $\hat{e}_\theta$ have the same orientation as the middle figure but were represented oriented like *xyz* to allow a better understanding of their relations. The vectors $\hat{e}_x$ and $\hat{e}_y$ define a plane which is perpendicular to the plane defined by $\hat{e}_\theta$ and $\hat{e}_r$.

Figure 3.9 - Example of the application of the tilt system of axis to a centred ellipse with minor axis along the x-axis. **a)** The tilted plane is selected by a φ rotation of the axis in the *xy* plane. Once again it must be emphasised that the ellipse is not rotated with $\hat{e}_\theta$ and $\hat{e}_\varphi$. **b)** The ellipse was tilted in the tilt plane (perpendicular to the screen defined by $\hat{e}_r$ and $\hat{e}_\theta$) therefore is not in the *xy* plane anymore. However $\hat{e}_\theta$ and $\hat{e}_\varphi$ are still separated by angle φ from the ellipse principal axis. c) The final system is represented for which the unit vectors coincide with the ellipse principal axis. The unit vector $\hat{e}_\theta$ is just represented to show the intersection with the tilt plane.

Figure 3.10 - Example of a case in which a tilted reflecting surface doesn't touch the faceplate but the circle described by the surface limits around the vertex does. The program will only allow the flat target to be placed outside the circle limits.

Figure 3.11 - Possibility for a tilted and decentred surface to intersect a flat faceplate. The images represent the circle centred at the vertex passing through the surface limits just touching (**a**), intersecting (**b**) and failing to intersect (**c**) the faceplate (thick line) respectively. Only the top half of the faceplate section is represented and the decentration, bigger than R_{CD}, was enough to take the circle above the *z*-axis.

Figure 3.12 - Possibility for a tilted and decentred surface to intersect a cylindrical faceplate. Only the top part of the cylinder was considered.

Figure 3.13 - Possibility for a tilted and decentred surface to intersect a cone shaped faceplate with *PD* diameter pupil located at a z_{PD} distance from the origin. Only the top part of the cone section was considered (thick line) for each situation. It can be seen that there is no intersection if the circle centred at the vertex passing through the surface limits is bellow (**a**) or above (**c**) the faceplate. This last case was obviously disregarded since the surface cannot be outside the faceplate limits.

Figure 3.14 - Intersection between a circle and an ellipse (**a**), a maximum of four points can be found. Intersection between two circles (**b**) a maximum of two points can be found. The only exception is if the circles have the same radius and overlap.

Figure 3.15 - Possibility for a tilted and decentred surface to intersect a conoid shaped faceplate. Only the top half of the faceplate section was represented (thick line). If there is an intersection for a given value of z (z_{TEST}) the corresponding y value for the faceplate is smaller or equal to y on the circle centred at the vertex of the reflecting surface.

Figure 3.16 - Intersections of parallel light rays with a sphere in the *yz* plane. The dashed part of the circle is not part of the reflecting surface. **a)** Light rays travel from left to right, the object point is to the left of the surface. **b)** The opposite situation is pictured, the object is to the right of the surface vertex. This is possible when the surface is tilted (see text). In this case only rays that intersect the circle in two points on the useful part of the surface (ray 4) will be considered. In this context ray 3 is invalid since the only intersection on the useful part of the surface is on the back.

Figure 3.17 - Special ray tracing case with incident ray perpendicular to the surface *z* axis (N=0). **a)** Ray intersection failures due to ray direction in *xy* plane (P_1) and displacement along the *z* axis (P_2 and P_3). The values in parenthesis are the object point coordinates and the line matrices are ray directions. **b)** Section of the ellipse in the *xy* plane with an object point sending light rays in several directions. The scalar product of the direction of a particular ray with the vector $[x_V-x_T, y_V-y_T]$ is an indicator of the possibility of intersection with the surface in the incident ray direction.

Figure 3.18 - When the reflecting surface is tilted (**a**) it's possible for some rays to strike it from right to left or perpendicular to the surface *z* axis. The procedure adopted for ray tracing with a tilted surface is such that the surface will be straight and the faceplate tilted (**b**). In this case the ray tracing equations will be the same when transferring to the surface.

Figure 3.19 - Situations for which a light ray coming from an object point on the 90° semi-meridian directed to the upper reflecting surface edge on the meridional plane, after reflection strikes the pupil plane below (**a**), in (**b**) and above the pupil (**c**). The light ray directed to the surface vertex is always reflected below the pupil except if the object point is at the pupil edge (c).

Figure 3.20 - The ray directed to the reflecting surface edge fails to intersect the pupil plane after reflection. This case has to be analysed separately or the transmitted ray searching procedure will fail.

Figure 3.21 – a) Direction of the incident rays coming from an object point striking the pupil edges in the meridional plane after reflection. **b)** An imaginary object point located on axis on the faceplate vertex. It doesn't belong to the faceplate since the faceplate is limited by the pupil plane. In this case M_{ut} and M_{lt} are symmetrical.

Figure 3.22 - Axis systems used to define the direction of a ray inside a pencil of rays. **a)** The unit vector $\hat{e}_2$ is the direction of the central ray in the pencil, the axis system *xyz* is not the global system but a local system with the same directions but with origin at an object point. **b)** This system is to be placed at the end of $\hat{e}_2$ on a), it represents the position of a point *P* belonging to a ray in the pencil of rays. The unit vectors presented are just to define the directions. **c)** Representation of figures a) and b) together.

Figure 3.23 - Generation of an equal ray intersection density circular pattern in a plane. The ray intersections are disposed in circles around a central ray. Each intersection is located in the centre of an area equal to the area of the circle around the central ray (radius R_o). For the case displayed each area (k) external limiting circle has radius $R_k=(2k+1)R_o$. The numbers displayed are labelling the areas between two consecutive circles and do not relate to a particular sector.

Figure 3.24 - **a)** Equal density pattern positioned perpendicular to the *z* axis (central ray for the imaginary object point) and limited by the upper tangential ray. R_{0i} depends on the number of divisions to M_{uti}. **b)** Angle γ_{R0i} is used to calculate R_0, for any object point, determining the ray density.

Figure 3.25 - The full lines and dark dots correspond to the pattern presented in the previous figure for areas 0, 1 and 2. The dashed lines and light dots

correspond to a pattern where the central radius is halved from the previous value. The new odd numbered area centres will coincide with the inner borders of the old areas. The new even area centres will coincide with the old area centres needing twice as much rays therefore the old ones can be reused.

Figure 3.26 - Representation of the position of a ray in a pencil of rays with a central ray in the *y* direction (**a**) and -*y* direction (**b**).

Figure 3.27 - Direction cosines representing the upper rim ray $[0,M_{ut},N_{ut}]$, lower rim ray $[0,M_{lt},N_{lt}]$ and central ray $[0,M_c,N_c]$, from an object point, for a centred reflecting surface. The central ray was considered to be the one bisecting the two rim rays.

Figure 3.28 - Section of a pencil of rays coming from the imaginary object point on axis. The circle represents the front view of the reflecting surface area that transmits rays, after reflection, from the on-axis point. **a)** The central ray of the pencil is on-axis hence bisecting the upper and lower rim rays. **b)** The central ray is still in the meridional plane but is not bisecting, as a result more rays have to be traced to get the same effect.

Figure 3.29 - Decentred image of the first and second ring mire images, the videokeratoscope axis is not located at the centre of the first ring. If the *IMG* system of axis used for the ring height is kept at the videokeratoscope axis than a ring may have two heights ρ_1 and ρ_2 in one semi-meridian σ (**a**). If the *IMG* system is placed at the inner ring mire image centre the problem will be solved (**b**).

Figure 3.30 – a) Axial ray coming from the centre of the fixation light and striking a decentred reflecting surface. The image on the image plane won't coincide with the videokeratoscope axis. **b)** Same ray striking a centred reflecting surface, the image of the fixation light will coincide with the videokeratoscope axis therefore the alignment process was concluded.

Figure 3.31 - Tilted and decentred surface in order for an axial ray from the fixation light (direction $[0,0,1]_{GLB}$) to strike a surface point with normal parallel to the incident ray. In this case the incident ray is reflected in the opposite direction $[0,0,-1]_{GLB}$. The normal to the tilted surface in the point where the ray strikes is also $[0,0,1]_{GLB}$. In these conditions the image (black dot) of the centre of the fixation light will be in the centre of the image plane. The videokeratoscope will assume that the surface is centred due to the correct alignment in the videokeratoscope axis (*z* axis).

Figure 3.32 – a) A reflecting surface with rotational symmetry is tilted by an angle θ in the 90° semi-meridian. In this case an axial ray is reflected downwards. **b)** The system of axis is changed to *VTXTLT* and therefore the surface is straightened as explained in section 3.3. It is always possible to find a point on the surface (black dot) for which the normal has the same direction as the incident ray along the videokeratoscope axis.

Figure 3.33 - The reflecting surface is decentred along the line defined by the intersection of the tilt plane (paper plane for this case) and the *xy* plane of the global system (left figure). The decentration is applied in order to match the incident ray from the centre of the fixation light with the point with a normal matching that direction.

Figure 3.34 - Parameters defining the position of the image plane (*DF*) for a centred (**a**) and tilted or decentred reflecting surface (**b**). For a centred surface *DF* was measured from the paraxial plane while for a decentred or tilted surface it was measured from the vertex *z* coordinate in the global system.

Figure 3.35 - Spot diagrams for a spherical faceplate with a 250mm apical radius limited by a maximum diameter of 300mm and a 9mm pupil. Reflecting surface *p*=0.82 apical radius of 7.75 mm limited by a 9mm diameter and wd=80mm. The object point has 15° eccentricity in the 90° semi-meridian and the images have a

720X enlargement with a ray density of 20 rays. Defocus in mm from the paraxial plane from top left to centre bottom is 0 (**a**), 0.03 (**b**), 0.041 (**c**), 0.05 (**d**) and 0.08 (**e**). The best tangential focus is image c). Labels *u*, *l* and c refer to the intersection of the image plane with the reflected upper rim ray, lower rim ray and central ray respectively.

Figure 3.36 - Tangential focus for a centred surface corresponds to the intersection of the upper and lower reflected rim rays.

Figure 3.37 - a) The image of a single object point reflected in a tilted and decentred surface is represented (black dots) with low ray density. There is a lack of symmetry and the points closer and further away from o_l are not in the image semi-meridian σ (point *c* corresponds to the central ray). **b)** The effect of the images from adjacent object points is to place the maximum and minimum distance points aligned with semi-meridian σ. It is obvious that the images are grossly exaggerated in order to provide an explanation.

Figure 3.38 - Two successive iterations of the focus procedure. **a)** The image plane is moved in steps of *k*. The radial blur at each image plane position starts decreasing and then a point is reached in which the blur increases. This means that the best focus has been passed and the present image plane position will be the maximum limit for the next iteration. It can be seen in the figure that the minimum limit should be DF_n-2*k* rather than DF_n-*k* that way the best focus will be between the new limits. **b)** The next iteration for which the image plane will be moved between the two specified limits in steps of *k*/2.

Figure 3.39 - Image of an object point using a ray density of 5 **(a)**, 20 **(b)** and 200 rays **(c)**.

Figure 3.40 - Relationship between the *xy* direction of the several system of axis used. They are all presented from the examiner's point of view.

Figure 3.41 - Procedure to decrease the magnification to fit the image on screen and still leave around 10 pixels tolerance from the left screen limit. Note that the screen point corresponding to the central ray remains unchanged, it is the screen point corresponding to the global system origin o_{px} that changes to make that possible. The coordinate x_{Fmax} is the maximum positive value of the x coordinate, for that particular image, measured in the global system.

Figure 3.42 - Screen area used to represent the image of an object point reflected in a non-centred reflecting surface. It is a square area centred at pixel (350,195) extending 195 pixels for each side. The useful area will extend 185 pixels for each side allowing a 10 pixel tolerance on each side as well. Labels adjacent to points in the figure are x or y screen coordinates (pixels) while labels in the middle of line segments represent their length in pixels.

Figure 3.43 - Image fitted to the useful screen area with x pixels ranging from 165 to 535 and y pixels from 10 to 380. The limiting x and y coordinates of the image in the global system are also presented. The magnification parameter *MMPX* must be limited in order for all the limiting x and y image coordinates in the global system to fall inside the useful screen area.

Figure 3.44 - The videokeratoscope axis is perpendicular to the paper plane, intersecting it at the white dot. The other white dot is o_l the centre of the fixation light image or the centre of the ring mire image. The small dark dots represent the image of the object point presented (large dark dot) with a low ray density formed by a non-centred reflecting surface. In this case it is possible that no point in the image falls in the object semi-meridian σ_o. This can happen whether the image points meridians are measured in relation to the videokeratoscope axis (**a**) or in relation to o_l (**b**).

Figure 3.45 - Image dimensions along the direction marker. This marker is the line passing through o_I and the central ray position on the image plane (x_{Fc},y_{Fc}). The total image dimension along the direction marker b_{DMTot} is not of any interest. The dimension desired is the line segment that intersects the image b_{DM}.

Figure 3.46 - The image is a set of points disposed in a particular arrangement. If the ray density is not very high there will only be a point in the image that will coincide with the direction marker. That is the point corresponding to the central ray, which was used to calculate the marker.

Figure 3.47 - The vector from the image origin o_I to an image point Q can be decomposed in one component perpendicular to the direction marker ($d_{DM\perp}$) and another component parallel to it ($d_{DM||}$). The perpendicular component represents the distance from the image point to the direction marker.

Figure 3.48 - First step of the Iterative procedure to bracket R_0 between a value that provides a negative minimum B and another that results in a positive minimum B. The present example is for an array with 4 elements where the bracketing has been achieved in the 5th iteration. The initial ray density was too low and had to be increased by decreasing R_0.

Figure 3.49 - First step of the Iterative procedure to bracket R_0 between a value that provides a negative minimum B and another that results in a positive minimum B. The present example is for an array with 4 elements where the bracketing has been achieved in the 5th iteration. The initial ray density was too high and had to be decreased by increasing R_0.

Figure 3.50 - Second stage of the iterative procedure to find a value of R_0 for which $Bmin$=0. Iteration 5 refers to the last first stage iteration. The values in grey background are the ones that were not changed in a particular iteration.

Figure 3.51 – a) Irradiance of the vertical radial section of an object ring. **b)** An example of the image irradiance of the radial section sampled by the CCD detector. However only the images of the edges of the object ring were considered. An example of the irradiance of these points is represented in **c)**. The image ring edge detection uses an irradiance value of $0.5I_{max}$ as a reference. If an inner ring edge of an image ring is being detected the smallest y for which $I \geq 0.5I_{max}$ is considered to be the edge. If an outer edge is being detected the larger y for which $I \geq 0.5I_{max}$ is considered to be the edge. The y values represented are in the global system.

Figure 3.52 - Simulation of the summing effect of images of adjacent points on a ring edge. The image of a single object point on a ring edge (grey tilted ellipse) is rotated on both directions around o_I in order to completely cover the angular sector defined by the image limits at o_I (**a**). The resultant sector is represented in **b)**. The irradiance of this sector at a distance d_{oI} from o_I was considered to be constant and equal to the maximum irradiance displayed by the image points at the same distance on the original image. The image size is grossly exaggerated to illustrate the point.

Figure 3.53 - Modified geometry for van Saarloos algorithm. A ray with origin at a general object point is reflected in the corneal surface and enters the faceplate pupil.

Figure 3.54 - Doss geometry for determining the next corneal point. It considers two adjacent points joined by arcs.

Figure 3.55 - Videokeratoscope selection of the object point corresponding to a given image point. If the image point describes an angle φ with the horizontal the instrument will assume the object point describes the same angle. It considers that the image rings are centred in the instrument axis.

Figure 4.1 - Sections of cylindrical and cone shaped faceplates. **a)** The angle ϕ from the cylinder base to the opposite corner can be used to control the diameter *b* and the length *WD*. **b)** Cones with semi-aperture angles θ_1 and θ_2. Both cones start at a 9mm pupil aperture.

Figure 4.2 - Hyperboles with the same apical radius of curvature and asymptotic lines at 30 and 45 degrees inclination. The curves are similar to a cone in the periphery, but different at the centre.

Figure 4.3 - In a cone shaped faceplate it is always possible to define the five points (see text) as long as the cone has sufficient length to either side. The same applies to cylindrical, hyperbolic and parabolic faceplates. In spherical and ellipsoidal faceplates the surface can only increase in diameter until a certain point, after which it starts to close. In these cases it is not always possible to find the five points. The figure represents a case where it is only possible to define two of the five points.

Figure 5.1 - Differences (*SRE*) between accurate axial radii of curvature and axial radii of curvature calculated by the van Saarloos algorithm for surfaces 1 to 5. Faceplate pupil with 9 mm diameter and image plane at best focus.

Figure 5.2 - Differences (*TRE*) between accurate instantaneous radii of curvature and instantaneous radii of curvature calculated by the van Saarloos algorithm for surfaces 1 to 5. Faceplate pupil with 9 mm diameter and image plane at best focus.

Figure 5.3 - Differences (*SRE*) between accurate axial radii of curvature and axial radii of curvature calculated by the van Saarloos algorithm for surfaces 1 to 5. Faceplate pupil with 9 mm diameter and image plane at first ring mire image focus.

Figure 5.4 - Differences (*TRE*) between accurate instantaneous radii of curvature and instantaneous radii of curvature calculated by the van Saarloos algorithm for

surfaces 1 to 5. Faceplate pupil with 9 mm diameter and image plane at first ring mire image focus.

Figure 5.5 - Differences (*SRE*) between accurate axial radii of curvature and axial radii of curvature calculated by the van Saarloos algorithm for surfaces 1 to 5. Faceplate pupil with 4 mm diameter and image plane at best focus.

Figure 5.6 - Differences (*TRE*) between accurate instantaneous radii of curvature and instantaneous radii of curvature calculated by the van Saarloos algorithm for surfaces 1 to 5. Faceplate pupil with 4 mm diameter and image plane at best focus.

Figure 5.7 – Sagittal radius error for the decentred surface measured along the 0° semi-meridian (*SREDEC*) and sagittal radius error for a centred surface (*SRECTR*) in the same points.

Figure 5.8 – Sagittal radius error for the decentred surface measured along the 45° semi-meridian (*SREDEC*) and sagittal radius error for a centred surface (*SRECTR*) in the same points.

Figure 5.9 – Sagittal radius error for the decentred surface measured along the 90° semi-meridian (*SREDEC*) and sagittal radius error for a centred surface (*SRECTR*).

Figure 5.10 – Sagittal radius error for the decentred surface measured along the 135° semi-meridian (*SREDEC*) and sagittal radius error for a centred surface (*SRECTR*) in the same points.

Figure 5.11 – Sagittal radius error for the decentred surface measured along the 180° semi-meridian (*SREDEC*) and sagittal radius error for a centred surface (*SRECTR*) in the same points.

Figure 5.12 – Sagittal radius error for the tilted surface measured along the 0° semi-meridian (*SRETLT*) and sagittal radius error for a centred surface (*SRECTR*) in the same points.

Figure 5.13 – Sagittal radius error for the tilted surface measured along the 45° semi-meridian (*SRETLT*) and sagittal radius error for a centred surface (*SRECTR*) in the same points.

Figure 5.14 – Sagittal radius error for the tilted surface measured along the 90° semi-meridian (*SRETLT*) and sagittal radius error for a centred surface (*SRECTR*) in the same points.

Figure 5.15 – Sagittal radius error for the tilted surface measured along the 135° semi-meridian (*SRETLT*) and sagittal radius error for a centred surface (*SRECTR*) in the same points.

Figure 5.16 – Sagittal radius error for the tilted surface measured along the 180° semi-meridian (*SRETLT*) and sagittal radius error for a centred surface (*SRECTR*) in the same points.

Figure 6.1 - Best focus position from the paraxial plane (0 mm) for 15 image ring edges for the best cylinder.

Acknowledgements

I gratefully acknowledge the contribution of the following people and organisations to my Ph.D. education:

My supervisor Cristopher C. Hull, Ph.D, for his academic expertise, patience and always being there when I needed.

I am thankful to my friend and colleague Paulo Torrão Fiadeiro, Ph.D. and to my friend Professor Robert Fletcher for pushing me into doing a Ph.D.

I thank Beira Interior University (Portugal) for allowing me to take a leave in order to follow a Ph.D program at City University.

Thanks to Calouste Gulbenkian Foundation for financial support.

Finally I am deeply thankful to my parents and to my wife, Isabel, for their continuous support throughout my long Ph.D.

I grant powers of discretion to the University Librarian to allow this thesis to be copied in whole or in part without further reference to me. This permission covers only single copies made for study purposes, subject to normal conditions of acknowledgement.

ABSTRACT:

A computer model using finite ray tracing methods was developed to simulate a videokeratoscope analysing an average cornea. Different faceplate designs were tested using five points in the faceplate subtending angles between 15° and 75° in 15° intervals at the corneal vertex. Image quality was assessed by adding the geometrical blurs of the 5 image points; the best focal plane was considered the one that gave the smallest sum of the blurs. Surfaces were divided into five categories according to their blur sums and a representative of each group selected. Differences (error) between accurate sagittal radius of curvature and radius of curvature calculated by the van Saarloos algorithm were calculated for the selected surfaces at the same corneal points. The calculations were repeated for the tangential radius of curvature. Differences equal or bigger than 0.02 mm were regarded as clinically significant. The surface that provided the sharpest image for an average cornea was a cylinder with the base 120 mm away from the corneal vertex and a diameter of 26 mm. Changing the faceplate design results in clinically significant differences for an average cornea. Focusing errors have more influence than aberrations (controlled by instrument pupil aperture).

Glossary

CCD	Charged Coupled Device
CD	Diameter of the reflecting surface
CMS	Corneal Modelling System
DF	Distance from the paraxial plane to the image plane for a centred reflecting surface or distance from the surface apex to the image plane measured along the instrument axis for a tilted reflecting surface.
e	Eccentricity
GLB	Global Cartesian axis system
GLBTLT	Axis system resultant from the global system tilt
IMG	Bidimensional axis system (xy) with x in the opposite direction of the global system
MAXD	Maximum diameter of the instrument faceplate
MMPX	Parameter that controls the image magnification on screen
o_I	Origin of the IMG system of axis
p	Parameter that controls the rate of peripheral flattening of a conic or a conoid
PD	Pupil diameter of the instrument faceplate
PMMA	Polymethylmethacrylate
PUP	Axis system with origin at the faceplate pupil
R_{CD}	Radius of the circle described by the edges of the reflecting surface when the surface is rotated around its apex
R_0	Parameter that controls the ray density in a bundle of rays
S_{PARAX}	Position of the paraxial plane from the reflecting surface apex
TMS	Topographic Modelling System
VTX	Axis system with origin at the reflecting surface apex
VTXTLT	Tilted global system of axis with origin at the reflecting surface apex
wd	Distance from the instrument pupil to the reflecting surface apex
z_{CD}	z coordinate of the end of the reflecting surface measured from the surface apex
z_{MAXD}	z Coordinate of the faceplate end
z_{PD}	z Coordinate of the faceplate pupil
ϕ_{MAXD}	Angle subtended by the faceplate end and instrument axis at the reflecting surface apex
ϕ_{PD}	Angle subtended by the instrument pupil and instrument axis at the reflecting surface apex

1 Introduction

The analysis of the anterior surface of the cornea is of major importance. Over the last centuries several methods have been developed to do so. Mejia-Barbosa and Malacara-Hernandez (2001) have presented a good review on the modern methods which include specular reflection techniques, diffuse reflection techniques and techniques using scattered light. Specular reflection methods include Placido disk systems, interferometric methods and Moiré deflectometry. The diffuse reflection group includes Moiré fringes, rasterstereography and Fourier transform profilometry. The last group, scattered light techniques, includes the slit-based system. Less common methods were reviewed by Clark (1973), which included many of the ones described by Mejia-Barbosa and Malacara-Hernandez. It also included direct photography of the corneal profile or projecting its shadow on a screen, casts, studying the fluorescein pattern beneath a scleral contact lens and pressing rods against the cornea. From all these methods the most widely used have been Placido disk systems which have been incorporated in videokeratoscopes. These instruments allow for planning and monitoring the results of refractive surgery, which were reviewed by Rabinowitz (1995). Videokeratoscopes generally include contact lens fitting software allowing, according to Szczotka (1997), for a 77% successful first fit in patients with normal corneas. It also reduces "chair time" by approximately 50% when compared to traditional methods of fitting. Rabinowitz et al. (1991) state that videokeratoscopes can be of great value in contact lens fitting in keratoconus since keratometry measures just four points. These are just a few of the possible applications of these instruments.

However, videokeratoscopes are affected by focusing, tilt and decentration of the analysed corneas, decreasing the measurement accuracy. The wide acceptance and importance of these instruments has led to the selection of this research topic, since they will still be present for many years to come in clinical practice. The development of a versatile videokeratoscope computer model capable of handling

reflecting surface decentration and tilt is fundamental for the research on these errors. This is mainly due to three factors: simulation of different instruments, accurate reflecting surface modelling and positioning. Videokeratoscopes are expensive instruments therefore investigators can only have one or two systems in their research centres. The developed simulation program allows for a change on the videokeratoscope parameters, mimicking several instruments. At present, test surfaces are verified by interferometry or profilometry, methods with very good but limited accuracy. These methods are sometimes not available in the investigator's own research centre and surface calibration and manufacturing has to be requested from an external source. The computer model of a surface has no errors, therefore saving money and time. The positioning of the reflecting surface in relation to the instrument poses another problem. Decentrations can be executed with an acceptable accuracy but tilt is difficult to control. Although a goniometer allows for an accurate tilt from an initial surface position, this position is the problem. It is almost impossible to attach a surface to a goniometer without introducing surface tilt. The simulation program allows for an exact tilt angle solving the previous experimental problem.

1.1 Synopsis

In the first chapter, Introduction, several methods for corneal topography analysis are briefly described. The importance of this analysis is presented and the reasons for undertaking this research project, explained.

The second chapter, Literature review, is divided into five sections covering keratoscopy, faceplate design, reconstruction algorithms, alignment and errors due to tilt, centration and focus. Each section is a comprehensive summary of the research work of several investigators on that particular field. It also includes comments where appropriate. The section on keratoscopy is an historical review of this method from the first analysis of a reflected corneal image to the development of the modern videokeratoscope. The section on faceplate design first describes several patterns up to the development of the concentric ring pattern on a flat

target. From then the evolution of faceplate shapes using that pattern is considered. The section on reconstruction algorithms describes their evolution from the simpler methods to complex iterative methods. Each algorithm is thoroughly analysed and its advantages and disadvantages presented. The section on keratoscope alignment describes the method used by videokeratoscopes to centre the reflecting surface on the instrument axis. Ending this chapter there is a comprehensive review of the research on tilt, centration and focusing errors. It includes qualitative methods, based on simple observations, and quantitative methods.

The third chapter, Computer modelling of a videokeratoscope system, is the main part of this research project – the development of the research tool. It is composed of 16 sections that describe the theory necessary to understand each part of the model. The first section, Faceplate model, describes the mathematical equations for the faceplate shapes used and their properties. It also describes how the rings on the faceplates are defined, since the rings are the object points. The second section, Reflecting surface, investigates conoidal surfaces as those chosen to represent a model of the cornea. It also presents the parameters for an average normal human cornea based on the research of other investigators. The third section, Axis systems, is a complex section that presents all the systems used. These systems include, observer view, patient view, and the tilted system to apply for a tilted surface. It also includes the mathematical relations between all systems. The fourth section, Decentring the reflecting surface, presents the mathematical limits of the decentration applied to the reflecting surface. This is important to prevent the surface touching or passing the limits of the defined faceplate. The fifth section, Tilt limits, is the same investigation of limits applied to the tilted reflecting surface. Its mathematicel treatment is however more complicated than for decentration. The sixth section, Ray tracing equations for reflection, is a comprehensive analysis of the usual ray tracing equations for reflection, detecting all possible errors. This section also describes a simple method developed to handle tilted surfaces. The seventh section, Finding a transmitted ray through the

faceplate pupil, describes a very powerful procedure for a centred surface. It is necessary to find the central ray before defining a pencil of rays. No separate procedure is applied for a non-centred surface, in this case a bundle of rays is sent to cover the entire surface and any transmitted ray is detected. The eighth section, Pupil exploration in the tangential plane, is aimed to determine the direction of the incident rays, coming from an object point, for which the reflected rays strike the pupil limits in the meridional plane. It is only applied for a centred reflecting surface. These directions are then used to determine the best focus position for each object point. The ninth section, Pencil of rays from an object point, ray density, describes how the ray density on each pencil of rays is defined in order to send a uniform bundle of rays from each object point. The tenth section, Central reference point of the ring images, describes the definition of this point used as an origin for the measurement of image ring edges heights. The eleventh section, Videokeratoscope alignment simulation, describes the mathematical operations needed for this procedure. The twelfth section, Focus, describes how the best focus for single object and multiple object points, on centred and non-centred reflecting surfaces was determined. The thirteenth section, Image relative irradiance, describes the method used to determine the irradiance distribution on an image from an object point which is related to the way images are presented on the computer screen. The fourteenth section, Ring edge detection, describes the method developed to transform the image of a single object point in a ring edge and the simulation of an edge detection algorithm. The fifteenth section, Reconstruction algorithms adaptation, describes the modifications of the two selected algorithms (described in section 3 of chapter 2) to fit the parameters defined for the developed videokeratoscope model. Other modifications were also applied in order to increase accuracy. The sixteenth section, Difference maps, describes how these maps were defined in order to present the differences from two reconstruction maps for the same reflecting surface obtained by different conditions. This procedure allows studying the effect of each parameter on the reflecting surface reconstruction.

Chapters 4, 5 and 6 are respectively the methods, results and discussion for 4 research projects using the developed computer model. Each chapter is divided into the same sections, each a research project (the third and fourth projects are not complete since more data would be needed to validate the findings). The first section, Determination of best faceplate design, is aimed at finding the faceplate design that results in the sharpest image of the object rings. The second section, Influence of faceplate design on radius of curvature maps, is aimed at proving that different designs (classified by the image blur produced) will produce different results with clinically significant differences. The third and fourth sections are aimed at determining the effects of reflecting surface decentration and tilt on the reconstructed surface.

Chapter 7 presents the main findings of the four research projects and indicates the novel aspects of the computer model. It also suggests new research based on the application of the developed computer model.

2 Literature review

2.1 *Keratoscopy*

Levene (1965) has compiled an historical review of keratoscopes. According to this author, Father Cristopher Scheiner in 1619 was the first known investigator to analyse the reflected image in the cornea. He compared the size of the corneal image to the size of the reflected image in a set of marbles with known radius of curvature. This permitted an estimation of the corneal curvature. Later in 1808 Sir David Brewster observed the changes in size and shape of a candle reflex in a conic cornea. These experiments were the precursors of the keratoscope. The first keratoscope was a simple instrument conceived by Henry Goode in 1847. It was just a small luminous square held a few inches from the eye.

Plácido (1880a) designed a device to analyse corneal surface irregularities. It consisted of a rectangular plate of unpolished glass with two black lines made of paper, glued to its surface. He called this simple instrument an "external keratoscope". The patient was placed near a window and the plate acted as a diffuser for the day light. Irregularities of the lines reflected in the corneal surface would indicate corneal irregularities. In the same year Plácido (1880 b) wanted to extend his original idea to allow an astigmatic analysis of the cornea. He designed two new devices made of white cardboard with a central opening. The first was a black square grid drawn on the white cardboard. He abandoned this idea since he could only analyse two perpendicular meridians at a time. He then decided to use a set of concentric rings which allowed a simultaneous analysis of all corneal meridians. In his paper he refers to this instrument by three names, "exploring astigmatoscope", "kerato-astigmatoscope" and "astigmatoscopic disk". Today the concentric rings design is named Plácido disk and is still used in all reflection based videokeratoscopes.

Levene (1965) refers to the controversy around the invention of the concentric ring keratoscope. Emile Javal claimed that he was the instrument inventor in 1881 and not Plácido. This probably occurred because Plácido's scientific papers on the

concentric ring keratoscope were published in Portuguese. Javal was however the first to use a magnifying lens in the instrument.

Plácido (1881) initially recorded his observations by drawings, however this was a very cumbersome process. He then had the idea of photographing the reflected images which was much faster and accurate and photokeratoscopy was born. It should be noted that Alvar Gullstrand is often erroneously credited with the application of photography to keratoscopy in 1896 (Gullstrand 1966). Since Plácido's invention many other photokeratoscopes have been developed by different investigators.

Gormley et al. (1988) developed a keratoscopy instrument that captured the ring mire image reflected in the cornea via a CCD camera. This device was named Corneal Modeling System (CMS) and was the first videokeratoscope. The digital record allowed for an immediate analysis of the image in a computer. Since then many other videokeratoscopes have been developed. Computerised analysis of photokeratoscope photographs has also been done in the past. This was however much slower than a videokeratoscope since the photograph had to be digitised. The digitisation process used by Klyce et al. (1984) consisted of a graphics digitising tablet and Busin et al. (1989) used a CCD camera.

The hand keratoscope with a self luminous Placido disk invented by Klein (1958) is worth mentioning since it is still used today. It is a very simple and inexpensive hand held instrument that allows a qualitative analysis of the corneal surface. It is ideal for clinical use.

2.2 *Faceplate design*

Ludlam and Wittenberg (1966a) and Mammone et al. (1990) presented a survey on faceplate designs. The first target design was flat, the Placido disk. To provide an adequate corneal area coverage a flat target has to be much larger than any concave target placed at the same distance. The graphic representation of this

problem can be found in the papers by Stone (1962) and Fowler and Dave (1994). Ludlam and Wittenberg last report a flat target back to Reynolds 1959, since then it seems that this design was discontinued for photo and videokeratoscopes. However the flat target has been applied to topographic keratometers after 1959, since this design simplifies calculations and these instruments are not meant to measure the peripheral cornea. One example is the photokeratometer designed by Fry (1975). Berg (1927) cited by Ludlam and Wittenberg appears to be the first investigator to use a non-flat target. He used two perpendicular arcs, increasing the corneal area covered.

Wittenberg and Ludlam (1970) presented results on optimum faceplate designs both for a spherical and elliptical reflecting surface (resembling the cornea). They concluded that an elliptical target was the best design but the theoretical calculations and the experimental work resulted in different ellipsoidal shapes. They used a small vertical line as an object. However such a line segment is imaged on the sagittal focal plane whereas their theoretical calculations applied a formula derived to calculate the tangential focus. This could explain the discrepancy in their results. In addition the formula for tangential reflection is derived only for a small area of the reflecting surface (Longhurst, 1973). This formula is

(2.1) $$\frac{1}{a}+\frac{1}{t}=\frac{2}{R\cos\beta}$$

where a is the distance from the object point to the reflection point measured along the principal ray, t is the distance from the reflection point to the tangential focus measured along the reflected ray, R is the spherical surface radius of curvature and β is the angle of incidence of the principal ray.

Wittenberg and Ludlam's camera had a large aperture, increasing the corneal area covered by a pencil of rays coming from a single object point. Using the tangential reflection formula (equation (2.1)) in such conditions may be a poor approximation.

Mandell and St. Helen (1971) determined experimentally the best target design for spherical and parabolic reflecting surfaces. They used a target with moving parts but didn't attempt to fit any particular surface to the final result.

Rowsey and Isaac (1983) and Binder (1995) claimed that a parabolic design would decrease optical aberrations, allowing for a flat image plane. Although it appears that no experimental work was done by them to support this claim, it may arise from the fact that the loci for sagittal and tangential focal surfaces for a plane object are parabolic in shape (Hecht, 1998). Reversing the path of the rays, a parabolic target would result in a flat image plane.

It is interesting to note that some investigators designed targets in order to produce an even spacing of the mire rings when reflected on a particular spherical surface. This was done originally by Gullstrand in 1896 (Gullstrand 1966) to simplify the calculations in his reconstruction algorithm. This process was repeated by Knoll (1961), Townsley and Ridge (1967), Rowsey et al. (1981) and Mammone et al. (1990).

2.3 *Reconstruction algorithms for Placido disk based systems*

2.3.1 *Telecentric videokeratoscope principle*

This is not a reconstruction algorithm but an approach adopted in several algorithms in order to simplify the calculations. In a telecentric videokeratoscope a stop is placed at the second principal focus of the objective lens (Rand et al. 1997). The aim of this setting is to stop all the rays non-parallel to the optical axis. In this case the height h of an object point's image (Figure 2.1) is equal to the height of the reflecting surface point from which the ray is reflected.

However the telecentric condition is only exactly met if the stop used is a pinhole. This is impractical in most systems since there will be insufficient light in the image. To overcome this problem there are two solutions. The first is to increase the object illumination and the second is to increase exposure time. However when working with a living subject both solutions are inadequate: A strong illumination will be very uncomfortable resulting in inadequate subject fixation. A longer exposure time will result in a blurred image due to subject motion. If a pinhole can't be used the algorithms using the telecentric approach will lose accuracy.

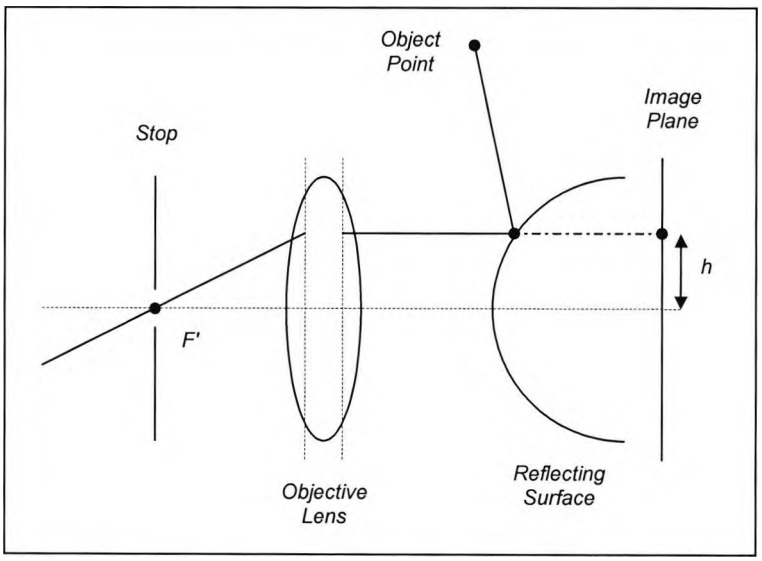

Figure 2.1 - Telecentric videokeratoscope principle. A stop is placed at the second principal focus of the objective lens to block all rays non-parallel to the optical axis. The height of the reflection point in analysis (*h*) will then be the same as the height of the image point in the image plane.

2.3.2 *Gullstrand's algorithm*

The first algorithm to analyse data from keratoscopes was developed by Gullstrand in 1896 (Gullstrand 1966). It had however serious inacuracies pointed out by Wittenberg in the appendix to Ludlam's translation of Gullstrand's work (Gullstrand 1966). For example he considered the gradient of the normal at a reflection point to be independent from the point position and surface curvature. A further error was introduced by considering the reflection point abscissa equal to the working

distance of the camera. These problems make Gullstrand's algorithm unsuitable for use. There is however a part of his algorithm that has been used by many investigators after him. He considered the reconstructed reflecting surface to be made of circular arcs joining each pair of calculated adjacent points. Each arc was centred on the intersection of the normals to the surface at each pair of points. This ensures that when two arcs join they share the same tangent resulting in a smooth surface. He also acknowledged that the centre of each arc could be located outside the instrument axis. Although he seems to be the first to introduce this approach in the analysis of corneal shape this property probably was known by mathematicians long before Gullstrand. The algorithm and the instrument developed by Gullstrand were tested with a spherical ocular lens (Seyberts Ocular IV). The lens radius of curvature was not given by the author. In the appendix to Ludlam's translation of Gullstrand's work, Wittenberg (Ludlam's coworker) found a difference of 0.05 mm between the lens calculated radius of curvature for the larger and smaller mires. Since there is no data for the lens radius of curvature the algorithm's accuracy cannot be assessed.

2.3.3 *Wittenberg and Ludlam algorithm*

Wittenberg and Ludlam (1966) considered that the height of the ring mire image in the image plane could be calculated using a single ray passing through the camera objective's first principal point. They based their analysis on an equation that gives the position of the tangential focus since the rings are imaged on the tangential plane. A differential equation was derived but a solution wasn't presented. Their conclusion was that any curve that represented the corneal surface had to satisfy that equation. Although they came short of achieving surface reconstruction, the differential equation can be solved using numerical methods. A problem would be the initial conditions necessary to solve the equation. Even if the equation is solved this method is not very accurate due to two factors: The first is that the ray passing through the principal point may not be the one corresponding to the ring edge. The second is that the equation they used to determine the position of the tangential focus is only valid for spherical surfaces. Although an aspherical surface can be

constructed with small arcs, their centres of curvatures will need to be off-axis. When deriving the equation for the tangential plane Longhurst (1973) considered that the centre of curvature must be on axis therefore it cannot be valid for an aspherical surface.

2.3.4 *Townsley and Ridge algorithm*

Townsley and Ridge (1967) used a pinhole camera approach for a non-telecentric keratoscope target. They reconstructed the reflecting surface using a different method from Gullstrand's but they used the circular arc approach to obtain a smooth surface. The problem with this algorithm is in the first step, the calculation of the slope of the ray coming from a target point and striking the reflecting surface (this will be the only ray transmitted to the instrument pupil for that target point in the pinhole camera approach). The authors state that the slope of this ray can be found solely from the target point location. This implies that the slope of this incident ray (transmitted through the instrument pupil after reflection) is independent of the reflecting surface which is not correct. The authors didn't mention testing with calibrated surfaces, only referring to measuring precision on image ring mire heights. In another paper, Townsley (1970) using the same photokeratoscope and algorithm states that photokeratoscope data can reconstruct the corneal profile to an accuracy of 9 μm or better. However it is not clear if he is referring to his system or how this value was determined.

2.3.5 *El Hage's algorithm*

El Hage (1971) presented a reconstruction algorithm similar to Wittenberg and Ludlam's. It was based on the same equation for determining the position of the tangential focal plane however El Hage used the telecentric approach. He derived a simpler differential equation and proposed a method to solve it. The initial conditions problem was solved by comparing the central reconstructed surface with a sphere. This approach was due to the fact that an aspherical surface can be considered a sphere at its central part. The radius of this sphere was obtained by keratometry on the analysed cornea. Even for a perfect telecentric

videokeratoscope this method will lose accuracy due to the fact that it is based on the equation for finding the tangential focal plane (see 2.3.3). The author does not mention testing on calibrated surfaces, presenting only a precision of 0.02 mm on the extreme periphery of the corneal profile. However El Hage (1989) applied his system to a telecentric videokeratoscope, the EH-270 claiming an accuracy of ±0.12 D. This value was calculated with the data from a single image ring mire on a 8.33 mm (40.50 D) sphere.

2.3.6 *Fry's algorithm*

Fry (1975) designed a telecentric photokeratoscope with a flat target. He recognised that the peripheral cornea would not be covered and decided to use the instrument as a photokeratometer. The flat target was used to simplify the calculations since one coordinate is constant. He started by deriving a differential equation by applying the same steps as El Hage (1971) arriving at exactly the same result (although El Hage is not acknowledged). To achieve the reconstruction Fry considers the differential equation a quotient of finite quantities Δy / Δx. Δy is obtained by measuring the height difference between two image rings in the keratograph and Δx is then calculated by the differential equation. This approach would only be accurate if the image rings were infinitely close, which is not the case, therefore it is an approximation. He fails to mention how the distance from the target to the corneal apex is obtained, although it is probably considered to be a constant value. Fry does not mention testing his algorithm on calibrated surfaces.

2.3.7 *Doss et al. algorithm*

Doss et al. (1981) developed the first iterative algorithm for surface reconstruction. They used a pinhole camera approach and considered that all reflecting surfaces would have an apical radius of 7.8 mm. This value was chosen since it resembles the average apical radius of the human cornea. All the calculations were based on a spherical faceplate. A linear magnification was considered, the ring height (x in their axes system) was calculated by dividing the ring height measured in a magnified keratograph by the magnification. The keratograph was taken by the

Corneascope, a photokeratoscope of the time. To obtain a reconstructed point (x_i,y_i) it was considered that an arc would join it to the previously determined point (x_{i-1},y_{i-1}). The mathematical formula used to achieve this relates the coordinates of the two points with the angle of the tangent to the surface at each point. For each new point one coordinate (x) was taken from the keratograph but the other coordinate (y) and the tangent angle are still variables. An initial value for the angle was considered to be half the angle from the object ring to the centre of curvature of the spherical faceplate. This angle was used in the formula to obtain an estimate of y for the unknown corneal point. This coordinate was then replaced in another formula that related the tangent angle with the incident ray on the corneal surface. After calculating the tangent angle with this new formula, this value would then be replaced in the initial formula to obtain a better estimate for y. The iterative process would continue until the difference of two y values calculated in successive iterations reached a predetermined value.

The authors state that in order to use this algorithm the reflection surface would have to be spherical with its centre of curvature coincident with the spherical faceplate centre of curvature. However after executing a careful analysis of the mathematics I concluded that it is valid if the curvature centres are not coincident and it also works for aspherical surfaces. The only advantage of a spherical reflecting surface with the centre of curvature coincident with the centre of a spherical faceplate is that the initial approximation of the tangent angle corresponds to the true value of the angle. In this case only one iteration would be needed.

The main problem with this algorithm is considering that all surfaces have the same apical radius. The authors tested the algorithm on a 9.52 mm radius sphere resulting in reconstructed surface with an average radius of 9.663 mm with a standard deviation of 0.2385 mm.

2.3.8 *Klyce's algorithm*

Klyce (1984) presented a refinement of Doss et al.'s algorithm. The main difference was the calculation of the central radius of curvature instead of the constant value used by Doss. This was achieved by considering the average image height for the central image ring (x_1 in his system of axis) and relating it with the object ring coordinates and working distance of the photokeratoscope (distance from the pupil plane to the image plane). This last parameter was used considering that the image plane would coincide with the surface reflecting point y_1 coordinate (in his system). This is never the case but is better than the Doss constant apical radius approach.

Klyce presented an interesting approach for determining the tangential radius of curvature (see section 3.1.1 for definition). It combined the coordinates of three adjacent surface points determined by the reconstruction algorithm to calculate the centre and radius of a circular arc passing through the points. The radius of the arc would be considered the tangential radius of curvature for the central point of the three considered. This method would then be applied to the next three points and the third point of the previous calculation would now become the middle point. This method fails in the point determined from the outer ring mire data since there is no next point. In this case it could be considered that the last point would have the same tangential radius of curvature as the previous point.

Based on the analysis of five spheres ranging from 6.9 to 8.4 mm radius of curvature, Klyce claims an accuracy of less than 0.1 mm on measuring radius of curvature. The calibration sphere's radiuses were measured with a convex radius gauge to within 0.05 mm.

2.3.9 *Spherical Biased*

This algorithm developed by Rowsey and Isaac (1983) is based on finding a sphere for each ring edge sector that produces a similar ring edge image to the

unknown reflecting surface in analysis. It uses the known property of spherical convex reflecting surfaces for which a larger radius of curvature results in a larger image. It was designed for a photokeratoscope available at the time, named the Corneascope. This device had 9 rings along a parabolic faceplate according to the authors. Six calibrating spheres were used with radius of curvature ranging from 5.5mm to 9.52mm. Each one of the spheres was used in the Corneascope, which photographed the image of the rings on the sphere surface. The distance from the centre of the inner ring to the inner ring edge of each image ring (hemi-chord length) was measured in the picture along eight semi-meridians. The average of the eight semi-meridians hemi-chords was placed as a point in a graph of hemi-chord length against radius of curvature. After the analysis of all ring edge images for all six spheres, a linear regression line was calculated for each of the 9 ring edges.

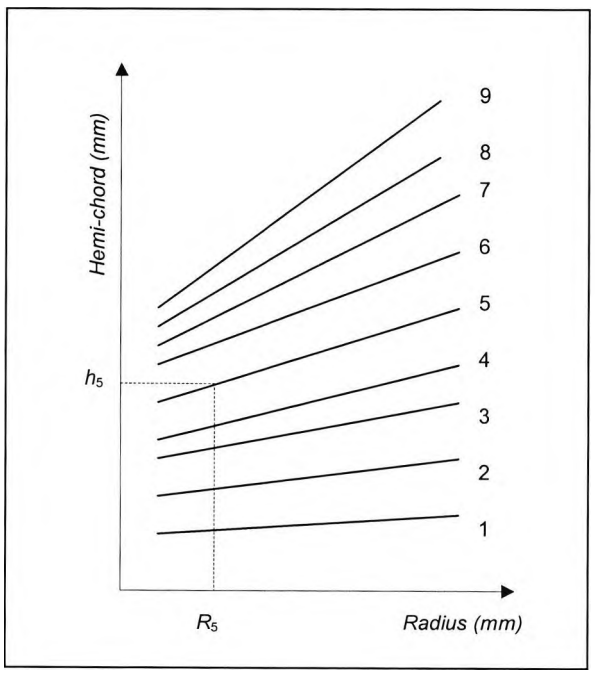

Figure 2.2 - Calibration graph for a 9 ring keratoscope for use with the spherical biased algorithm. If the inner edge of the 5th image ring is in analysis in a keratograph then the line corresponding to this edge is selected. Supposing that the ring mire image of this ring edge has an hemi-chord height of h_5 then the corresponding radius of curvature in the reflection area is R_5.

The final calibration graph is similar to the one presented in Figure 2.2. This figure represents an example of the use of the graph. If the inner ring edge of the 5th image ring is being analysed then the line for the 5th ring edge image is selected on the graph. Supposing that the ring mire image corresponding to this edge has an hemi-chord of height h_5 then, from this line, the radius of curvature is R_5.

The image ring height measured by Rowsey and Isaac was based on a photograph with 4.8X magnification in relation to the real size. They have assumed that the magnification was linear therefore if the hemi-chord is divided by 4.8 the original size of the hemi-chord was obtained.

It should be noted that they developed this simple method when analysing photokeratoscope photographs in an instrument called a comparator. According to Goss (1991) this device was used with the corneascope photographs, which were optically enlarged so that a particular ring image analysis would match a circular mark corresponding to the same ring. The magnification used for the ring was then converted to radius of curvature by an unknown algorithm. Probably this instrument already used a very similar algorithm to the one Rowsey and Isaac developed.

The idea for the spherical biased algorithm can be traced as far back as Fincham (1953). In his paper he states "A close approximation of the radius of curvature of the surface may be obtained by the direct comparison method of photographs of the images produced by a number of steel balls of known diameter, and the results plotted in a graph show the relation between radius of curvature and diameter and width of the rings. The record of the corneal image is then measured either on an enlarged print of known magnification or simply by projecting an image of the negative to a known size, and the values are read off on the graph."

Roberts (1994a) has shown that although this algorithm is adequate to analyse spherical surfaces it doesn't work well for aspherics. The error increases towards

the periphery of the surface. Rowsey and Isaac (1983) tested their algorithm on a 7.96 mm radius steel ball obtaining an average radius of 7.955 mm.

Since the algorithm is based on the size of the image produced by spheres the radius of curvature determined is the sagittal radius of curvature (see section 3.1.1). It would only be suitable for a telecentric keratoscope since each radius of curvature is attributed to a point on the surface with the same height as the ring mire image. However the coordinates of the surface reflection points along the videokeratoscope axis cannot be determined by this algorithm preventing the reconstruction of the original surface.

2.3.10 *Edmund and Sjontoft algorithm*

Edmund and Sjontoft (1985) developed a reconstruction algorithm based on the assumption that the cornea would be a conoid (however their calculations do not work for a parabola) and that the image plane would be located at a distance of half the apical radius from the corneal vertex. This is a paraxial approach for spherical mirrors when the object is at an infinite distance, and is therefore only approximate for the finite distance of the faceplate. They attributed values to the apical radius (*Ro*) and eccentricity (*e*) of the aspherical reflecting surface and compared the ring image height measured from the keratograph with the ring image height calculated by finite ray tracing. A linear magnification was considered in order to achieve this. For each keratoscope ring the difference from the calculated and measured image height was determined and squared. These squared differences were then added and the sum was the parameter used to evaluate the values of apical radius and eccentricity used. Then new values were attributed to *R* and *e* and the process repeated until a minimum sum was found. The authors do not mention testing the algorithm with calibrated surfaces.

2.3.11 *Wang et al. algorithm*

Wang et al. (1989) developed a two-step algorithm. The first step was applied to the central cornea using the tangential equation for reflection. The second step

was for peripheral points and considered that any two points could be joined by a segment of arc. It combines procedures used in previous algorithms. The use of the tangential reflection formula (equation (2.1) for the central cornea is adequate since this part can be considered spherical. Wang and coworkers realised that this equation is not suitable for peripheral points. They present their sets of equations in vectorial form and do not solve the vectors in their components. However if this development is done it can be seen that the distance from the instrument pupil to the corneal apex wasn't calculated. Therefore one equation is missing to allow for an accurate solution of their system of equations.

They tested the algorithm on a steel sphere of 8.33 mm radius of curvature and an axial symmetric ellipsoid with a 7.73 mm apical radius and eccentricity 0.5. The surface parameters were checked on a microscope with stage verniers. They found a maximum error of 0.8% (0.06 mm) for the spherical surface and 2% for the ellipsoid.

2.3.12 *Mammone et al. algorithm*

Mammone et al. (1990) presented the algorithm that was used for the first videokeratoscope, the CMS. The reconstruction was based on fitting a conoid to all points by an iterative least squares estimate. The iteration starts with a p value of 1 for the conoid, which corresponds to a sphere. The initial apical radius was determined based on an equation derived by considering that the image plane was positioned at the mirror focus. This assumption is an approximation, it would only be accurate if the object (faceplate) was at infinity. Furthermore they apply a relation between coordinates and radius of curvature of two circles which is only valid if the circles share a common centre of curvature. However in their system the two circles (reflecting surfaces) are located at a constant distance from the instrument pupil so they share a common vertex and therefore are not concentric. The values of p and apical radius were then applied in the iteration and new values of these parameters estimated. The iteration stopped when the difference between p values calculated in two successive iterations was below a certain value.

Hannush et al. (1989) tested the CMS on four calibrated steel balls (38.66, 42.52, 43 and 50.14 D) and presented an accuracy within ±0.25 D for the first three spheres and ±0.37 D for the steepest. The data corresponds to rings 2 to 26 (the instrument has 32 rings). Rings 27 to 32 were not processed by the instrument and the first ring data was not used due to extreme variability.

2.3.13 *Gersten et al. algorithm*

Gersten et al. (1989) presented a refinement of the Mammone et al. algorithm developed for the CMS videokeratoscope. It was then applied to the instrument that replaced the CMS, the TMS. The algorithm is very similar to the original except in the estimation of the initial apical radius. This estimation is based on an equation that is only valid for a telecentric videokeratoscope, which is not the case for the instrument they describe. This equation is then combined with a relation between the surface to analyse and a reference sphere that relates coordinates and radius of curvature of both spheres. This relation is the same described in section 2.3.12. However the authors acknowledge that the relation is not adequate if the spheres share a common vertex. Instead of trying a different approach they decided to multiply each value of the apical radius, determined by the equation for each data point, by a correction factor. This factor was determined by a least squares solution from analysis of several reference spheres with radius ranging from 6.75 to 8.8 mm.

Wilson et al. (1992) tested the TMS on three calibrated spheres previously verified with a radiuscope. At 1 mm from the sphere's apex the instrument presented a maximum error of 0.23 D and at 3 mm from the apex the error ranged from 0.18 to 0.69 D.

2.3.14 *van Saarloos and Constable algorithm*

van Saarloos and Constable (1992) presented a refinement of Klyce's algorithm (see 2.3.8), which in turn was a refinement of Doss et al.'s algorithm (see 2.3.7).

One of the most important modifications of the algorithm was to lose the telecentric approach employed by the previous authors. A second important modification was to turn the calculation of the apical radius of curvature into an iterative approach that worked much better than the methods of Doss and Klyce. van Saarloos included the paraxial equation for spherical mirrors in the calculation of the apical radius, which is adequate for the first keratoscope ring.

The authors tested the algorithm on a sphere (radius not specified) using finite ray tracing. The results are presented in graphical form and compared to Klyce's algorithm (2.3.8). A maximum error on the sag of the reconstructed surface of less than 4 μm is presented versus a maximum error of around 27 μm in Klyce's algorithm. For all points the error was always larger for Klyce's algorithm.

2.3.15 *Klein's algorithm*

Klein (1992) developed an iterative reconstruction algorithm based on a third degree polynomial. This function results from a Taylor series expansion up to the third order around a known surface point, the one determined for the previous ring (i-1). The first and second derivatives for ring (i-1) were obtained from differentiation of the Taylor expansion around ring i-2. The third derivative for ring (i-1) was obtained by several approximations. Based on this estimation of the reflection point the angle of incidence and reflection are calculated and compared. The reflection point position is then changed and a new iteration begins with the new value. The procedure ends when the difference between the incidence and reflection angle is less than a pre determined value. The Taylor expansion assures a continuous surface.

Klein tested the procedure by finite ray tracing with a 10 mm radius sphere concentric with a 10 cm radius spherical faceplate. The algorithm simulation with these parameters lead to a reconstruction accuracy (corneal point position) better than 1μm.

2.3.16 *Andersen et al. algorithm*

Andersen et al. (1993b) developed an iterative algorithm to analyse the data from their photokeratoscope, described by Anderson et al. (1993a). The algorithm was divided into three different parts. The first was called screenmapping and calculates the angles subtended between the instrument axis and the rays from each ring mire directed to the intersection of the image plane with the axis. The image plane position is fixed in relation to the camera. To achieve focus the instrument moves in relation to the reflecting surface, therefore the mentioned angles are constant for each mire and do not depend on the reflecting surface. A direct calculation of the angles from the ring mire positions and camera working distance is easily obtained. However they followed a very complicated path. Since the working distance is much larger than the radius of the measured surface they considered that the ring mires were at infinity and therefore the image plane was located at half the radius of curvature of the surface from the surface vertex. They also applied a linear magnification for the imaged mires. These two assumptions are approximations compromising the algorithm's accuracy. Using a sphere of known radius of curvature the angles are then calculated based on the image ring mire heights.

In the second part of the algorithm the position of the reflecting surface vertex was calculated using the angles determined in the first part for the first image ring mire only. It uses the same assumptions as the first part and a paraxial approximation in the calculation. The first mire is very close to the instrument axis hence the approximation is adequate. The vertex position is calculated for several semi-meridians and then averaged. In the third part an iterative procedure is used to find the position of the reflection point of the next mire based on the data from the previous one. It uses data acquired in the first two parts and is a modified Euler method that starts by considering that the next corneal reflection point has a tangent equal to the previous point. After that a new tangent is calculated based on

the reflection angles and the process is repeated until the difference on two successive iterations is below a pre-determined value.

The authors tested the procedure on five steel spheres of radii 5.5, 7, 8, 9 and 11 mm resulting in an average error of 0.2% on radius of curvature. From their data the maximum error on radius of curvature was 0.04 mm for the 11mm sphere.

2.3.17 *Laskin and Puryayev algorithm*

Laskin and Puryayev (1995) built a telecentric videokeratoscope with collimated mires employing an unusual design. The faceplate mires were not observed directly but through a collimating lens. The mires were located in a meniscus with a curvature equal to the curvature of the lens focal plane. This design makes any pencil of rays from any point in any mire to arrive parallel at the corneal surface (collimation). The telecentric principle only allows rays parallel to the instrument axis to enter the instrument pupil. The combination of these two features makes the calculations much easier. They reconstruct each semi-meridian separately fitting a conic section by a least squares method.

The algorithm was tested on a 10.02 mm radius sphere and a paraboloid with apical radius of 6.08 mm. They present an error of 0.03 mm on the sphere radius and an error of 0.11 mm on the apical radius of the paraboloid.

2.3.18 *Halstead et al. algorithm*

Halstead et al. (1995) resorted to polynomial splines to represent surface information as a continuous data set. Algorithms that reconstruct each semi-meridian at a time are criticised since they are more prone to error if asymmetric surfaces are used. The algorithm starts by shifting the position of a 9 mm apical radius paraboloid until it reaches a surface point determined by an ordinary reconstruction algorithm. At each iteration a backward ray trace is executed using the approximated surface. First a ray is traced from the image mires in the CCD plane passing through the nodal points of the objective reaching the surface at a

given point. The surface normal at that point is then used to trace the reflected ray. If this ray doesn't intersect an object ring mire edge, then the approximated surface has an error. This error was quantified by the dot product of the tangent vector to the surface at that point with the desired normal vector that would make the reflected ray intersect the closest point on the object mire. If the surface is adequately reconstructed the dot product is zero. The approximated surface is then replaced by another surface that minimises the error by a least squares method. The iterations are repeated until the squared error values of the dot product representing the error falls below 1% of the sum. This algorithm is adequate for non-symmetrical surfaces since it considers the hypothesis of the incident and reflected rays in different meridians (skew rays).

The algorithm was tested on three spheres of 7, 8 and 9 mm radius and a computer simulation of the image reflected from a non-rotational symmetric ellipsoid. They report a root mean square error in sag reconstruction of 8.5 nm for the ellipsoid and 0.7, 0.8 and 1.4 μm for the 7, 8 and 9 mm spheres respectively.

2.3.19 *Brenner's algorithm*

Brenner (1997) disclosed the algorithm used by the TMS2 videokeratoscope. The cornea is reconstructed by a sequence of spherical surfaces with centres on the instrument axis. Using a calibration sphere of known radius, at each sample point in the image (defined by the coordinates ring number, semi-meridian), the radius of the sphere is divided by the image ring mire height defining a coefficient *c*. The coefficients for all sample points are then stored. When analysing an unknown surface the coefficient *c* (determined for the calibration sphere) for a given sample point is multiplied by the ring image mire height for that point. This will result in an estimate of a radius of curvature for that point. Note that this radius would be accurate only if the unknown surface was equal to the calibration sphere. Therefore a different correction factor must be applied to each radius of curvature. The correction factors are based on the application of the same methods to two other spheres of known radius of curvature. The radial coordinate of the analysed

corneal point is obtained by linear magnification from the image on the CCD plane. Knowing the radial coordinates and the sagittal radius of curvature (see section 3.1.1 for definition) for each corneal point, they reconstruct the surface using circular arcs. Each arc will be positioned with the corneal point in the middle. Since the several arcs will not be joined in their extremities they are translated in order to do so. However this will result in a loss of smoothness at the arcs junctions, like a sequence of bumps. The author does not mention this problem. No testing of the algorithm was reported.

2.3.20 *Campbell's algorithm*

Campbell (1997) disclosed the algorithm used in the Mastervue videokeratoscope. This instrument uses a unique concept, the cone of focus. Ring number 10 is located away from the faceplate in an inner cone with the same apical angle as the faceplate and opposite base (Figure 2.3). Therefore when the instrument executes an axial displacement there is a differential movement between the image of ring 10 and the images of rings 9 and 11. When the image of ring 10 is located in the middle of the images of rings 9 and 11 the incident ray is directed along the direction of the cone of focus.

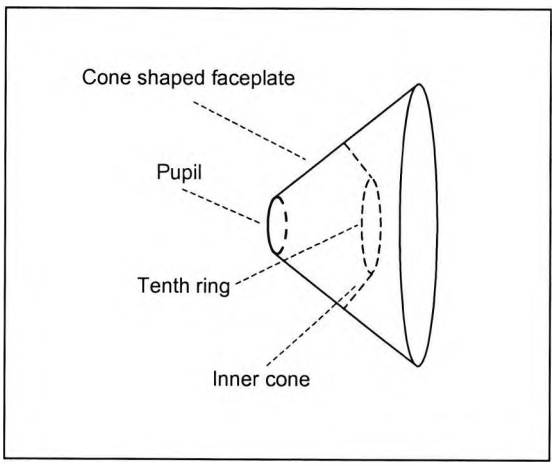

Figure 2.3 – Cone shaped faceplate of the Mastervue videokeratoscope. All rings are located on the faceplate inner surface except for ring 10. This ring is located in an inner cone with the same apical angle as the faceplate and with opposite base.

Knowing the direction of the incident ray, the image position and considering that the reflected ray is directed to the nodal point of the CCD camera objective, the position of the corneal reflection point is determined. Using the van Saarloos' algorithm backwards, the position of the corneal vertex is located for the horizontal semi-meridians (0 and 180°) and averaged. The surface is then reconstructed using the van Saarloos algorithm. The author claims that the system is able to measure differences in surface elevation up to 1 μm.

2.4 *Keratoscope alignment*

Mandell (1992) mentions that although Placido disk-based videokeratoscopes use slightly different alignment procedures, they are all based on the same principle. The subject fixates on a point on the instrument optical axis and its reflection on the corneal surface is used to place the instrument perpendicular to the cornea at the point of intersection with the instrument axis. This is achieved by overlapping the image of the fixation light with a mark on the centre of the screen, which marks the instrument axis. The corneal point where the fixation light is reflected can be in the centre or slightly more to the corneal periphery. Mandell suggests that the instrument should be directed to the entrance pupil centre, however he acknowledges that in this case the instrument optical axis wouldn't be perpendicular to the cornea. Since the majority of reconstruction algorithms need this condition to be met, there would be the need to develop new algorithms.

Mandell's centring suggestion follows the work of Uozato and Guyton (1987) in which they state that all surgical procedures should be centred at the line of sight. This should be done since this line corresponds to the centre of the bundle of rays entering the eye.

To achieve a compromise between centration on the line of sight and placing the instrument axis perpendicular to the cornea Mandell (1992) suggested an eccentric fixation point. This would allow for the instrument axis to be directed to the point

where the line of sight intersects the cornea. In another article Mandell (1994) names this point the corneal sighting centre.

2.5 *Decentring, tilt and focus errors*

Placido (1880b) was aware that tilting and/or decentring the cornea would influence the keratoscopic ring mire image. To prevent tilting of the Placido disk he placed a cylindrical tube on the back of the instrument, concentric with the disk aperture. Since the observer would focus on the patient's cornea the disk aperture and the cylinder aperture would be out of focus. However it was still possible to be aware of both apertures while focusing on the Placido disk image. Placido points out that the image of both apertures should be concentric in order to prevent tilting of the instrument. He also placed two dots on the horizontal meridian on each side of the first ring in order to study the effect of patient fixation on the keratoscopic image.

Levene (1962) studied the effect of the self-luminous keratoscope (see 2.1) tilt in the recognition of astigmatic surfaces using 30 observers. Anterior surfaces of toric contact lenses were used instead of human corneas. He concluded that astigmatism detection was difficult if lower than approximately 2.5 diopters. He refers to Gestalt concepts to explain the tendency to perceive ellipses of small eccentricity as circles. He also points out the potential to tilt the instrument in order to obtain a perfect image (circle).

Ludlam and Wittenberg(1966b) also studied the effect of surface tilt in a photokeratoscope. They analysed a tilted reflecting aspheric surface with axial symmetry and a non-astigmatic cornea fixating eccentrically. They used 4 degrees tilt for the former and 8 degrees for the latter. The tilt was done once for the vertical plane and once for the horizontal. They concluded that toricity could be induced from surface tilt. In a centred toroidal surface the ring separations are constant on

opposite sides of the measurement axis. This doesn't happen if the toricity is induced from surface tilt.

El Hage (1972) performed a simple mathematical analysis on the effect of reflecting surface decentration. He concluded that these errors are negligible since the decentration is much smaller than the keratoscope rings (He used a cylindrical keratoscope with rings of equal height).

Fry (1975) mentioned that for reflecting surfaces without rotational symmetry the reflected ray won't lie in the meridional plane. The only exception would be for the principal meridians of the surface. This is important since it also applies to decentred or tilted axially symmetrical surfaces due to loss of symmetry of the system surface – instrument.

Rowsey and Isaac (1983) photographed 6 steel balls with the Corneascope and analysed the surfaces with their spherical biased algorithm (see 2.3.9). They observed that decentration caused ring crowding in the direction of decentration (indicating steepening) and separation on the opposite direction (indicating flattening). However in their algorithms the average hemichord length was the average of all image ring points and the errors would compensate. Therefore decentration did not seem to be a problem.

Penney et al. (1990) used the CMS videokeratoscope to analyse a reflecting sphere of 7.94 mm radius equivalent to 42.5 D. They mention that when the sphere was displaced in the direction of the instrument, from the best focus position, the reflected mires increased in size, corresponding to a larger radius of curvature. The opposite happened when the sphere was displaced away from the instrument. They calculated an average 0.1 D change for each 50 μm displacement from the best focus position.

Fisher and Applegate (1990) used the TMS on spherical steel balls of 7, 7.5 and 8 mm radius of curvature. They misaligned the instrument until the limits of the alignment box obtaining an error of approximately 0.875 D.

Wang et al. (1991) investigated the effects of astigmatism and misalignment on surface reconstruction. Their work can be considered a cornerstone on corneal topography. They resorted to ray tracing in three dimensions, using an ellipsoid with three different axes as an astigmatic surface. Two of the axes remained unchanged and the third changed in order to produce different degrees of astigmatism.

Their study shows that the skew ray error (difference of object and image meridian) increases with the degree of astigmatism and is maximum near the meridian bisecting two of the surface principal axes. They also realised that it is not possible to focus an entire image ring from an astigmatic reflecting surface. When focusing in the horizontal meridian the vertical will be out of focus. The total error will be the sum of the defocusing error across a ring, the skew ray error and the error associated with reconstruction algorithms when dealing with aspheric surfaces. In some points these errors will aggregate and in others they will compensate. Therefore it isn't possible to analyse the effect of the skew ray error as a single source. However when analysing the error for all rings in a semi-meridian the reconstruction error was larger when compared with a spherical surface.

Wang and co-workers also analysed the effect of decentration with a 8.33 mm sphere. They report that the image rings are compressed in the opposite direction of shift and will separate in the direction of shift. They estimated a 0.5 D error for each mm of shift. However videokeratoscope alignment systems won't allow that magnitude of shift. The tilt effect was analysed on a rotational symmetric ellipsoid (non-astigmatic on xy) for several tilt angles. The simulation results for the first and last ring were compared to the centred ellipsoid and to the tilted ellipsoid. When

compared to the centred ellipsoid the error was larger for the last ring. When compared to the tilted ellipsoid the error was larger for the first ring.

They reported a maximum error of less than 1% on paraxial power maps when comparing the instrument values with their simulation values using centred surfaces. For an average cornea of 43 diopters, 1% of the power is 0.43 diopters which is a significant error. This error can be explained by the fact that they used a single ray to calculate the image of each object point. That ray passed through the principal point of the camera lens. In addition, once again they appeared to forget the distance from the instrument pupil to the reflecting surface vertex. This happened previously in the article from Wang et al. (1989) (see 2.3.11).

Mandell (1992) tested two well known videokeratoscopes, the TMS and the Eyesys, concluding that the instrument with the shorter working distance was more sensitive to focusing errors. He also mentions that the same instrument is more sensitive to decentration errors but didn't present any proof. He based his findings on the analysis of a single reflecting sphere of 7.94 mm radius.

Mandell et al. (1992) tested 10 subjects with standard videokeratoscope alignment and alignment at the line of sight. They found maximum radius of curvature differences of 0.09 mm for central rings and 0.16 mm for peripheral rings.

Nieves and Applegate (1992) tested the TMS and the Eyesys with two spheres of 7.115 and 7.95 mm radius. They tested defocusing and decentration concluding that the first parameter leads to larger errors which were more significant for the instrument with shorter working distance. The error was 0.9 D for a defocusing of 0.33 mm in the direction of the instrument.

McCarey et al. (1992) tested the Eyesys software version 1.75 in a 47 D sphere. It accepted decentrations up to 0.6 mm, from then the accuracy dropped sharply. However their error graphs for decentration and defocus are scaled in 5 D intervals

and do not allow a proper analysis. From those graphs they concluded that small decentration and defocus do not significantly alter data.

Mellinger et al. (1993) tested the TMS1 and the Eyesys on toroidal surfaces until 7 D of astigmatism. The surfaces were verified by interferometry and profilometry. Focusing errors were more significant for the instrument with shorter working distance with 2.7 D per mm of defocusing. Decentration errors were not significant for misalignments of ±0.4 mm.

Legeais et al. (1993) tested the TMS1 on six PMMA spheres checked with a radius gauge to an accuracy of 0.02 mm. They mounted the TMS1 head on a micrometer stage (therefore modifying the instrument). Steeper readings were observed in the direction of decentration and flatter in the opposite direction. Decentration error increased with surface power. Although they claimed to have tested decentrations in the range 100 to 300 μm, they just report a maximum error of 0.2 D for 100 μm neglecting to mention results for other decentrations. Focusing errors also increased with power. Defocusing magnitudes of 250 and 500 μm were studied with the amount of error doubling from the former to the latter defocusing magnitude. Focusing errors were larger than decentration errors. At 500 μm defocus they obtained 0.5 D error for a 43 D sphere and 2.3 D for a 60 D sphere.

Roberts (1994a) analysed the Eyesys, concluding that focusing errors were larger than misalignment errors. She also concluded that the latter were small when compared with the spherical biased reconstruction algorithm inherent error. An ellipsoid with 7.5 mm apical radius, an eccentricity of 0.5 and a diameter of 10 mm was used in the study. This surface was verified by Rank Hobson Talysurf profilometry.

Hubbe and Foulks (1994) used the Eyesys in normal corneas and three aspheric surfaces with 7.4, 7.7 and 7.9 mm apical radius. The normal corneas were tilted 2.5, 5 and 10 degrees and the surfaces 1, 2, 3, 4, 5, 10 and 15 degrees. They

observed that the asymmetry of the bow tie pattern, presented in the dioptric colour map, increased with the angle of tilt. They also used the I-S value, which is an index that compares the steepness of the superior and inferior cornea, that is usually applied in the detection of keratoconus (for more details on this index see Rabinowitz et al. 1990). Three of the five normal eyes tilted 5 degrees would be classified as keratoconic by the I-S index. This index increases with surface tilt. They also observed that the tilting effect on the maps increased with the steepness of the surface apical radius.

Mandell et al. (1995) compared standard videokeratoscope alignment with alignment at the corneal apex and at the corneal sighting centre. The Eyesys model 2 was used for this study on the right eyes of 20 subjects. They found differences smaller than 0.5 D for central power, toricity and axis when comparing standard and corneal sighting centre alignment. Differences were larger with apex alignment compared with standard, being larger than 1 D at the periphery.

Suchecki et al. (1995) studied fixation effects on the dioptric maps of 7 eyes calculating the I-S index. At 7.5 degrees tilt the maps displayed a pseudokeratoconus pattern but the I-S index did not indicate keratoconus. They also analysed focusing errors in four spheres. Each image was defocused 250, 500 and 750 μm in both directions. They reported a power increase of +0.45D focusing 750 μm away from the spheres and –0.57 D with the same amount of defocusing towards the spheres.

Laskin and Puryayev (1995) claimed to have built a videokeratoscope insensitive to alignment errors, however their results show otherwise. They tested a 10.07 mm radius sphere and an axial symmetric paraboloid with an apical radius of 6.08 mm. They do not mention how the surface parameters were checked. With 1 mm decentration the sphere radius error was 0.05 mm and the paraboloid apical radius error was 0.12 mm. For a 1 mm defocus the sphere radius error was 0.05 mm and the apical radius error for the paraboloid was 0.14 mm.

Mandell et al. (1996) used the Eyesys model 2 on 16 subjects presenting asymmetric corneal toricity, known as an asymmetric bow tie pattern on the colour dioptric map. When changing from regular alignment to alignment on the corneal apex the majority of maps became more symmetric. Half the subjects presented a difference of more than 1 D in the corneal periphery. When suspecting keratoconus from inferior steepening in the colour dioptric maps, they noted that in true keratoconus there was a large increase in power when apex alignment was applied.

Douthwaite et al. (1996) developed a model to estimate surface tilt based on ring image displacement for a telecentric videokeratoscope. They used a mathematical model of an axial symmetric ellipsoid represented by Baker's equation. It is well known that when the reflecting surface is tilted the centre of the image rings shifts in relation to the centre of the inner ring. They considered the fifth ring and measured its centre displacement. They claimed that this shift is directly proportional to the amount of tilt and a linear relationship exists between both parameters until 10 degrees tilt. If a first image is captured with regular alignment and then a second image with the subject fixating on an eccentric point the tilt angle from the first to the second position can be calculated. The tilt and fifth ring displacement difference between both situations are used to determine the gradient of the straight line that defines the linear relation. Since for zero tilt there is no ring displacement the line must pass through the origin, which is zero intercept. The tilt on the first position can then be determined from the line. They applied the model to four ellipsoids and ten human corneas using the Eyesys (this instrument has 16 rings) applying the principle to all rings. They observed inconsistent results for rings 1 to 5 (central rings). For the ellipsoids the calculated tilt angle was close to the real value (less than 0.5 degrees error). Their work suggested that typically normal corneas will have a tilt angle of approximately 5 degrees, which doesn't result in a significant error on surface reconstruction (determination of apical radius and *p* value). When they applied the model to real corneas the subject's fixation

was changed according to the calculated tilt angle and the dioptric maps displayed improved symmetry.

Analysing their work it can be seen that the mathematical model was developed for a telecentric videokeratoscope which limits its scope. However they showed that it works fairly well for the Eyesys since even though it is not a telecentric instrument, it has a large working distance that approaches a telecentric system (due to the fact that for a larger distance the rays will be approximately parallel). Secondly, if the linear relationship between image ring displacement and tilt is accepted, it will only be adequate if the initial surface tilt and the fixation induced tilt are in the same direction. This was in fact what happened in the controlled conditions of their experiment since they knew the initial surface tilt direction. However for a real cornea the initial tilt direction is unknown therefore the second tilt direction may be different which would decrease the model's accuracy. Perhaps it would be possible to estimate the initial tilt direction based on the direction of ring crowding.

Chan and Mandell (1997) studied alignment effects on keratoconic, non-contact lens wearers subjects using the Eyesys software version 2.10. Normal alignment was compared with alignment at the apex and 1 and 2 mm below the apex. They reported that apex alignment resulted in larger dioptric values than standard alignment. Sagittal power errors can be as great as 8.32 D and 7.1 D for toricity. Tangential power is better to represent keratoconus since it is less dependent on the chosen axis.

Campbell (1997) analysed the skew ray error effect on reconstruction, arriving at a similar result to Wang et al. (1991). The difference in the analysis system is that Campbell expressed the surface normal in terms of a mean curvature and two cross cylinder components. Another interesting approach was to use the projection of the normal and the projection of the incident ray in the meridional plane. Since Snell's law still holds for these projections, the skew ray error problem is reduced to an incorrect height of the object point in the meridional plane.

Oltrup et al. (1997) developed a system for compensation of defocusing errors in videokeratoscopy. It was applied to the C-Scan instrument. The system requires a colour CCD camera, a red diode Laser and a green fixation light on the videokeratoscope axis. The red diode laser is placed in the instrument faceplate projecting a beam intersecting the videokeratoscope axis at the point where the image plane intersects the axis. Based on the lateral displacement of the red and green lights on the cornea and using paraxial magnification formulas, a correction is calculated for the height of each ring mire image. They tested the system on a single sphere of 8 mm radius of curvature obtaining a maximum error of 0.25 D in the defocus range of ±1.5mm. This result suggests that the system works well, however it should have been validated on other surfaces, including non-spherical ones. The system is based on paraxial formulas hence it shouldn't be adequate for peripheral rings. Another problem seems to be the way that the distance between the red and green lights on the corneal surface is calculated. They say "The relative position of the laser beam (red dot) and of the fixation light (green dot) on the corneal surface is then captured.", which implies a direct measure. Although this can be achieved due to the scattering properties of the cornea, it would require focusing the instrument on the corneal surface. However this is not the case, the instrument focus is on the image plane of the ring mires which would make the scattered light on the cornea barely visible. I believe the instrument measures instead the reflected image of the red and green lights on the image plane. Considering that the red Laser beam is reflected in the direction of the nodal point of the CCD camera's objective, the reflection point on the cornea can be determined. Since the green light is directed axially, the distance to the red laser reflection point on the cornea can then be determined.

Higaki et al. (1997) analysed the automatic misalignment correction on the TMS2 videokeratoscope. They used four calibration surfaces, one spherical, two elliptical (one prolate and the other oblate) and a toroidal. Each was misaligned 0.1 and 0.2 mm in the horizontal direction and defocused 0.25 and 0.5 mm. Sagittal, tangential

and refractive power maps showed no marked differences on the colour coded patterns. They do not mention if the absolute or normalised scale was used and seem to base their analysis on visual inspection of the maps.

Hilmantel et al. (1997) used the TMS1, software version 1.41, on calibrated ellipsoidal surfaces tilted 5, 10 and 15 degrees towards the 90 degrees semi-meridian. The accuracy of the elevation maps varied according to the analysed semi-meridian increasing with tilt yielding a 14.8 μm root mean square error for the largest tilt.

Klein (1997) used cylindrical coordinates to represent corneal shape, using a left handed axis system. If the corneal normal lies in the meridional plane, as in the case of an axial symmetric surface, there is only one definition for axial distance which ranges from a corneal point to the instrument axis measured along the surface normal. He states that when the corneal normal doesn't lie in the meridional plane three definitions of axial distance are possible since the normal does not intersect the instrument axis. He named meridional axial distance the one ranging from the corneal point to the instrument axis measured along the projection of the normal in the meridional plane. The closest approach axial distance is the one ranging from a surface point to the point closest to the instrument axis measured along the normal direction. Finally the videokeratoscopic axial distance (d_v) is the one measured by videokeratoscopes for very small corneas according to the author. It is also measured along the surface normal and meets the condition $d_v = h / \sin\sigma$ where h is the radial coordinate of the corneal point and σ is the angle between the normal and the instrument axis. All these definitions consider a centred surface.

Klein based his skew ray error analysis on the differences between the different definitions of axial curvature calculated by the inverse of axial distance. For a centred ellipsoid the difference is negligible. It is only significant for keratoconus, which he simulated by a bi-sphere, especially in the transition zone.

Douthwaite and Pardan (1998) following on from their work started in 1996, tried to predict surface tilt based on a single keratograph rather than two as presented in their previous work. For each reflected ring on a tilted surface they determined the quotient between opposite hemi-chords in the tilt semi-meridian. They found a linear relation between this quotient and the tilt angle of the surface, using different surfaces tilted at several angles. They do not specify which surfaces were used but these were probably axially symmetric ellipsoids. The slopes of the regression line changed with the surface *p* value but were fairly independent of apical radius. Another parameter used in the equation was the gradient determined by the *p* value. This was calculated plotting a graph of the slopes of the regression lines of the graphs (quotient versus tilt) versus the *p* value of the surfaces. All these steps were applied to each image ring separately. The final tilt was then calculated by averaging the tilt calculated from each image ring data. Testing the model on calibrated convex conoidal surfaces they found the results would be better if a subtraction of 0.4 degrees was applied to the final tilt angle. They report a ± 0.6 degrees difference (95% confidence interval) in relation to their previous method.

Sayegh et al. (1998) tested three approaches on focus correction. The first using geometrical optics, the second a nomogram obtained from measurements on known surfaces and the third based on neural networks. They report corrections of 2 to 3 diopters. No further details are given.

Hilmantel et al. (1999) tested the TMS1 software version 1.61 to measure tilted ellipsoidal surfaces. The three surfaces had eccentricities of 0.6 and apical radius of 7.03, 7.99 and 9.37 mm all calibrated by interferometry. Each was tilted 5, 10 and 15 degrees using a Meles Griot goniometer. They found that the accuracy was independent of the surface apical radius with a trend to a greater error towards the surfaces periphery. Results were given regarding surface elevation measurements.

Munnerlyn et al. (2000) analysed bicurve surfaces tilted 0, 3, 6, 9, 12 and 15 degrees, using the Humphrey Atlas videokeratoscope and the Orbtek Orbscan. Both devices overmeasured the radial position of the central curvature section with the location error increasing with the tilt angle. The Humphrey Atlas produced a more accurate elevation measurement.

In summary, from the review on keratoscopy (section 2.1) it can be seen that the concentric ring pattern was considered as the most adequate target since 1881. Keratoscopes, which used visual inspection evolved to photokeratoscopes that recorded the reflected ring pattern on a photograph for subsequent analysis. Nowadays the videokeratoscopes use CCD cameras connected to computers, the image is captured and immediately analysed.

From the review on faceplate design (section 2.2) it was seen that the faceplate shape has evolved from the original flat design to allow for a larger coverage of the analysed corneal area and to decrease field curvature. Only a few papers can be found in this subject and it seems that this research topic has been abandoned since 1971. Nevertheless there are several faceplate shapes available on commercial instruments, therefore this topic should be subject to further study.

From the reconstruction algorithm review (section 2.3) it was concluded that it isn't possible to reconstruct the corneal shape without resorting to some approximations. This is due to the fact that it is not possible to reconstruct a three-dimensional surface with two-dimensional information. While some approximations are more acceptable than others, each investigator assessed his algorithm's accuracy with different surfaces. The only way to compare all the algorithms would be to analyse the same set of surfaces, which has never been done.

From the keratoscope alignment review (section 2.4) it was concluded that keratoscopes can detect surface decentration and are equipped with means to

avoid it. However surface tilt cannot be detected since a correct alignment can be achieved in such conditions. This is a topic that needs further research.

From the decentration, tilt and focus errors research (section 2.5) it can be concluded that focusing errors are more important than tilt and decentration errors and that short working distance instruments are more affected by these errors. The majority of the research on this field has been done by analysing one surface or a small number of surfaces. Since all researchers used different surfaces the studies cannot be compared. Only one group of two investigators developed a method to determine the magnitude of tilt from videokeratoscopic images, however it still presents limitations. Another group of researchers developed algorithms for focus correction but do not present details on the methods. Other focus correction algorithm was developed but was based on paraxial formulas. The author tested the procedure on a single spherical surface for which it worked well. Further research is needed for the correction of these errors.

Since many parameters and sources of error in videokeratoscopy required further research, a computer simulation of a videokeratoscope was designed. The next chapter presents all the theory applied to the computer model.

3 Computer modelling of a videokeratoscope system

A videokeratoscope system can be divided into four parts: faceplate, alignment system, CCD camera and a computer. The parameters of the reflecting surface to be analysed can also be changed in the computer model. The faceplate commonly consists of a series of illuminated concentric rings positioned coaxial to the instrument.

An alignment system is designed to position the reflecting surface coaxial with the videokeratoscope axis. This process is very important since reconstruction algorithms assume that alignment has been achieved. Unfortunately an ideal alignment system hasn't been developed therefore small alignment errors will always be present. Information on these systems, as part of an overview on corneal topography, has been compiled by Gills et al. (1995).

The CCD camera captures the image of the faceplate rings reflected by the cornea. Analysis of CCD cameras is beyond the scope of this work. The computer then analyses the image detecting the position of the ring edges along a pre-defined number of semi-meridians. This data is then used to build a dioptric power map or a topography map, reconstructing the reflecting surface.

3.1 *Faceplate Model*

Based on the literature review on faceplate shapes and the measurement of several commercial videokeratoscopy systems, cylinders, cones, conoids and flat surfaces were used in the model. The reflecting surface was also modelled by conoids hence there is a need to review the properties of these solids.

3.1.1 General properties of conics and conoids

Greek mathematicians defined conics as curves obtained by the intersection of a plane and a circular cone (Bers, 1969). If the section does not pass through the cone vertex and is parallel to the base it results in a circle, while a section parallel to the cone generatrix (line that generates the cone if rotated around the central

axis) results in a parabola. Sections with an inclination ranging from the plane parallel to the base and the generatrix inclination result in ellipses and sections perpendicular to the base result in hyperbolas.

Geometrically these curves can be defined in relation to two parameters, a straight line (directrix) and a point (focus). Conics are the locus of points whose ratio of the distance to the focus to its distance from the directrix is constant (Grieve, 1926). This ratio is called eccentricity and takes a particular range of values for each curve.

The general equation for a conic can take several forms (Townsley, 1970). The one chosen for this study is often referred to as Baker's equation (Baker, 1943)

(3.1) $$y^2 = 2Rz - pz^2 .$$

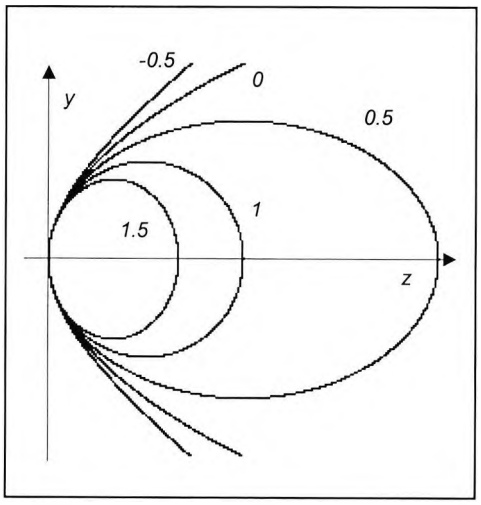

Figure 3.1 - Family of conics with the same apical radius of curvature. Each curve is associated with a *p* value (number displayed near each curve) that relates to the way the curvature changes from the centre to the periphery.

Although he did not derive this equation, his paper is one of the earliest references found in the ophthalmic literature and hence the equation became associated with

his name. The equation is advantageous since it is possible to define a conic in terms of its apical radius of curvature (*R*), which is the radius of curvature at the surface apex, and just one other parameter, the *p* value, which is related to the way the curvature changes from the apex to the periphery (Figure 3.1). The *p* value can be understood as a measure of deviation from a circle. Baker's equation represents the various conic sections with vertex at the axis system origin.

The common equations for an ellipse and a hyperbola (Bers, 1969) can be decentred along the *z*-axis in order to be equivalent to Baker's form. They are respectively

(3.2) $$\frac{(z-a)^2}{a^2}+\frac{y^2}{b^2}=1$$

and

(3.3) $$\frac{(z+a)^2}{a^2}-\frac{y^2}{b^2}=1.$$

For an ellipse, 2*a* and 2*b* are the major and minor axis respectively or vice-versa depending on which value is bigger. For a hyperbola 2*a* is the transverse axis and 2*b* the conjugate axis (*a*>0 and *b*>0). The relation of both parameters with eccentricity for an ellipse (only if a>b) and for a hyperbola are respectively

(3.4) $$e=\sqrt{\frac{a^2-b^2}{a^2}}$$

and

(3.5) $$e=\sqrt{\frac{a^2+b^2}{a^2}},$$

(Grieve, 1926). Comparing the decentred common equations with Baker's form it can be demonstrated that for an ellipse $a=R/p$ and $b=R/\sqrt{p}$. For an hyperbola ($p<0$) the relations are $a=-R/p$ and $b=R/\sqrt{-p}$ (Bennett, 1988). The p value is related to the eccentricity by

(3.6) $$p = 1 - e^2,$$

which is only valid if $p \leq 1$. Further discussion into the different parameters can be found in the work by Lindsay et al. (1998). Table 3.1 summarises the values of parameters e and p for conics.

	Oblate ellipse	*Circle*	*Prolate ellipse*	*Parabola*	*Hyperbola*
e		0	$0 < e < 1$	1	$e > 1$
p	$p > 1$	1	$0 < p < 1$	0	$p < 0$

Table 3.1 – Values of the parameters e and p relating to the curvature change from the centre to the periphery of a conic arranged by curve type.

If the conic is rotated around its axis, a rotational symmetric surface is generated, a conoid (Borowski and Borwein, 1989). A conoid with vertex at the point $(x_v, y_v, 0)$ can be represented by

(3.7) $$(x - x_v)^2 + (y - y_v)^2 = 2Rz - pz^2,$$

where the parameters have the same meaning as previously. This equation will be very useful for representing a decentred reflecting surface in the xy plane controlled by the vertex position. The normal vector to this surface can easily be obtained by application of the gradient operator and dividing it by its magnitude (Welford, 1986) resulting in

(3.8) $$\hat{n} = \frac{\left[-c(x - x_v) \quad -c(y - y_v) \quad 1 - cpz\right]}{\sqrt{1 - 2c(p-1)z + c^2 p(p-1)z^2}}.$$

The parameter *c* is the curvature, the inverse of the apical radius of curvature *R*. The signs were selected in order for the normal to point inside the conoid. Surface normals are needed for ray tracing to determine the direction of a reflected ray.

The gradient of the two asymptotic lines for a hyperbola is the ratio between the conjugate axis and the transverse axis ± *b* / *a* (Grieve, 1926). This ratio can be shown to be equal to $\pm\sqrt{-p}$ (Bennett, 1988). If the vertex is at the origin, as in Baker equation, the lines are represented by

(3.9) $$y = \pm\sqrt{-p}z \pm \frac{R}{\sqrt{-p}}.$$

For a decentred rotational symmetric hyperboloid the asymptotic lines generate an asymptotic cone defined by

(3.10) $$(x - x_v)^2 + (y - y_v)^2 = -p\left(z - \frac{R}{p}\right)^2.$$

A cone can be represented by an hyperbola with zero apical radius. Baker 's equation will then take the form

(3.11) $$(x - x_v)^2 + (y - y_v)^2 = -pz^2.$$

This cone has its apex at the origin whereas the cone represented by equation(3.10), associated with the hyperbola, has its apex on the hyperbola centre to the left of the origin. The *p* value associated with the cone controls its apical angle and is negative.

The reflecting surface and the faceplate are going to be limited by specifying the maximum diameter (*MAXD*) allowed in the *xy* plane, since only rotational

symmetric surfaces will be used. The section of the surface with diameter *MAXD* is a circle represented by the equation $(x-x_v)^2+(y-y_v)^2 = (1/4)MAXD^2$ (this circular section is the end of the surface while the beginning of the surface is the circular section correspondent to the pupil diameter). The z coordinate corresponding to the specified limit will be needed for several purposes and will be calculated from the decentred form of Baker's equation(3.7). As in all second degree equations when determining the value of *z* for a given pair (*x*,*y*), a maximum of two solutions can be found. The selected solution for the purpose of this simulation was the one with the vertex touching the origin given by

(3.12) $$z = \frac{R - \sqrt{R^2 - p\left[(x-x_v)^2 + (y-y_v)^2\right]}}{p}.$$

To determine the *z* coordinate for the beginning or the end of the surface, the quadratic term in *x* and *y* (corresponding to the equation of a circular section) is replaced by $(1/4)PUPD^2$ or $(1/4)MAXD^2$ respectively. Analysis of the previous equation shows that it is not valid for p=0, a paraboloid. This is because such a conoid is a first degree equation on *z* thus having a single solution

(3.13) $$z = \frac{(x-x_v)^2 + (y-y_v)^2}{2R}.$$

The sagittal or axial radius of curvature is the distance from a surface point to the surface axis measured along the normal direction to the surface at that point. Smith (1966) presented the sagittal radius expression for a conic curve, which can easily be transformed for a decentred conoid resulting in

(3.14) $$R_s = \sqrt{(x-x_v)^2 + (y-y_v)^2 + (R-pz)^2}.$$

The tangential, instantaneous or local radius of curvature is the distance from a surface point to the instantaneous (local) centre of curvature, for that point,

measured along the surface normal. The formula for the tangential radius for a general plane curve (Bers, 1969) is given by

$$R_t = \frac{\left[1+\left(\frac{dy}{dz}\right)^2\right]^{3/2}}{\frac{d^2y}{dz^2}}. \tag{3.15}$$

It can only be applied to curves of second degree or higher whose second derivative at the desired point is different from zero. Smith (1966) applied this equation to a conic curve but the results are also valid for a decentred conoid. He obtained the relation

$$R_t = \frac{R_s^3}{R^2}, \tag{3.16}$$

that when applied to the surface vertex $(x_v, y_v, 0)$ results in the apical radius of curvature R.

The width of the rings on the faceplate has to be determined to check if they are too thin since very thin rings would have a poor illumination. By visual inspection of rings on several videokeratoscopes, an inferior limit of 0.5 mm width was considered. Since they follow the faceplate curvature it is the arc length that has to be determined for this purpose. The process of finding the length of an arc of a curve is called rectification (Edwards, 1930). If a curve is expressed in its Cartesian form $z=f(y)$, the corresponding arc length is

$$s = \int \sqrt{1+\left(\frac{dy}{dz}\right)^2}\, dz. \tag{3.17}$$

The arc length for a circle of radius R is expressed by a well-known formula $s=\theta R$ (Bers, 1969), where θ is the angular amplitude of the arc described at the circle centre (Figure 3.2). This expression is the solution of the integral in equation(3.17) for a circle. As stated previously Baker's equation represents conics with vertex at the origin. Due to the symmetry in relation to the z-axis it is sufficient to work with the top part of the faceplate as represented in Figure 3.2. However the limits of the object rings on the faceplate are going to be expressed in z-coordinates therefore the angular amplitude θ of a ring must be calculated accordingly. In such conditions the arc length s between z_1 and z_2 is

$$s = \theta R = (\varepsilon_2 - \varepsilon_1)R = \left[\arccos\left(\frac{R - z_2}{R}\right) - \arccos\left(\frac{R - z_1}{R}\right)\right]R. \tag{3.18}$$

Angles ε_1 and ε_2 are positive as defined in the figure and were only used as auxiliary angles to get to the final expression.

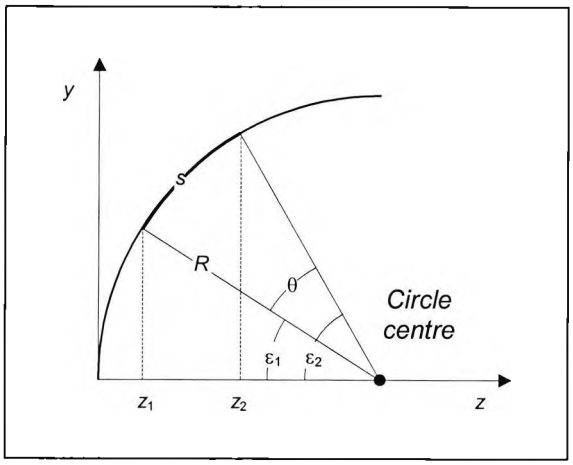

Figure 3.2 – Arc length of a circle between two z coordinates.

For a decentred ellipse expressed in the common form, the arc length formula (equation(3.17)) is

(3.19) $$s = \int_{z_1}^{z_2} \sqrt{1 + \frac{b^2}{a^2} \frac{(z-a)^2}{a^2 - (z-a)^2}} dz .$$

Executing the substitution $z = a + a \cos t$, this expression takes the form

(3.20) $$s = -a \int_{\arccos\left(\frac{z_1 - a}{a}\right)}^{\arccos\left(\frac{z_2 - a}{a}\right)} \sqrt{1 - e^2 \cos^2 t} dt .$$

Without the constant $-a$ this is known as Legendre's elliptic integral of the second kind and can only be solved numerically (Edwards, 1930). Therefore can only be solved numerically in equation(3.19).

The arc length formula for a decentred hyperbola is

(3.21) $$s = \int_{z_1}^{z_2} \sqrt{1 + \frac{b^2}{a^2} \frac{(z+a)^2}{(z+a)^2 - a^2}} dz .$$

Edwards(1930) has shown that this integral can be rearranged in another form that includes the Legendre elliptical integral of the second kind, which again can only be solved by resorting to numerical methods.

The integrals in equations (3.19) and (3.21) can be merged into the form

(3.22) $$s = \int_{z_1}^{z_2} \sqrt{1 + p \frac{\left(z - \frac{R}{p}\right)^2}{\frac{R^2}{p^2} - \left(z - \frac{R}{p}\right)^2}} dz ,$$

considering the relations between the parameters *a*, *b*, *R* and *p* for each curve. It has an obvious problem at the vertex, where z=0 (and also *z=R/p*), since the tangent to the curve is vertical (the first derivative is infinite). Outside these points it can be used without problems. It has the advantage of combining the arc length for the ellipse and hyperbola in a single formula and can be used for oblate ellipses (*p*>1).

For a parabola the arc length is given by the integral

(3.23) $$s = \int_{z_1}^{z_2} \sqrt{1 + \frac{R}{2z}}\, dz \,.$$

It can be solved by conventional methods and according to Edwards(1930) the solution is

(3.24) $$s = \sqrt{z_2}\sqrt{\frac{R}{2} + z_2} - \sqrt{z_1}\sqrt{\frac{R}{2} + z_1} + \frac{R}{2}\ln\left(\frac{\sqrt{\frac{R}{2} + z_2} + \sqrt{z_2}}{\sqrt{\frac{R}{2} + z_1} + \sqrt{z_1}}\right).$$

3.1.2 Faceplate parameters

Target shapes were divided into two groups, cylinders and conoids. The flat surface is a special case of the cylinder group and the cone a special case of the conoids group. The faceplate parameters to input are dependent on the group selection.

A flat faceplate is the base of a cylinder with zero length, and is therefore specified by *L*=0 (Figure 3.3). All the surfaces used have rotational symmetry around the *z*-axis and were limited by the maximum specified diameter (*MAXD*). A cylinder has

two parts the base and the cylinder body. In addition to the parameters for a flat faceplate, the body is limited by its length *L*. The pupil is located in the base (z_{PD}=0) and is defined by its diameter (*PD*).

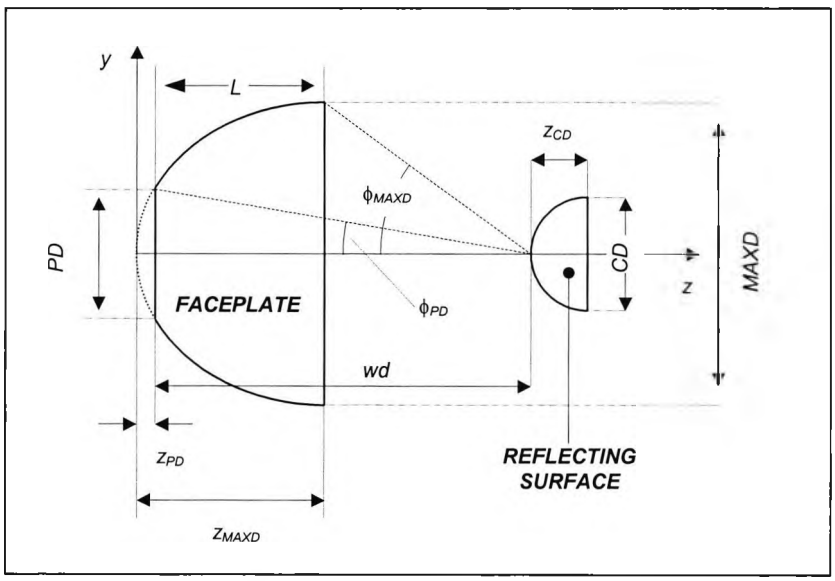

Figure 3.3 - Schematic representation of the model for a videokeratoscopy system used for this research. The main axis system is also represented along with the model parameters.

A cone is a conoid with zero apical radius and a negative *p* value. As stated previously the generatrices have a gradient of $\pm\sqrt{(-p)}$ that will control the aperture angle. The faceplate will begin at z_{PD} calculated by Baker's equation(3.1) where $y=PD/2$.

The pupil diameter has an influence on the faceplate shape that will turn into a cone without the apex (Figure 3.4). The conoid shaped faceplate is similar to the cone, with a non-zero apical radius of curvature and *p* value controlling the peripheral flattening ratio. The surfaces in the conoids group are limited by the pupil diameter (*PD*) and the maximum diameter (*MAXD*).

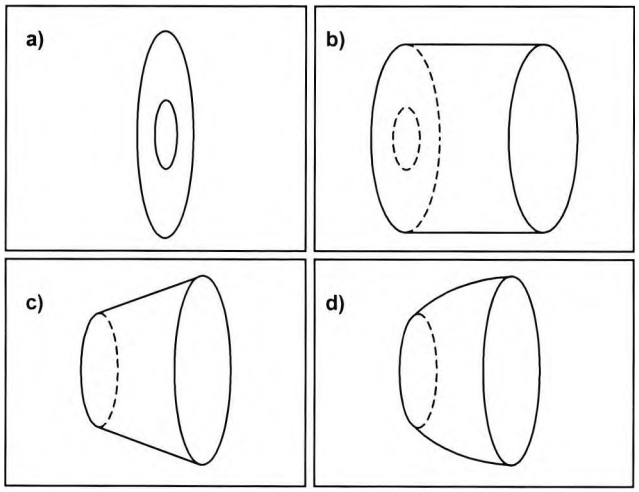

Figure 3.4 - Three-dimensional representation of the four faceplate geometries used. The pupil size limits the area of the surface. For a cone (**c**) and a conoid (**d**) a part of the surface is removed so that it starts at the specified pupil diameter.

3.1.3 Object point selection on the faceplate

As stated previously the faceplate was fitted with a set of concentric rings. These were considered to be at equal angles intervals from the reflecting surface vertex ranging from the pupil edge (ϕ_{PD}) to the maximum diameter (ϕ_{MAXD}), see Figure 3.3. To maximise the number of light rings in the angular space defined the first and last rings must be light, hence the number of dark rings is always one less than the light ones. Therefore if *n* light rings are desired, the angular spacing of each from the reflecting surface vertex is given by

$$\Delta\phi = \frac{\phi_{MAXD} - \phi_{PD}}{2n-1}. \tag{3.25}$$

This maximisation of light rings is needed since they are used as objects.

Theoretically a faceplate should have a large number of rings to generate more data points in the image. If the data points are closer accuracy will increase.

However a large number of rings leads to a decrease in ring width (for conoids this is the arc length calculated by equation(3.17)). Very thin rings will pose a manufacturing problem and the accuracy that could be gained by increasing the rings may be lost in manufacturing errors. Another limitation is that there may not be enough light coming from a very thin ring to trigger an edge detection algorithm. The way around this problem is to increase the brightness of the rings, but this can be very uncomfortable for a patient also leading to a loss of accuracy. Therefore the ring width shouldn't be too small. For the purpose of this research a minimum width of 0.5mm was allowed, although a warning was generated if rings were smaller than 1mm.

The parameter *wd* is input by the user and is the distance from the pupil plane to the vertex of the reflecting surface. It must be bigger than the target length in order to fulfil the condition $\phi_{MAXD}<90°$. When a corneal surface is being analysed in a real videokeratoscope, the light coming from a ring vertically aligned with the corneal vertex ($\phi_{MAXD}=90°$) is blocked by the lashes.

A CCD camera attached to the faceplate pupil is a separate component, it's not built in the pupil. There is a thin cylinder limiting the CCD camera where the objective is assembled. Therefore the first light ring does not start after the pupil but after the outer diameter of the CCD camera limiting cylinder. Although it wasn't measured it was assumed that different manufacturers will use cylinders of different width to limit the camera and so this situation wasn't applied in the model.

An object point on a vertical section of the faceplate is determined by finding the *z* coordinate based on the intersection of the resulting conic with a line describing a given angle with the z-axis. This line intersects the z-axis in the point with a *z*-coordinate equal to the reflecting surface vertex *z*-coordinate. If the reflecting surface is centred, this point is the surface vertex. The intersection with the faceplate will be the same for all semi-meridians due to the rotational symmetry. It is necessary to check if the intersections are on the part of the conic that touches

the origin. As an example, for an hyperbola the intersections of the line with the right branch (touches the origin) are the relevant ones (Figure 3.5a).

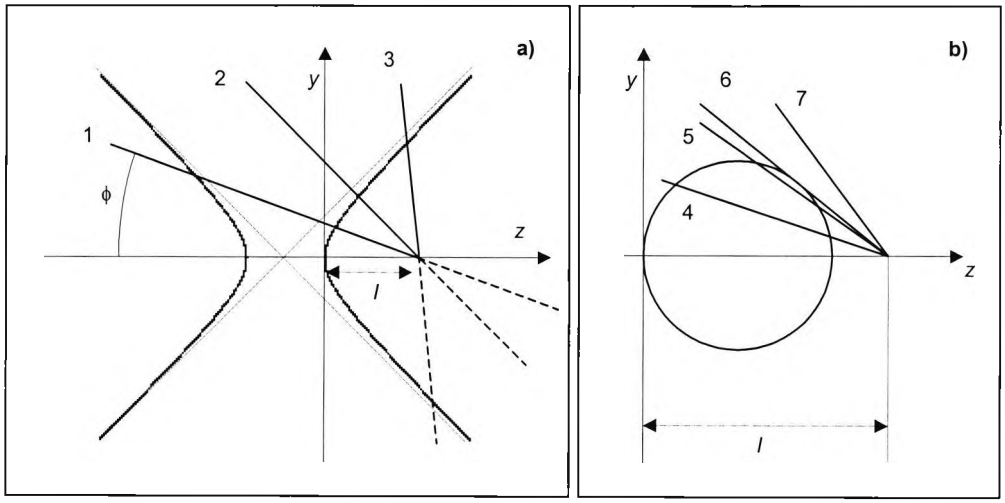

Figure 3.5 - Intersection possibilities of a line with a conic curve.

To determine the intersection *z* coordinate on the faceplate we proceed as follows: A line that passes through a point on axis located at a distance *l* from the origin, to the right, and describing an acute angle ϕ with the axis, is defined by

(3.26) $$y = -\tan\phi(z - l).$$

Angle ϕ was considered positive if above axis. Solving for the intersection of the last equation with the conic defined by Baker's equation(3.1) yields

(3.27) $$\left(p + \tan^2\phi\right)z^2 - 2\left(R + l\tan^2\phi\right)z + l^2\tan^2\phi = 0,$$

which has two solutions given by

(3.28) $$z = \frac{R + l\tan^2\phi \pm \sqrt{\left(R + l\tan^2\phi\right)^2 - \left(p + \tan^2\phi\right)l^2\tan^2\phi}}{p + \tan^2\phi}.$$

The only exception occurs when the second order coefficient in equation(3.27) is zero, in which case there is a single solution

$$z = \frac{l^2 \tan^2 \phi}{2\left(R + l \tan^2 \phi\right)}. \tag{3.29}$$

Line 2 in Figure 3.5 represents this situation, and defines a line parallel to the asymptote in a hyperbola. It is also the case of a parabola (p = 0) when the line is on axis (ϕ=0).

The part of the surface to be used is the branch that touches the origin and by observation of Figure 3.5 it can be seen that the correct intersection (if there is one in the branch that touches the origin) is the one closest to the curve vertex. The selection of the sign before the square root in equation(3.28) has to be done carefully. In the case of a closed surface (p>0) the line will fail to intersect it if the expression inside the square root is negative (line 7). If it's zero it means that the line is tangent to the curve (line 6), but on the wrong branch. If it's positive it can easily be seen that the square root is smaller than the other expression in the numerator, therefore the negative sign before the square root corresponds to the solution closest to the surface apex. However in case both solutions are on the non-desired branch (line 5) it must be considered that the line misses the surface. The same approach is taken when a solution is found in the desired branch but outside the limits specified for it by the program user. For a parabola (p=0) the line cannot miss or be tangent to the surface (in the conditions specified for the line), there are always two solutions and the approach is the same as for the ellipse. For the hyperbola (p<0) the situation is more complex since it will depend on the asymptote inclination ($\sqrt{-p}$). If the line is steeper than the asymptote the denominator is positive and the square root is smaller than the outer expression. Both solutions are on the right branch and the minus sign before the square root corresponds to the desired solution. If the line is less steep than the asymptote the

denominator is negative and the square root is bigger than the outer expression. In this case the desired solution is the one with the minus sign before the square root, which makes the intersection positive. In conclusion the solution closest to the conic apex is the one with the minus sign before the square root but it must be validated against the desired branch limits.

For a vertical flat target, passing through the origin (z=0), the intersection with a line crossing the z-axis at a distance l to the right describing an acute angle ϕ with the axis is given by

(3.30) $$y = l \tan \phi .$$

For a cylinder with base (b diameter) at the origin the intersection with the line (Figure 3.6) depends on whether ϕ is larger or smaller than the angle ϕ_C described at the intersection of the base with the cylinder body. This angle is defined by

(3.31) $$\phi_C = \arctan\left(\frac{b}{2l}\right).$$

If $\phi < \phi_C$ the intersection is at the base, which is a flat target, so equation (3.30) is used. If $\phi > \phi_C$ the intersection is at the cylinder body (y=b/2) and is given by

(3.32) $$z = l - \frac{b}{2 \tan \phi}.$$

A light ring containing the corner may be undesirable in a cylindrical target. The base diameter and the cylinder length can be modified in order to avoid this situation without changing the number of rings. The new dimensions need to be calculated for the cylinder end to be in the same line that marks the edge of the last ring (Figure 3.6). If the base diameter is increased to b_1 and the length to l_{cyl1} the

light ring will lay on the base. Alternatively the base diameter can be decreased to b_2 and the length to l_{cyl2}, the light ring will then stay on the cylinder body. Videokeratoscopes that use a cylindrical target always have more than two rings on the base. Increasing the base diameter is therefore the best option. However since the base is further away from the reflecting surface vertex than the cylinder body, the same angular ring magnitude results in larger rings at the base.

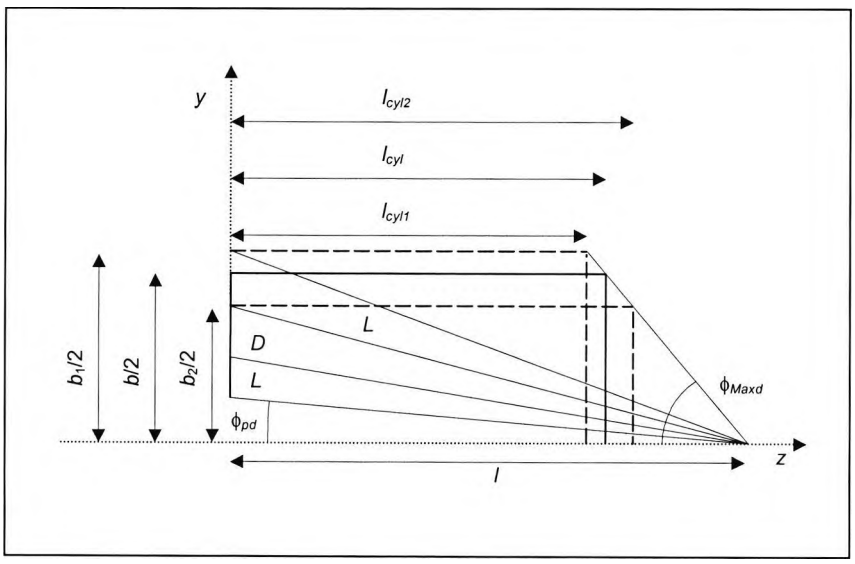

Figure 3.6 – Section of a cylinder with light (*L*) and dark (*D*) rings defined by the intersection of lines at equal angle intervals. If a light ring falls in the corner, the cylinder base can be increased or decreased (long dashed sections) to avoid this situation keeping the number of rings constant.

The distance $l=wd+z_{PD}$ (see Figure 3.3 for definition of parameters *wd* and z_{PD}) does not change if the reflecting surface is decentred laterally in the *xy* plane since it represents the *z* coordinate of the surface vertex.

3.2 *Reflecting surface*

The reflecting surface is intended to represent a simplified model of the human cornea and also a test surface. Research conducted in different ways by several authors has shown that the normal human cornea approaches a prolate ellipse in a single meridian. The average *p* value determined in each work is very variable but

always in the range $0<p<1$. It is also concluded that the cornea is not a rotational symmetric surface. Eghbali et al. (1995) presented a review of the p value averages found by several authors and in their research found an average of 0.82. Another average was taken including their p to the list resulting in 0.81 (0.05 SD). Kiely et al. (1982) presented a list of average central radius of curvature for the human cornea determined by several authors. Adding to this list the value found by Guillon et al. (1986) the average of all values considered was 7.75mm (0.13mm SD). For this research the normal human cornea was approached by a prolate ellipsoid with 7.75mm apical radius and a p value of 0.82 limited by a maximum diameter (*CD* in Figure 3.3) of 8mm. According to Waring(1989) the cornea flattens more in the limbal area and can no longer be represented by the same curve.

Although a prolate ellipsoid may be used as an approximate model for the normal cornea, an oblate ellipsoid can represent a cornea after refractive surgery (Eghbali et al. 1995) and a hyperbola with small radius of curvature is similar to the cone in keratoconus.

3.3 Axis systems

The global Cartesian system (abbreviated as *GLB*) was placed at the far left following the optical sign convention that the light rays should travel from left to right. The z-axis is horizontal, the y vertical and the x is perpendicular to the page pointing away from the reader. The corresponding unit vectors are $\hat{\imath}$, $\hat{\jmath}$, and $\hat{k}$. These directions form a right-handed system, which means that the vector product of any two of these unit vectors results in the third one. The faceplate vertex is at the origin of this system (Figure 3.1).

Several local coordinate systems were also defined to simplify calculations. When working with the reflecting surface it is easier to consider that the origin is at the same z-coordinate as the surface vertex. Such a system is a translation of the global system along the z-axis direction and will be abbreviated as *VTX*. If the reflecting surface is centred the *VTX* origin will coincide with the surface vertex.

When determining the position of image points on the image plane, based on the intersection of reflected rays with the pupil, it is easier to place the origin at the pupil centre. This local coordinate system will be abbreviated as *PUP*.

When looking at the ring mire image reflected on the analysed surface it is easier to define points in the image on the examiner's viewpoint (along the positive *z*-axis direction). For that purpose a new two dimensional axis system is used with the *x*-axis pointing in the opposite direction of the global system one. This system is abbreviated as *IMG*.

A polar coordinate system is useful for defining the radial locus of points in a rotational symmetric surface. If it is measured in the global system a point is located by the coordinates $(\rho,\varphi)_{GLB}$, if it's in the image system the coordinates are $(\rho,\sigma)_{IMG}$. The relations between both angles are represented in Figure 3.7.

To represent a tilted surface, Cartesian coordinates were selected due to the properties of conics being well documented in this form. Using spherical or cylindrical coordinates may be adequate for some purposes but its use in this research project would not allow a comprehensive analysis of all possible sources of error. To make this analysis possible a tilted coordinate system had to be developed in order for the tilted conoids to be represented by Baker's equation in that system. If a tilted conic was represented in the global system its equation would take the form

(3.33) $$Az^2 + 2Bzy + Cy^2 + Dz + Ey + F = 0$$

(Bers, 1969), which is difficult to analyse due to the mixed term *zy*.

Since Baker's equation was selected to represent the surface, the tilt was applied to the vertex. When using a reflecting surface in a real videokeratoscope there may not be a possibility to tilt around the vertex for mechanical reasons. In that case a

tilt applied to any other point on the surface will be equivalent to a tilt around the vertex plus a decentring, therefore any case can be represented in the simulation program.

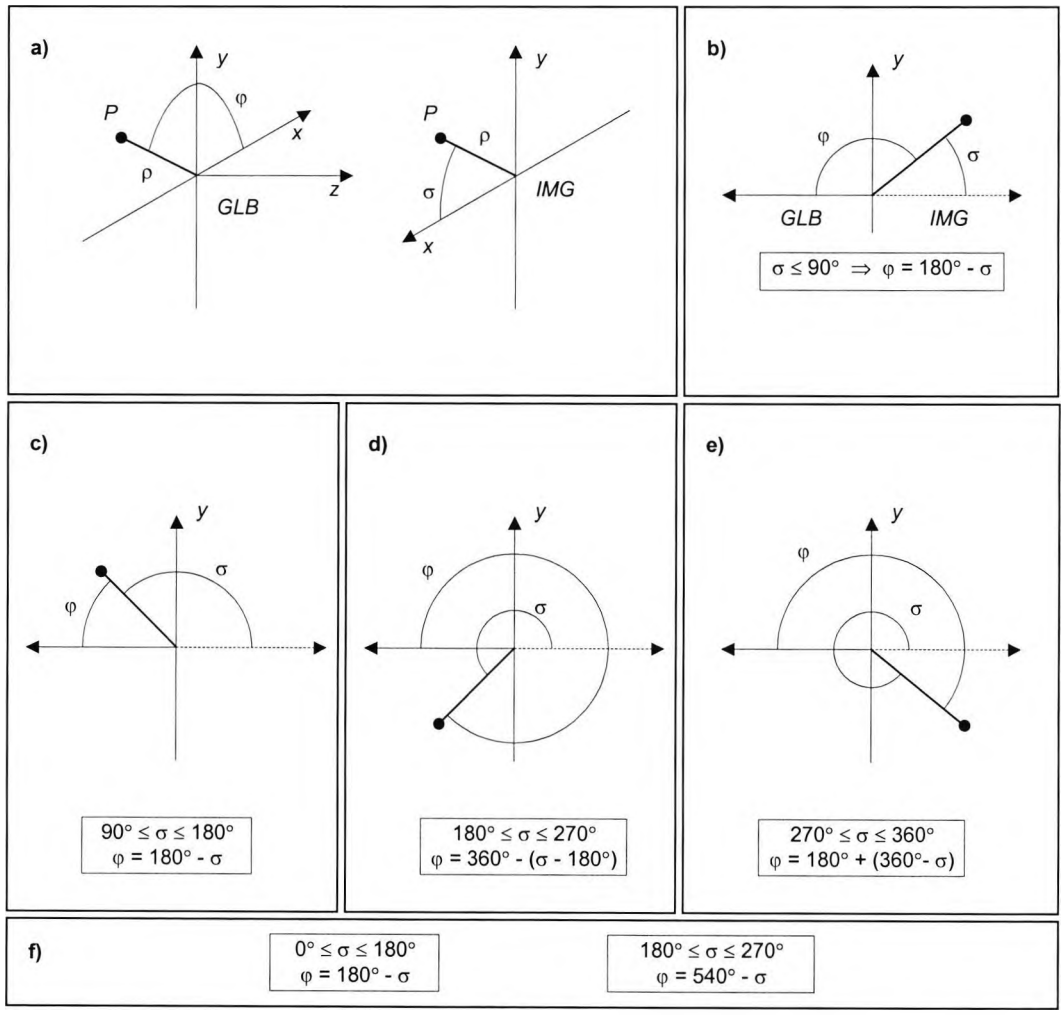

Figure 3.7 - Definition of a point P in polar coordinates for the global (ρ,φ) and the image system (ρ,σ) and their relations.

Tilting a centred surface by the vertex was achieved in two steps. First, when observing the reflecting surface from the examiner's view point, a semi-meridian is selected on the *xy* plane. It is important to notice that this selection is not a rotation applied to the surface. Then the z-axis of the surface is pulled towards the selected

semi-meridian in the plane defined by that semi-meridian and the original *z*-axis. This plane will be referred as the tilt plane. The semi-meridian is chosen by specifying angle σ, from the observer's point of view of the surface (Figure 3.7). This angle is then transformed to φ applying the relations presented in the previous figure. The angular magnitude of the tilt in the tilt plane is specified by angle θ subtended by the original *z*-axis of the centred surface and the rotated z-axis of the tilted surface $\hat{e}_r$. This rotation is represented in Figure 3.8 b).

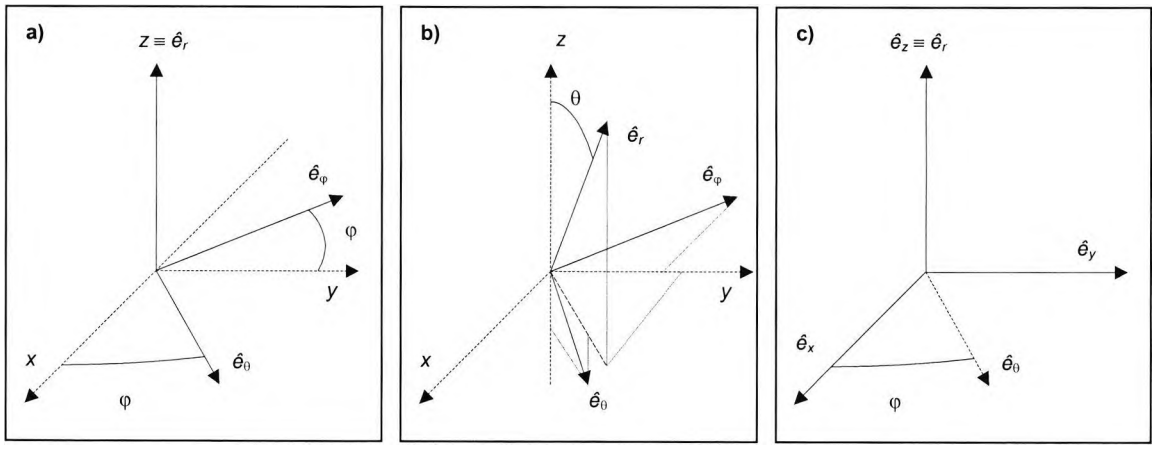

Figure 3.8 – a) The axis system was rotated in the *xy* plane to define the tilt plane. The reflecting surface vertex was centred at the origin of *xyz* but wasn't rotated along with the axis. **b)** A new axis rotation was executed in the plane defined by $\hat{e}_r$ and $\hat{e}_\theta$. The unit vector $\hat{e}_\varphi$ remained on the *xy* plane. The surface was then rotated by θ and $\hat{e}_r$ is the rotated surface z-axis. **c)** This is the axis system developed for this research where $\hat{e}_\theta$ is represented just for reference. The unit vectors $\hat{e}_r$ and $\hat{e}_\theta$ have the same orientation as the middle figure but were represented oriented like *xyz* to allow a better understanding of their relations. The vectors $\hat{e}_x$ and $\hat{e}_y$ define a plane which is perpendicular to the plane defined by $\hat{e}_\theta$ and $\hat{e}_r$.

The first model developed for the tilted system is represented in Figure 3.8 a) and b). The first step was to define the tilt plane by the vectors $\hat{e}_r$ and $\hat{e}_\theta$ by a rotation of φ from the *x* axis (Figure a). Then these two vectors were rotated by an angle θ around $\hat{e}_\varphi$ (Figure b). This approach is sufficient for a rotational symmetric surface

since after a tilt in any semi-meridian the surface equation has the same form in the new axis system. However procedures developed in this research are meant to be a skeleton for future investigation work using surfaces without rotational symmetry. For a better explanation, consider a centred ellipse on the *xy* plane with its minor axis in the *x* direction (Figure 3.9 a), hence represented by equation(3.2) but with *x* replacing *z* in the equation. If a tilt is applied in the plane defined by $\hat{e}_r$ and $\hat{e}_\theta$, the ellipse principal axis won't coincide with these directions (Figure 3.9 a). Therefore the curve equation won't take the usual form and will be of the type presented in equation(3.33) but with *z* and *y* replaced by other variables. Since the aim of developing a tilted axis system was to avoid this equation, a different system had to be developed. It should be noted that if instead of an ellipse a circle had been used than this axis system wouldn't be a problem due to symmetry.

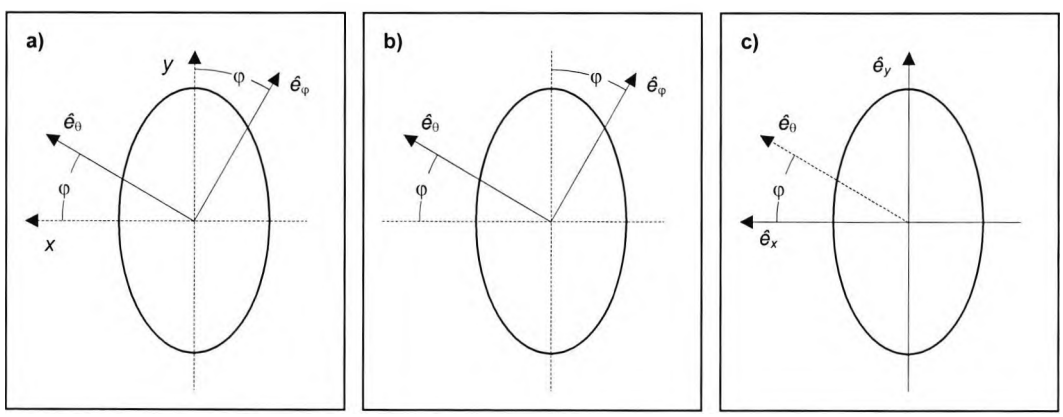

Figure 3.9 - Example of the application of the tilt system of axis to a centred ellipse with minor axis along the x-axis. **a)** The tilted plane is selected by a φ rotation of the axis in the *xy* plane. Once again it must be emphasised that the ellipse is not rotated with $\hat{e}_\theta$ and $\hat{e}_\varphi$. **b)** The ellipse was tilted in the tilt plane (perpendicular to the screen defined by $\hat{e}_r$ and $\hat{e}_\theta$) therefore is not in the *xy* plane anymore. However $\hat{e}_\theta$ and $\hat{e}_\varphi$ are still separated by angle φ from the ellipse principal axis. **c)** The final system is represented for which the unit vectors coincide with the ellipse principal axis. The unit vector $\hat{e}_\theta$ is just represented to show the intersection with the tilt plane.

A solution could be to execute two rotations; the first would place the major axis coincident with $\hat{e}_\theta$ and then execute the tilt. This would make the principal axes

coincident with the system axis but the tilt plane would have to contain the major axis limiting the possibilities and the tilt would be the combination of two rotations. Therefore a different model was required to solve these problems. If a rotation of magnitude θ is executed in the plane defined by $\hat{e}_r$ and $\hat{e}_\theta$, the perpendicular plane that contains $\hat{e}_\theta$ is the *xy* plane rotated by the same amount. Knowing that an angle φ separated $\hat{e}_\theta$ from the *x*-axis, if the same rotation is applied in the new plane a new axis ($\hat{e}_x$) can be defined, which corresponds to the *x*-axis in this plane. The axis $\hat{e}_y$, corresponding to the *y*-axis in the new plane, is obtained by a 90°-φ rotation in the opposite direction from $\hat{e}_\theta$ (Figure 3.8 c) and Figure 3.9 c). This procedure allows the equation of a surface without rotational symmetry tilted in any semi-meridian φ to take the same form in the global and the tilted system. The price to pay is an unnecessary increase in complexity when using a rotational symmetric surface.

When the tilted system is applied to the global system it is abbreviated as *GLBTLT*. When applied to the *VTX* system is abbreviated *VTXTLT*.

Determining the relations between the unit vectors in the global and tilted systems is not straightforward. Only $\hat{e}_z$ and the reference vector $\hat{e}_\theta$ are a direct result of a rotation from one of the global system axes and the relations are easy to determine. They are respectively:

(3.34) $$\hat{e}_z = \sin\theta\cos\varphi\,\hat{i} + \sin\theta\sin\varphi\,\hat{j} + \cos\theta\,\hat{k}$$

and

(3.35) $$\hat{e}_\theta = \cos\theta\cos\varphi\,\hat{i} + \cos\theta\sin\varphi\,\hat{j} - \sin\theta\,\hat{k}\,.$$

It should be noted that it is essential to work only with acute angles when determining relations between unit vectors in two axis systems.

To determine the relations for $\hat{e}_x$ and $\hat{e}_y$ a system of 3 equations was used to determine the direction cosines *u*, *v* and *w* for each unit vector. The desired vectors are in a plane perpendicular to $\hat{e}_z$ so the scalar product between this and any of the other vectors is zero. The unit vector $\hat{e}_x$ describes an angle φ with $\hat{e}_\theta$ so their scalar product is $\cos\varphi$. The unit vector $\hat{e}_y$ describes an angle $90°-\varphi$ with $\hat{e}_\theta$ so their scalar product is $\cos(90°-\varphi)=\sin\varphi$. A unit vector has unit length thus the sum of the squares of their components is one. The two systems of three equations can be summarised in the form

$$\begin{cases} \hat{e}_x \bullet \hat{e}_z = 0 \quad or \quad \hat{e}_y \bullet \hat{e}_z = 0 \\ \hat{e}_x \bullet \hat{e}_\theta = \cos\varphi \quad or \quad \hat{e}_y \bullet \hat{e}_\theta = \sin\varphi \\ u^2 + v^2 + w^2 = 1 \end{cases} . \tag{3.36}$$

The quadratic nature of the last equation in the system introduces a double solution. The correct solution is selected when tested against the condition $\theta=0$, in which case $\hat{e}_x \equiv \hat{i}$ and $\hat{e}_y \equiv \hat{j}$. The relations between vectors in both axis systems are represented in matrix form by

$$\begin{bmatrix} X\hat{e}_x \\ Y\hat{e}_y \\ Z\hat{e}_z \end{bmatrix} = \begin{bmatrix} 1-\cos^2\varphi(1-\cos\theta) & \sin\varphi\cos\varphi(\cos\theta-1) & -\sin\theta\cos\varphi \\ \sin\varphi\cos\varphi(\cos\theta-1) & \sin^2\varphi\cos\theta+\cos^2\varphi & -\sin\theta\sin\varphi \\ \sin\theta\cos\varphi & \sin\theta\sin\varphi & \cos\theta \end{bmatrix} \begin{bmatrix} x\hat{i} \\ y\hat{j} \\ z\hat{k} \end{bmatrix} \tag{3.37}$$

and

$$\begin{bmatrix} x\hat{i} \\ y\hat{j} \\ z\hat{k} \end{bmatrix} = \begin{bmatrix} 1-\cos^2\varphi(1-\cos\theta) & \sin\varphi\cos\varphi(\cos\theta-1) & \sin\theta\cos\varphi \\ \sin\varphi\cos\varphi(\cos\theta-1) & \sin^2\varphi\cos\theta+\cos^2\varphi & \sin\theta\sin\varphi \\ -\sin\theta\cos\varphi & -\sin\theta\sin\varphi & \cos\theta \end{bmatrix} \begin{bmatrix} X\hat{e}_x \\ Y\hat{e}_y \\ Z\hat{e}_z \end{bmatrix} . \tag{3.38}$$

3.4 Decentring the reflecting surface

The decentration is defined in polar coordinates from the examiner's view in relation to the image system *IMG*. It is specified by the magnitude ρ in mm from the global system *z*-axis and the semi-meridian σ in which the decentration should take

place (Figure 3.7). It represents the new position of the conoid vertex in the image system $x_V=\rho\cos\sigma$ and $y_V=\rho\sin\sigma$. However these parameters must be transformed into global system coordinates using the relations between both systems expressed in Figure 3.7. The decentration is then given by $x_V=\rho\cos\varphi$ and $y_V=\rho\sin\varphi$.

Decentring the surface has to be limited in such a way as to avoid the surface falling outside the faceplate limits. To prevent this situation it was postulated that the faceplate maximum diameter (*MAXD*) must be at least 2mm larger than the surface maximum diameter (CD). This condition will allow a margin of 1mm on either side of *CD*. In a real videokeratoscope the reflecting surface could fall outside the faceplate limits but that part of the surface won't reflect rays into the instrument pupil.

If the decentration is larger than 1mm then the problem may arise again. Both faceplate and reflecting surfaces have rotational symmetry around the *z*-axis, so an analysis can be done for just one semi-meridian. Taking the initial margin of 1mm from the faceplate limit the decentration *d* (positive) must fulfil the condition

(3.39) $$d \leq \frac{MAXD}{2} - \frac{CD}{2} - 1.$$

3.5 Tilt limits

The tilted surface cannot touch the faceplate, since that situation is impossible in a real videokeratoscope. If this situation is not prevented the simulation would provide unreliable results. Although the tilting angles are typically small this would still be possible for a small faceplate.

To determine the points of intersection of the faceplate with a tilted surface both surfaces must be specified in the same axis system. This approach leads to large equations and so an alternative procedure was developed to get around this

problem. The exact intersection points are not of any interest, it is only necessary to know if the tilted reflecting surface can intersect the faceplate and what to do to prevent this situation from happening. To reduce the problem to a plane the worst case scenario was adopted which is tilt and decentration applied in the same semi-meridian. Once again the 90° semi-meridian was selected for the demonstration. If the surface is rotated 360 degrees around its vertex in the vertical plane *yz*, a circle is described by the surface limits. If the faceplate doesn't touch this circle there is no possibility of the tilted surface intersecting it (Figure 3.10). The great advantage of this approach is that the circle has a simple equation and is expressed in the global system, so finding its intersection with the faceplate is much easier than the initial problem. The disadvantage is that if the tilt is small it is possible that no intersection exists even though the circle touches the faceplate.

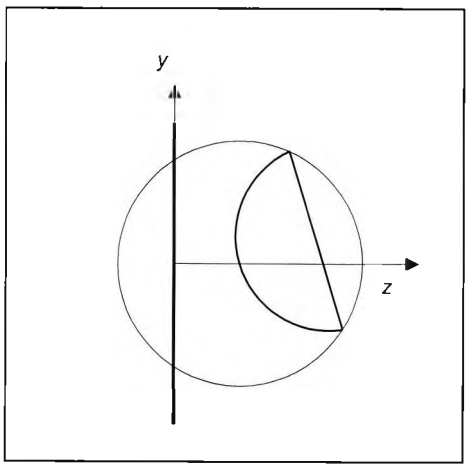

Figure 3.10 - Example of a case in which a tilted reflecting surface doesn't touch the faceplate but the circle described by the surface limits around the vertex does. The program will only allow the flat target to be placed outside the circle limits.

The radius R_{CD} of the circle centred at the vertex is

$$R_{CD} = \sqrt{\left(\frac{CD}{2}\right)^2 + z_{CD}^2} \tag{3.40}$$

(Figure 3.11 a). The variable z_{CD} is the distance from the vertex to the maximum diameter of the reflecting surface if not tilted, given by equation(3.12) with y=0.5CD and x=x_V=y_V=0. Each faceplate type will be analysed at a time. The tilt must be combined with the decentration in order to establish the limits of both parameters.

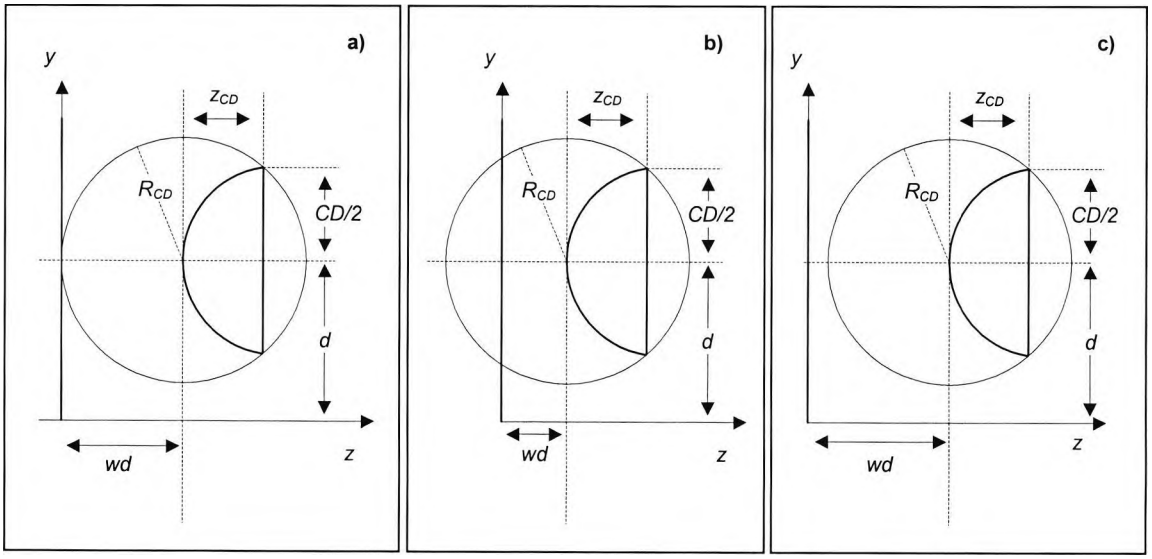

Figure 3.11 - Possibility for a tilted and decentred surface to intersect a flat faceplate. The images represent the circle centred at the vertex passing through the surface limits just touching (**a**), intersecting (**b**) and failing to intersect (**c**) the faceplate (thick line). Only the top half of the faceplate section is represented and the decentration, bigger than R_{CD}, was enough to take the circle above the z-axis.

For the flat faceplate (Figure 3.11) it is very easy to see that the circle centred at the vertex passing through the faceplate limits fails to intersect the faceplate if $wd>R_{CD}$ (Figure c). A cylinder has two components: the base and the cylinder body. The base is equivalent to a flat target so it must fulfil the same conditions.

For the cylinder body it can be seen by analysing Figure 3.12 c) that the circle fails to intersect the faceplate if $d+R_{CD}$ <0.5$MAXD$ which solved for d yields d<0.5$MAXD$-R_{CD}. In this case the tilting and decentration limits are not

independent. This last condition can also be applied to the flat faceplate to prevent the tilted surface from falling outside *MAXD*.

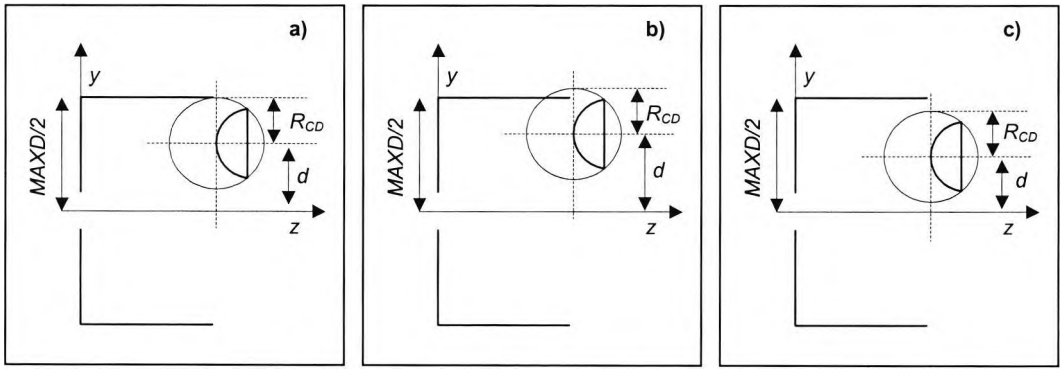

Figure 3.12 - Possibility for a tilted and decentred surface to intersect a cylindrical faceplate. Only the top part of the cylinder was considered.

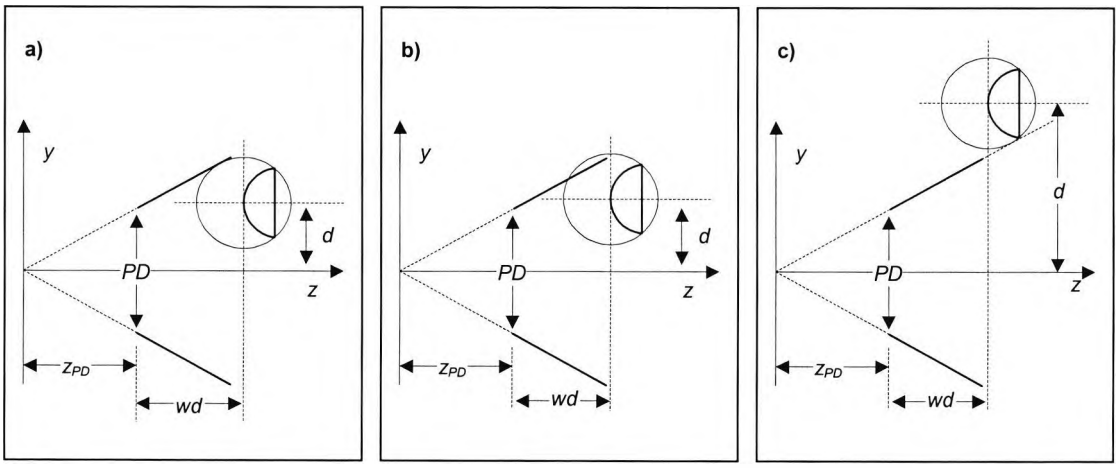

Figure 3.13 – Possibility for a tilted and decentred surface to intersect a cone shaped faceplate with *PD* diameter pupil located at a z_{PD} distance from the origin. Only the top part of the cone section was considered (thick line) for each situation. It can be seen that there is no intersection if the circle centred at the vertex passing through the surface limits is bellow (**a**) or above (**c**) the faceplate. This last case was obviously disregarded since the surface cannot be outside the faceplate limits.

For a cone shaped faceplate (Figure 3.13) the intersection problem gets slightly more complex. Once again a section that passes through the middle of the cone is

taken and only the top part analysed. This part is a straight line that passes through the origin so the equation has the form $y=mx$. The gradient m is $\sqrt{-p}$ as indicated previously.

The circle centred at the vertex and passing through the reflecting surface limits is represented by

(3.41) $$(y-d)^2+(z-wd-z_{PD})^2=R_{CD}^2 .$$

If the straight line representing the top part of the target is replaced in this expression the resultant equation is

(3.42) $$(1+m^2)z^2-2z(md+wd+z_{PD})+\left[d^2+(wd+z_{PD})^2-R_{CD}^2\right]=0 .$$

The solution for a quadratic equation of the type $az^2+bz+c=0$ is given by a well known formula. This formula has the term b^2-4ac inside a square root, therefore if it's negative the solution has imaginary roots which means the circle does not intersect the faceplate. This term, for equation (3.42), can be simplified into

(3.43) $$b^2-4ac=\left\{R_{CD}\sqrt{1+m^2}-\left[m(wd+z_{PD})-d\right]\right\}\left\{R_{CD}\sqrt{1+m^2}+\left[m(wd+z_{PD})-d\right]\right\} .$$

This is really another quadratic equation with d as variable. In this form it can easily be seen that this function has two roots at $d=m(wd+z_{PD})-R_{CD}\sqrt{(1+m^2)}$ and $d=m(wd+z_{PD})+R_{CD}\sqrt{(1+m^2)}$, these are the values of d for which the circle is tangent to the faceplate (Figure 3.13 a) and c) respectively). The condition $b^2-4ac<0$ must be met as stated previously. Analysis of equation(3.43) shows that the coefficient of d^2 is negative which means this function is negative outside the roots. Therefore the solution for the stated condition is $d<m(wd+z_{PD})-R_{CD}\sqrt{(1+m^2)}$ or $d>m(wd+z_{PD})+R_{CD}\sqrt{(1+m^2)}$. The latter is a solution for which the circle falls outside

the faceplate limits, hence invalid. Concluding this analysis, the tilted and decentred surface does not intersect the faceplate if the decentration is limited by the condition $d<\sqrt{(-p)}(wd+z_{PD})-R_{CD}\sqrt{(1-p)}$.

The intersection between the circle centred at the vertex (equation(3.41)) and a conic (equation(3.1)) becomes a very complex problem, since there can be four intersection points (Figure 3.14). This is expressed by the fourth degree equation

(3.44)

$$(1-p_T)^2 z^4 - 4z^2(1-p_T)(wd+z_{PD}-R_T)+2z^2\{(1-p_T)[d^2+(wd+zpd)^2-R_{CD}^2]+2[(wd+z_{PD}-R_T)^2+d^2 p_T]\}-$$
$$-4z\{(wd+z_{PD}-R_T)[d^2+(wd+z_{PD})^2-R_{CD}^2]+2d^2R_T\}+[d^2+(wd+z_{PD})^2-R_{CD}^2]^2=0$$

representing the problem.

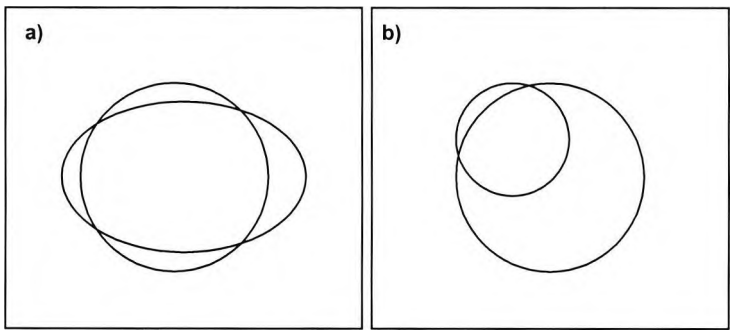

Figure 3.14 - Intersection between a circle and an ellipse (**a**), a maximum of four points can be found. Intersection between two circles (**b**) a maximum of two points can be found. The only exception is if the circles have the same radius and overlap.

The case of intersection with another circle (p=1) is simpler because there are only two intersection points and equation(3.44) becomes of second degree. However there are still several possibilities depending on the relations between the faceplate radius R_T and R_{CD}.

A solution for the equation could not be found due to its extension and relative complexity of the *z* coefficients. Numerical methods were applied to search for the equation roots but because the *z* coefficients were large numbers there was a significant loss of accuracy in the process. This was tested with a circle intersecting an ellipse close to the end opposite the vertex. There should be two intersection points but the numerical routine only returned imaginary roots meaning no intersection was found.

A new procedure had to be developed without resorting to the long fourth degree equation. If a point in the faceplate falls inside the circle centred at the reflecting surface vertex then *y* for the former, given by

(3.45) $$y = \sqrt{2R_T z - p_T z^2}$$

is smaller or equal to *y* for the latter, given by

(3.46) $$y = \sqrt{R_{CD}^2 - [z - (wd + z_{PD})]^2} + d\,,$$

as represented in Figure 3.15. These equations are obtained by solving equations(3.1) and (3.41), respectively, in order to *y*. If this process is repeated from the vertex of the circle centred at the vertex ($z=z_{PD}+wd-R_{CD}$) to the faceplate limits ($z=z_{MAXD}$) in small steps, it can be determined if the faceplate falls inside the circle. For the research 1μm intervals were used for which modern computers can complete the analysis in seconds, depending on the z interval length analysed.

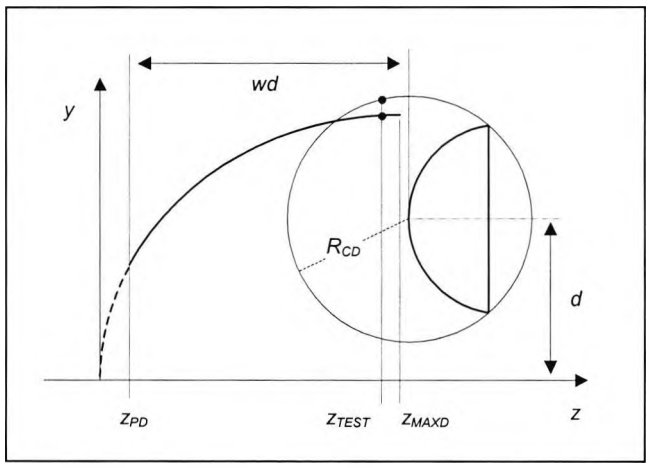

Figure 3.15 – Possibility for a tilted and decentred surface to intersect a conoid shaped faceplate. Only the top half of the faceplate section was represented (thick line). If there is an intersection for a given value of z (z_{TEST}) the corresponding y value for the faceplate is smaller or equal to y on the circle centred at the vertex of the reflecting surface.

3.6 Ray tracing equations for reflection

The general ray tracing equations derived by Welford (1986) were modified in order to accommodate the decentred surface case. Usually the ray tracing process can be divided in the following phases:

- Selection of the object point and the direction of a ray.
- Transfer to the plane perpendicular to the reflecting surface axis touching the surface vertex.
- Transfer to the surface.
- Reflection.
- Transfer to the pupil plane.

The developed model assumes that the camera is able to capture all rays striking the camera objective. If this assumption wasn't made it would imply linking a particular camera optics to the simulation. This would make it valid for only a single camera design, when is intended to be general.

The object point has coordinates (x_T, y_T, z_T) in the global system and the direction of a ray coming from it is represented by a unit vector with direction cosines (L,M,N). The intersection of this ray with the plane perpendicular to the reflecting surface axis touching the surface vertex is (x_o,y_o,0) given by

(3.47) $$x_o = x_T + \frac{L}{N}(l - z_T)$$

and

(3.48) $$y_o = y_T + \frac{M}{N}(l - z_T).$$

Using the *VTX* system simplifies the calculations. The parameter l is the distance from the global system origin to the reflecting surface vertex measured along the z axis. For a non-tilted surface $l=wd+z_{PD}$ (Figure 3.3).

This ray intersects the surface at the point ($x_o+L\Delta$, $y_o+M\Delta$, $N\Delta$) in the *VTX* system. The parameter Δ is the distance from the plane to the reflecting surface measured along the incident ray and is given by

(3.49) $$\Delta = \frac{F}{G + \sqrt{G^2 - [1 + (p-1)N^2]cF}}.$$

The parameter c is the apical curvature of the reflecting surface and F and G are respectively

(3.50) $$F = c[(x_o - x_v)^2 + (y_o - y_v)^2]$$

and

(3.51) $$G = N - c[L(x_o - x_v) + M(y_o - y_v)].$$

The reflection equations presented by Welford were derived for a spherical reflecting surface. Using the same procedure the expressions for conoids were calculated and are respectively

(3.52) $$L' = -L - \frac{2c(x - x_v)\cos I}{\sqrt{1 - 2c(p-1)z + c^2 p(p-1)z^2}},$$

(3.53) $$M' = -M - \frac{2c(y - y_v)\cos I}{\sqrt{1 - 2c(p-1)z + c^2 p(p-1)z^2}},$$

and

(3.54) $$N' = -N + \frac{2\cos I - 2cpz\cos I}{\sqrt{1 - 2c(p-1)z + c^2 p(p-1)z^2}},$$

where

(3.55) $$\cos I = \frac{N - c(Lx + My + Npz)}{\sqrt{1 - 2c(p-1)z + c^2 p(p-1)z^2}}.$$

The direction of the reflected ray is represented by the direction cosines [-*L'*,-*M'*,-*N'*]. *I* is the angle of incidence equal to the angle of reflection.

The intersection of the reflected ray with the pupil plane is given by equations (3.47) and (3.48) using *L'*,*M'*,*N'* instead of *L*,*M*,*N* and *l*=-*wd*. The direction [*L'*,*M'*,*N'*] is opposite to the reflected ray as stated previously. This ray starts at the surface to the right of the pupil plane therefore for it to strike the plane it's necessary to be directed from right to left which corresponds to $N'>0$. If $N'\leq 0$ the reflected ray will not intersect the pupil plane.

3.6.1 The parameter Δ

A line can intersect a conoid in two points therefore it's necessary to select the correct one. This problem was previously addressed in section 3.1.3 but now needs to be solved using parameters from the ray tracing equations in order to simplify the procedure. The conoid represents a reflecting surface therefore the

closest intersection to the object point should be selected. The intersection further away from the object point would correspond to a transmitted ray. It is important to note that this principle is only valid for the part of the surface that contains the vertex, corresponding to z=0 in Baker's equation. If for example a hyperbola is used the closest intersection to the object point may be located in the left branch, however this branch does not contain the vertex hence the principle is not valid. For this case the correct intersection would be the one further away from the object point. The equation for Δ has two solutions, equation(3.49) represents the correct one and will be called Δ^+. The second solution for Δ has a negative sign before the square root and will be called Δ^-. The solution Δ^+ is correct if G>0 as pointed out by Welford. Freeman (1990) also addresses the problem of the correct intersection for conoids but also considers G>0. However analysis of equation (3.51) shows that G can be negative. This observation led to a detailed study of G for all conoids with light rays coming from left to right and right to left. For simplification centred surfaces were used with light rays in the yz plane, in which case $G=N-cMy_o$ and $F=cy_o^2$. Due to the number of cases involved, the G analysis for an ellipse using rays with M>0 and N>0 is going to be the only situation presented. For all other cases only the pertinent aspects will be discussed.

The first step to determine the sign of G is to find out which range of values of y_o makes the incident ray intersect the surface. From equation (3.49) a ray will intersect the surface if the expression inside the square root is positive or zero. Applying the analysis conditions (incident ray in the yz plane with M>0 and N>0 and surface with p>0) this expression can be transformed to give the condition

(3.56) $$pNc^2y_o^2 + 2cMy_o - N \leq 0 .$$

This condition shows that for an incident ray in the yz plane with direction [0, M, N], the intersection with the surface will be determined by y_0, which is the intersection of the ray with the vertex plane (plane perpendicular to the z axis passing through the surface vertex). This is illustrated in Figure 3.16 for a set of parallel rays

intersecting the vertex plane at different points. Equation (3.56) is quadratic in y_o and therefore has two roots represented by

$$y_o = \frac{-\sqrt{1-N^2} \pm \sqrt{1+(p-1)N^2}}{pNc}, \tag{3.57}$$

where the positive root (because $p>0$) was labelled y_{o1} and the negative y_{o2}. In the present analysis conditions $M=\sqrt{(1-N^2)}$. This expression was substituted into equation(3.57) making it easier to determine the sign of each root. If $y_o=y_{o1}$ or $y_o=y_{o2}$ the solutions Δ^+ and Δ^- are equal leading to a single solution for $\Delta=F/G$. This means that y_{o1} and y_{o2} are the intersections of the surface tangents (with direction $[0,M,N]$) with the vertex plane (rays 2 and 4 in Figure 3.16a).

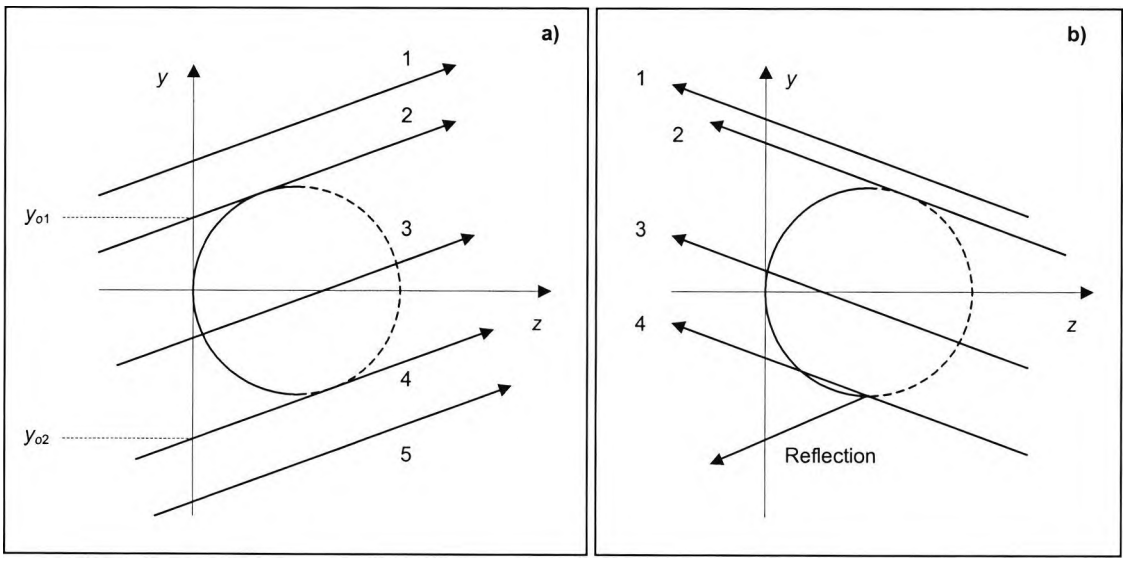

Figure 3.16 - Intersections of parallel light rays with a sphere in the *yz* plane. The dashed part of the circle is not part of the reflecting surface. **a)** Light rays travel from left to right, the object point is to the left of the surface. **b)** The opposite situation is pictured, the object is to the right of the surface vertex. This is possible when the surface is tilted (see text). In this case only rays that intersect the circle in two points on the useful part of the surface (ray 4) will be considered. In this context ray 3 is invalid since the only intersection on the useful part of the surface is on the back.

The coefficient of y_o^2 in equation(3.56) is positive therefore the equation is positive outside the interval between the roots y_{o1} and y_{o2} and negative within the interval. This means that a ray with direction [0,*M*,*N*] intersects the surface if it crosses the vertex plane between y_{o1} and y_{o2} (ray 3 in Figure 3.16 a). If $y_o>y_{o1}$ (ray 1) or $y_o<y_{o2}$ (ray 5) the ray will not intersect the surface.

Returning to the analysis of the sign of *G*, its value for $y_o=y_{o1}$ is

$$G = N - cMy_{o1} = \frac{\sqrt{1+(p-1)N^2}\left(\sqrt{1+(p-1)N^2}-\sqrt{1-N^2}\right)}{pN}, \tag{3.58}$$

which is positive for the analysis conditions (incident ray in the *yz* plane with $M>0$ and $N>0$ and surface with $p>0$). If $G=N-cMy_o$ is positive for y_{o1} then it is also positive for $y_o<y_{o1}$. *G* can only be negative when $y_o>y_{o1}$ although it can still be positive for some values in this interval. However the ray won't intersect the surface in this case therefore for the analysis conditions *G* is always positive if the ray intersects the surface. If $G>0$, the value for Δ in equation (3.49) (Δ^+) is the correct one since it will be the intersection closest to the object point and Δ^- will be further away. If none of the intersections are on the part of the surface that contains the vertex they are both considered invalid. Ray 4 in Figure 3.16 a) is an example of an invalid intersection since it hits the surface on the part that doesn't contain the vertex.

If the object point is located behind the vertex of the reflecting surface the light may travel from right to left to hit the surface. Although this seems odd it can happen if the reflecting surface is tilted (see Figure 3.18). The ray tracing procedures first transfer the ray to the vertex plane and then to the reflecting surface. However in this case the ray strikes the surface first and then passes through the plane (Figure 3.16 b). As a result Δ will be negative since the transfer from the plane to the surface is made in the opposite direction of the incident ray. Using algebra the *z*

coordinate of the transference from the plane to the surface is $z=N\Delta$. If $N<0$ and the surface is to the right of the plane ($z>0$) then Δ has to be negative.

Using the same process that was applied for the case $N>0$ and $M>0$ it was concluded that when a ray with $M>0$ and $N<0$ strikes the reflecting surface, G is negative. In this case $|\Delta^+|>|\Delta^-|$ which means that the Δ^+ intersection is further away from the vertex plane than Δ^-. Analysis of Figure 3.16 b) shows that in this case a ray can only be reflected if both intersections are on the useful side of the surface (ray 4). It is obvious that for this ray the correct intersection will be the one closest to the object point, which is also the one further away from the vertex plane. The Δ^+ solution is therefore the correct one for this case. It can be seen that ray 3 is not considered since the first intersection is on the side of the surface that isn't used and the second intersection hits the surface from the inside and hence can't be reflected.

For a parabola ($p=0$) the case of a ray parallel to the z-axis needs special considerations. It is easy to see that for this case the ray intersects the surface in a single point. The Δ parameter is the solution of equation

(3.59) $$\left[1+(p-1)N^2\right]c\Delta^2-2G\Delta+F=0\,.$$

When $N=1$ in a parabola the coefficient $1+(p-1)N^2=0$ and the last equation becomes of first degree, implying a single solution $\Delta=F/(2G)$.

For a hyperbola there are two special cases: rays parallel to and coincident with the asymptote. Analysis of Figure 3.5 shows that for the first case there is a single intersection and in the second case no intersection. The analysis for the first case is very similar to the parabola special case since the coefficient $1+(p-1)N^2=0$ and $\Delta=F/(2G)$ however N is not 1. If $N<0$ the ray strikes the surface from the inside so it isn't reflected. For a ray coincident with the asymptote the coefficient $1+(p-1)N^2=0$

and G=0 so Δ is undetermined from equation (3.59). Alternatively if $\Delta=F/(2G)$ is used as a solution then $\Delta=\infty$ which is the point of contact of the asymptote with the hyperbola.

In conclusion, the transfer from the vertex plane to the surface has to be approached with great care to check if the intersection point is valid. The z value of the intersection must be checked to determine if it's in the specified surface limits. If the ray strikes the surface from inside the ray tracing procedure must be aborted because the ray won't be reflected.

3.6.2 Special case: Initial ray perpendicular to the surface z axis (N=0)

For this case the general ray tracing equations are not valid so adequate modifications had to be made. The transfer to the plane perpendicular to the reflecting surface couldn't be achieved since the ray is parallel to the plane. As a result Baker's equation, representing the reflective surface, had to be expressed in relation to the global system. This resulted in a decentration $z_v=wd+z_{PD}$ in z resulting in

(3.60) $$(x-x_v)^2+(y-y_v)^2=2R(z-z_v)-p(z-z_v)^2 .$$

The initial condition for the ray to strike the surface is $z_v<z_T\leq z_v+z_{CD}$. The intersection point z coordinate is the same as the object z_T since the ray is perpendicular to the surface axis. The intersection of the ray with the reflecting surface is calculated by substitution of the ray vector equation

(3.61) $$(x,y,z)=(x_T,y_T,z_T)+\Delta(L,M,0)$$

in equation(3.60). This substitution results in

(3.62) $$c\Delta^2 - 2G\Delta + F = 0$$

where

(3.63) $$G = c[L(x_v - x_T) + M(y_v - y_T)]$$

and

(3.64) $$F = c\left[(x_T - x_v)^2 + (y_T - y_v)^2 + p(z_T - z_v)^2\right] - 2(z_T - z_v).$$

The values of $c\Delta$ that satisfy equation(3.62) are

(3.65) $$c\Delta = G \pm \sqrt{G^2 - cF}$$

Once again the solution with a + sign before the square root will be referred to as Δ^+ and the other by Δ^-. The ray will intersect the surface if the expression inside the square root fulfils the condition G^2-$cF \geq 0$. This expression can be developed into

(3.66) $$G^2 - cF = -c^2[-M(x_v - x_T) + L(y_v - y_T)]^2 + c(z_T - z_v)[2 - pc(z_T - z_v)].$$

The first term of this equation is never positive so it contributes to an intersection failure. The expression inside brackets is the vector product of the incident ray direction [L,M,0] by the vector joining the object point to the axis [x_V-x_T,y_V-y_T,0] (Figure 3.17 a), object point 1). The vector product of two vectors is zero when they have the same direction. This means that regardless of the distance of the object point to the surface if it points towards the surface axis and z_T is inside the surface limits, the ray will always strike the surface.

The second term of equation(3.66) is dependent on the surface limits along the z axis. It can be seen in Figure 3.17 that a ray with N=0 striking the surface outside the z limits will always fail the surface (object points P_2 and P_3). If the object point is

located before the surface vertex ($z_T<z_V$) the ray will fail for a circle, ellipse and parabola ($p\geq0$) because the second term will be negative. For a circle and ellipse the ray will also fail if $z_T>z_V+2/(cp)$, which corresponds to a ray beyond the other surface limit. For a hyperbola ($p<0$) the ray will only fail if it falls in the gap between the branches, which corresponds to the condition $z_V+2/(cp)<z_T<z_V$.

If the incident ray points towards the surface in direction $[L_1,M_1]$ the scalar product is positive so $G>0$. Therefore the solution Δ^- in equation (3.65) is the correct one, which corresponds to the intersection closest to the object point.

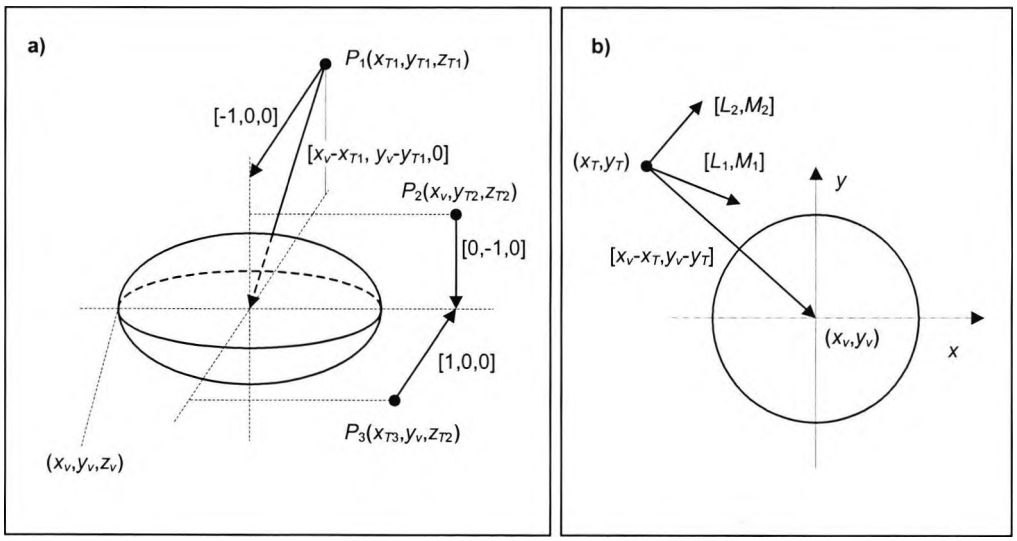

Figure 3.17 – Special ray tracing case with incident ray perpendicular to the surface z axis (N=0). **a)** Ray intersection failures due to ray direction in xy plane (P_1) and displacement along the z axis (P_2 and P_3). The values in parenthesis are the object point coordinates and the line matrices are ray directions. **b)** Section of the ellipse in the xy plane with an object point sending light rays in several directions. The scalar product of the direction of a particular ray with the vector $[x_V-x_T,y_V-y_T]$ is an indicator of the possibility of intersection with the surface in the incident ray direction.

The intersection point following correct determination is translated to the *VTX* system using $z=z-(wd+z_{PD})$. The reflection equations (3.52) to (3.55) can then be applied and the ray tracing follows the regular procedure.

3.6.3 Ray tracing with a tilted reflecting surface

It is very complex to modify the ray tracing equations for a reflective tilted surface so an alternative procedure was developed. In the first phase of the ray tracing process the object point and the directions were transformed into a tilted axis system with its origin at the global system origin using equation (3.37). This system is referred to as the *GLBTLT* axis system. Using the same equation the position of the reflecting surface vertex (x_v,y_v,z_v) was also translated to *GLBTLT* becoming (X_v,Y_v,Z_v). This axis system was developed in order for Baker's equation to have the same form therefore the transfer equations will be the same. This procedure results in a tilt inversion consisting of a straight reflecting surface with a tilted target (Figure 3.18 b).

In section 3.1.3 it was stated that the reflecting surface was positioned at a distance *wd* from the faceplate pupil and that $z_v > wd$. If this is the case light rays coming from the object won't strike the surface from right to left or perpendicular to the surface *z* axis. However if the surface is tilted these situations are possible (Figure 3.18 a).

After determining the intersection point of the incident ray with the surface and the opposite direction of the reflected ray [L',M',N'], the intersection point *z* coordinate is increased by Z_v. This step will return the intersection point to the *GLBTLT* axis. The direction and the point are then translated to the global system using equation(3.38). If the operation $z=z-(wd+z_{PD})$ is performed on the intersection point that was in the global system, the point will be translated to the *VTX* system. Equations(3.47) and (3.48) can then be used to determine the intersection with the pupil plane since they were derived for an intersection point on the surface expressed in the *VTX* system.

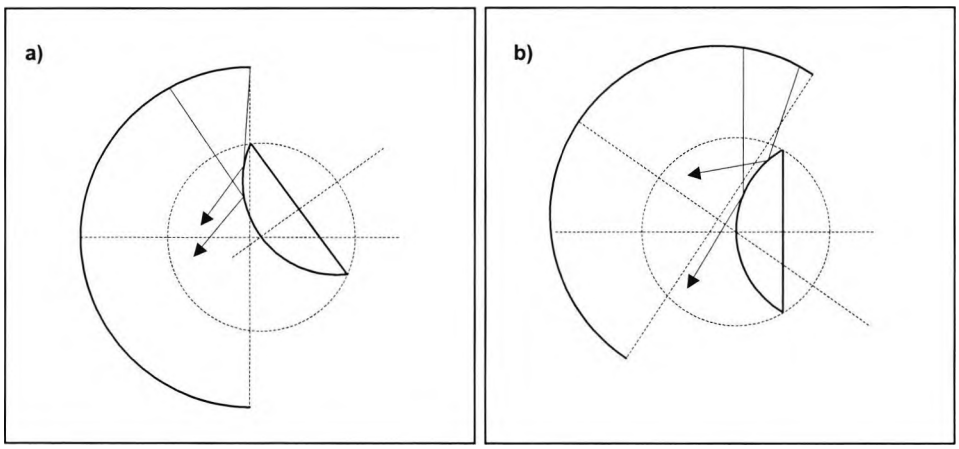

Figure 3.18 - When the reflecting surface is tilted (**a**) it's possible for some rays to strike it from right to left or perpendicular to the surface *z* axis. The procedure adopted for ray tracing with a tilted surface is such that the surface will be straight and the faceplate tilted (**b**). In this case the ray tracing equations will be the same when transferring to the surface.

3.7 Finding a transmitted ray through the faceplate pupil

A transmitted ray is necessary to determine the rays that strike the pupil edge after reflection. This procedure will be explained in the next section. It is not used if the reflecting surface is tilted or decentred.

For a centred reflecting surface there are always transmitted rays in the meridional plane. Due to the rotational symmetry of the faceplate and the reflecting surfaces used for this model it is sufficient to work in a single semi-meridian for many situations. Ray tracing can be performed in one semi-meridian and the results extrapolated to other semi-meridians. To find a transmitted ray the object point in the faceplate will be in the 90° semi-meridian and the problem will be solved for the vertical plane.

The process starts by tracing two rays and analysing the intersection of each with the pupil plane. One of the rays is directed to the reflecting surface superior edge and the other to the surface vertex (Figure 3.19). The former will be referred as the

by edge ray and the latter as the vertex ray. The vertex ray always strikes below the pupil except if the object point is on the pupil edge in which case it will hit the opposite side of the pupil after reflection. In the latter case it can be considered that the ray is transmitted and the problem is solved. The edge ray may strike the pupil plane after reflection below, in or above the pupil. If the edge ray strikes the pupil plane below the pupil it means that no transmitted ray can be found for that object point (Figure a). All rays touching the surface below the edge will intersect the pupil plane at an even lower point. If the edge ray is transmitted through the pupil the problem is solved in the first step (Figure b). If the edge ray strikes above the pupil the vertex ray intersection must be analysed.

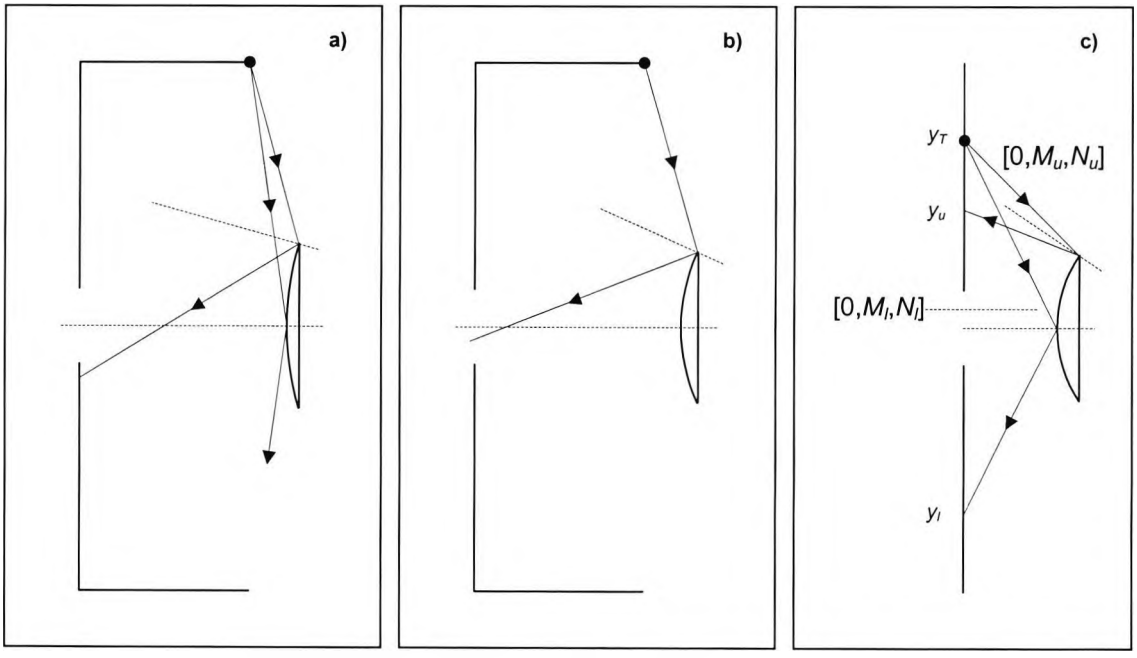

Figure 3.19 - Situations for which a light ray coming from an object point on the 90° semi-meridian directed to the upper reflecting surface edge on the meridional plane, after reflection strikes the pupil plane below (**a**), in (**b**) and above the pupil (**c**). The light ray directed to the surface vertex is always reflected below the pupil except if the object point is at the pupil edge (**c**).

When the edge ray strikes above and the vertex ray below the pupil, bracketing has been achieved since a transmitted ray will be found if it is directed between the

two. If a new ray is directed exactly in the middle of the initial two there is no guarantee that it will be transmitted. One solution is to continue to trace rays in the middle of each new pair of limits found. A second is to increment one direction in equal steps. Both procedures can be time consuming.

As an alternative, an iterative linear interpolation method was developed based on the ray's M direction cosine and the y intersection of the reflected ray with the pupil plane. The limiting ray that strikes the reflective surface higher will have the subscript u, and the one that strikes lower the subscript l. When the procedure begins the edge ray is u and the vertex ray l. Each iteration applies the equation

$$M = M_u + \frac{M_l - M_u}{1 - \frac{y_l}{y_u}} \tag{3.67}$$

to the limiting rays and a new ray is traced with the new direction for which the intersection with the pupil plane determined. If it strikes the plane above the pupil (but closer to the pupil edge) the new ray becomes the upper limit and if strikes below it becomes the lower limit. The iteration is repeated until a transmitted ray is found. The process is completed with a small number of iterations.

It is interesting to analyse the effect of equation(3.67): $M_u<0$ for the object points presented in Figure 3.19, but if the ray comes from an object closer to the pupil edge and the pupil diameter is smaller than the surface diameter, M_u can be positive or zero. M_l is always negative and larger than M_u, in magnitude value, therefore the numerator of the second term M_l - M_u is always negative. As for the y coordinates, $y_l<0$ and $y_u>0$ thus the denominator is always positive, hence the second term of the equation is negative. This forces the new ray to be directed lower than the edge ray as desired. If $|y_l|=y_u$ the new ray should have a direction equal to the average of the two limiting M values. If $|y_l|>y_u$ the new ray should have an M closer to M_u because it strikes the pupil plane closer to the pupil edge. If

$|y_l|<y_u$ the new ray should have an M closer to M_l for the same reasons. The denominator of the second term is 2, >2 and <2 respectively for each one of the cases stated above giving the desired result.

3.7.1 Special case: Edge ray fails to intersect the pupil plane.

This is a situation that must be analysed or else the transmitted ray procedure will fail in these circumstances (Figure 3.20). The vertex ray always strikes the pupil plane therefore it is sufficient to analyse the N component of the edge ray after reflection to see if it is directed to the pupil plane or not.

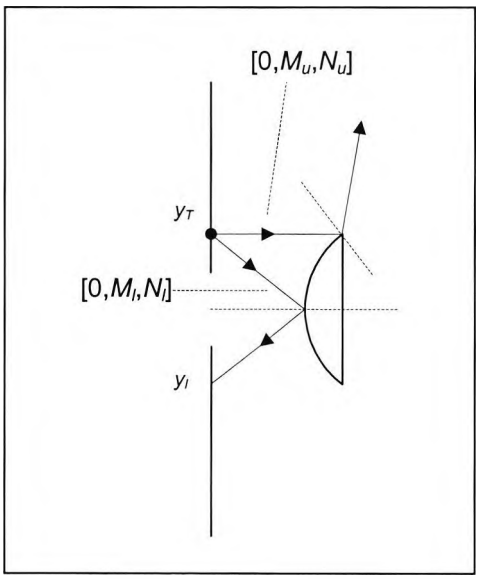

Figure 3.20 - The ray directed to the reflecting surface edge fails to intersect the pupil plane after reflection. This case has to be analysed separately or the transmitted ray searching procedure will fail.

If the edge ray can't be used to do the initial bracketing of the M values then a new ray must be traced in order to do so. If the vertex ray strikes below the pupil after reflection then there will always be a ray that will strike above the pupil (in the present conditions for the edge ray) and will have an M component between M vertex and M edge. A new ray was traced with $M=(M_u+M_l)/2$ and the intersection

coordinates with the pupil plane analysed. If the new ray strikes above the pupil the bracketing is completed and the transmitted ray searching procedure follows as normal. If it strikes below the pupil then it's a better limiting value than M vertex so it will become the new M_l. However the other bracketing limit remains to be determined therefore a new ray will again be traced with the average M component. If in the process to find the bracketing rays a transmitted ray is found, the procedure is terminated since that was the initial objective.

3.8 Pupil exploration in the meridional plane.

This procedure is used to determine the direction of the incident rays for which the reflected rays strike the pupil limits in the meridional plane (Figure 3.21). The position of the object point follows the same conditions applied to the transmitted ray finding algorithm. The M component of the incident ray that strikes the superior pupil edge after reflection will be referred to as M_{ut} and the one for the ray that strikes the inferior edge M_{lt}. A transmitted ray is available with an M direction cosine M_{tr} and striking the pupil plane at a coordinate y_{tr}, both determined by the transmitted ray finding algorithm.

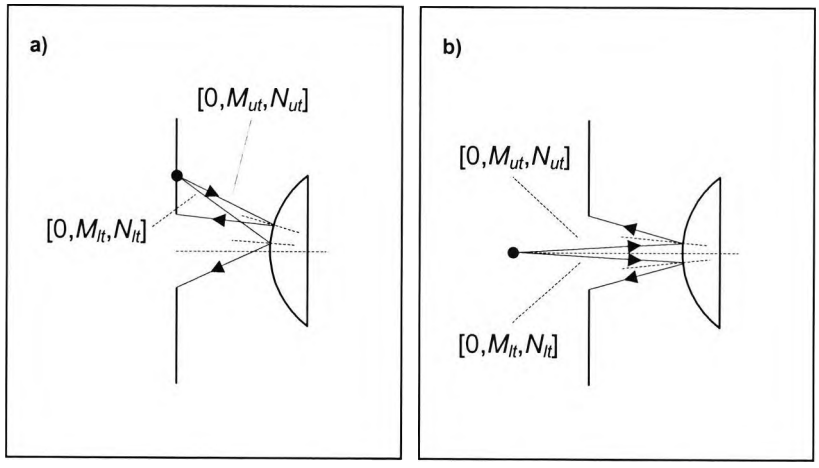

Figure 3.21 – a) Direction of the incident rays coming from an object point striking the pupil edges in the meridional plane after reflection. **b)** An imaginary object point is located on axis on the faceplate vertex. It doesn't belong to the faceplate since the faceplate is limited by the pupil plane. In this case M_{ut} and M_{lt} are symmetrical.

The initial step of this procedure will be to bracket the desired pupil edge between the transmitted ray and a ray that strikes above the pupil for the upper limit or below the pupil for the lower limit. Once again the M component of the edge ray and the one for the vertex ray are going to be used as starting points but now the problem is more complex.

The vertex ray should be the first to be tested since its path is predictable. Analysis of (Figure 3.20) shows that the vertex ray strikes below the pupil therefore it is only useful for determining M_{lt} being one of the limiting directions for bracketing. If the object point is on the upper pupil edge the vertex ray will be reflected to the opposite edge hence the vertex ray M direction cosine can be considered M_{lt} for this special case.

The edge ray will only be useful for determining M_{ut} since it will be reflected above the pupil. However when the reflected ray fails to intersect the pupil plane (Figure 3.20) this ray can't be used. This problem was solved in the transmitted ray finding procedure (section 3.7) and for the present case the same process is applied with the exception that the transmitted ray M direction cosine is used as a limit instead of M for the vertex ray.

Another interesting situation is displayed in Figure 3.19 b), where the edge ray is transmitted. This implies that no ray strikes the upper pupil edge after reflection since it would have to strike the reflecting surface at a higher point than the edge. This means that there is vignetting by the surface diameter. In this case the M component for the edge ray is considered M_{ut}.

When the desired pupil edge is bracketed by the transmitted ray M_{tr} and the ray that strikes the pupil plane above or below the pupil, with direction cosine M_F, a new ray is traced with M given by equation

$$M = M_{tr} + \frac{M_F - M_{tr}}{\dfrac{y_F - y_{tr}}{\pm\dfrac{PD}{2} - y_{tr}}}, \tag{3.68}$$

where PD is the pupil diameter. The positive sign is used if the upper pupil edge is being analysed and the negative is taken for the lower edge. The coordinates y_{tr} and y_F are respectively the y coordinates of the intersection of the transmitted ray and the ray that strikes outside the pupil with the pupil plane. A new ray is traced with the calculated M direction cosine that will strike the pupil plane closer to the pupil edge. The new M will replace M_{tr} or M_F in the equation depending on whether the ray was transmitted or failed respectively. The iterative process continues until the ray strikes close to the pupil edge within a pre-defined tolerance. This equation is a linear interpolation that will direct the new ray closer to the limiting ray that strikes the pupil plane at a shorter distance to the desired pupil edge.

There are no object points before the pupil since the faceplate is limited by it. If an imaginary object point on axis located before the pupil is used then a ray directed along the axis would be reflected in the opposite direction (zero incidence angle). This ray would intersect the pupil plane at y_{tr}=0 and M_{tr}=0. Equation (3.68) can still be applied to this case and M_{ut}=-M_{lt} (Figure 3.21 b). Using this procedure allows an estimate of the angular aperture of a pencil of rays for a set of particular vk parameters applied in the simulation.

3.9 Pencil of rays from an object point, ray density

The object points are part of the edges of luminous rings located in the instrument faceplate. A single object point will send a spherical wavefront and the light rays will be perpendicular to it. Only the section of the wavefront that's directed to the reflecting surface is relevant. That section is a solid angle and can be called a pencil of rays. This part of the thesis is aimed at determining the direction of each ray in order for the ray density to be uniform in the pencil of rays.

A central ray will determine the pencil direction and the other rays will revolve around it. The direction cosines for the central ray are $[L_c, M_c, N_c]$. A local axis system was defined in order for one of its unit vectors ($\hat{e}_2$) to coincide with the central ray direction (Figure 3.22). The transformation applied was similar to a spherical coordinates system and represented in matrix form by

$$\begin{bmatrix} \hat{e}_1 \\ \hat{e}_2 \\ \hat{e}_3 \end{bmatrix} = \begin{bmatrix} \cos\varphi & 0 & -\sin\varphi \\ \sin\theta\sin\varphi & \cos\theta & \sin\theta\cos\varphi \\ \cos\theta\sin\varphi & -\sin\theta & \cos\theta\cos\varphi \end{bmatrix} \begin{bmatrix} \hat{i} \\ \hat{j} \\ \hat{k} \end{bmatrix} \tag{3.69}$$

This transformation is much simpler than the one applied for the tilt system (equation (3.37)) because the angles φ and θ are measured between both system axes. This wasn't the case for the angle φ in the tilt system.

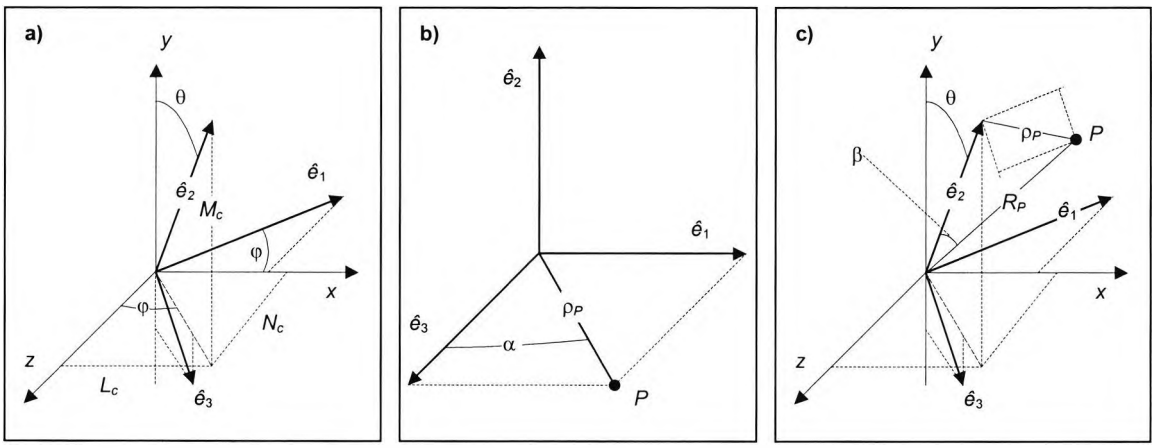

Figure 3.22 - Axis systems used to define the direction of a ray inside a pencil of rays. **a)** The unit vector $\hat{e}_2$ is the direction of the central ray in the pencil, the axis system *xyz* is not the global system but a local system with the same directions but with origin at an object point. **b)** This system is to be placed at the end of $\hat{e}_2$ on **a)**, it represents the position of a point *P* belonging to a ray in the pencil of rays. The unit vectors presented are just to define the directions. **c)** Representation of figures **a)** and **b)** together.

The trigonometric relations for angles φ and θ can be expressed in terms of the central ray direction components $[L_c, M_c, N_c]$ by equations

(3.70) $$\cos\varphi = \frac{N_c}{\sqrt{L_c^2 + N_c^2}} = \frac{N_c}{\sqrt{1 - M_c^2}},$$

(3.71) $$\sin\varphi = \frac{L_c}{\sqrt{L_c^2 + N_c^2}} = \frac{L_c}{\sqrt{1 - M_c^2}},$$

(3.72) $$\sin\theta = \sqrt{1 - M_c^2},$$

and

(3.73) $$\cos\theta = M_c.$$

It should be noted that in order to cover all space, φ will take values from 0 to 2π but θ is only required from 0 to π. Therefore $\sin\theta \geq 0$, which is in agreement with equation (3.72).

To represent the directions of the other rays revolving around the central ray a plane can be placed perpendicular to the central ray at a unit distance from the object point (Figure 3.22 b) and c), hence at the end of $\hat{e}_2$. The intersection of a ray with the plane is a point (P) with position in the plane represented by the vector

(3.74) $$\vec{\rho}_P = \rho\sin\alpha\,\hat{e}_1 + \rho\cos\alpha\,\hat{e}_3.$$

The position vector of this point

(3.75) $$\vec{R}_P = \rho\sin\alpha\,\hat{e}_1 + \hat{e}_2 + \rho\cos\alpha\,\hat{e}_3$$

from the local system with origin at the object point is the sum of $\hat{e}_2$ with the position vector at the plane ρ_P. The magnitude of R_P is $\sqrt{(1+\rho^2)}$. If R_P is transformed to the *xyz* system applying equation(3.69) the vector in the new system is given by

$$\vec{R}_P = \left[L_c + \frac{\rho}{\sqrt{1-M_c^2}} \left(N_c \sin\alpha + M_c L_c \cos\alpha \right) \right] \hat{i} + \left[M_c - \rho \cos\alpha \sqrt{1-M_c^2} \right] \hat{j} + \left[N_c + \frac{\rho}{\sqrt{1-M_c^2}} \left(-L_c \sin\alpha + M_c N_c \cos\alpha \right) \right] \hat{k} \quad (3.76)$$

If now this vector is divided by its magnitude, the resultant vector is the unit vector pointing the direction of a ray in the pencil of rays given by

$$\hat{\mu}_R = \frac{1}{\sqrt{1+\rho^2}} \vec{R}_P . \quad (3.77)$$

A solution could not be found for ρ in equation(3.74) in order for the vector R_p in equation(3.77) to represent the position of a ray in a spherical wavefront. Instead a section of the pencil by a plane perpendicular to the central ray was used and the intersection of the rays with that plane calculated by equal increments of ρ. However it should be noted that for a pencil of rays with a small aperture the linear increments are approximately equal to angular increments which will correspond to a spherical wavefront as desired. Tests executed on the simulation program have shown that this is the case for a set of typical videokeratoscope parameters.

The developed model uses a circle of radius R_0 centred at the central ray (Figure 3.23) hence with an area $A_0=\pi R_0^2$. If a circle of radius $R_1>R_0$ is centred at the same point, the area between circles (A_1) is the difference between the areas of the circles. If this area is divided in n_1 parts in such a way that each sector has the same area as the central circle a relationship between all parameters can be found. This procedure applied to the area (A_k) between circles of radius R_k and R_{k-1} is represented by

$$\frac{\pi R_k^2 - \pi R_{k-1}^2}{\pi R_0^2} = n_k . \quad (3.78)$$

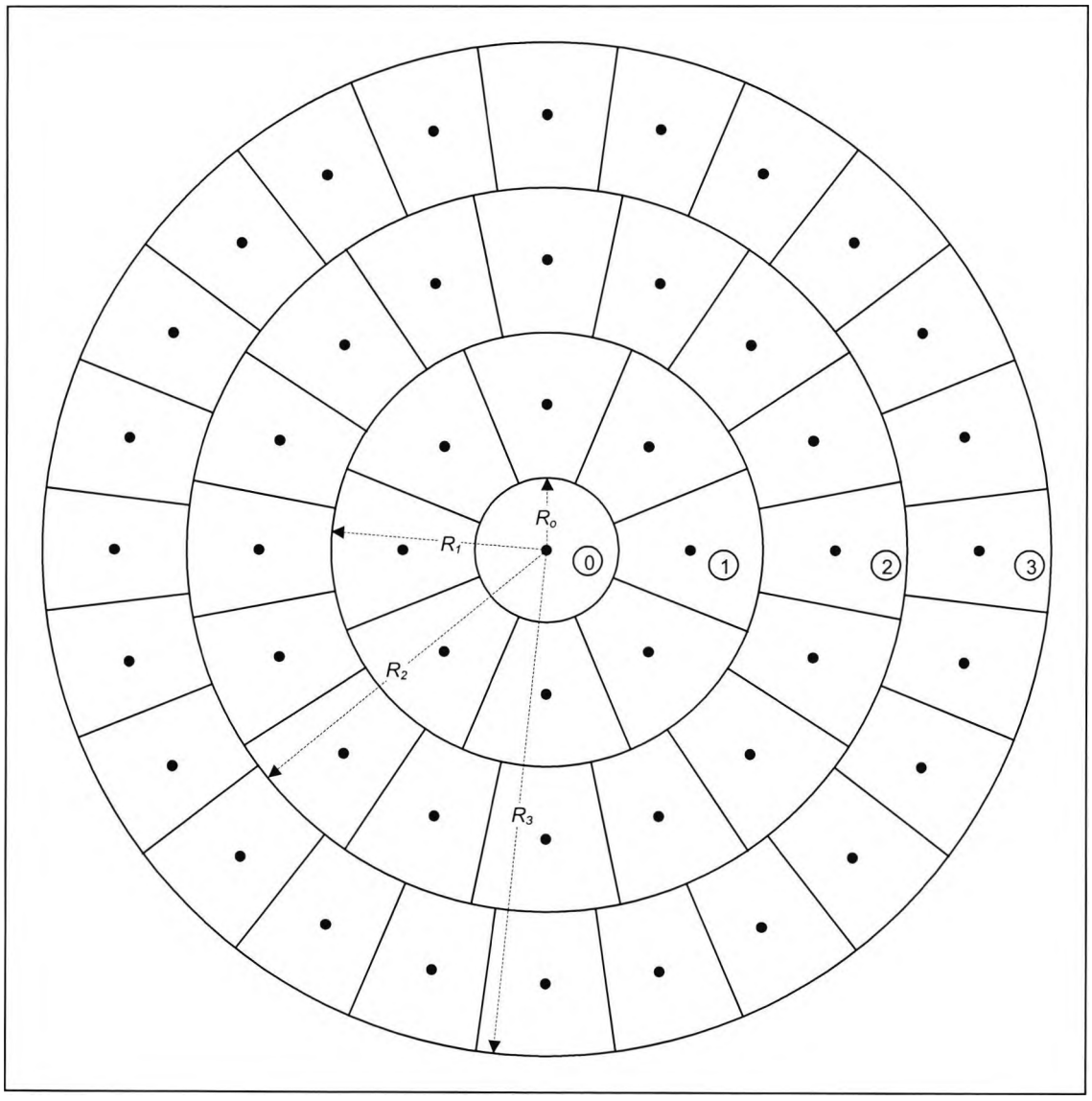

Figure 3.23 - Generation of an equal ray intersection density circular pattern in a plane. The ray intersections are disposed in circles around a central ray. Each intersection is located in the centre of an area equal to the area of the circle around the central ray (radius R_o). For the case displayed each area (k) external limiting circle has radius $R_k=(2k+1)R_o$. The numbers displayed are labelling the areas between two consecutive circles and do not relate to a particular sector.

Analysis of the previous equation shows that a simplification is achieved if each area radius results from equal increments (Δ) from R_0, $R_k=R_0+k\Delta$. If this expression is replaced in the last equation it gives

$$n_k = \Delta \frac{(2k-1)\Delta + 2R_0}{R_0^2}. \tag{3.79}$$

It can be seen that in order to obtain a greater degree of simplification the best value for Δ is a multiple of R_0, aR_0, for which n_k is

$$n_k = [(2k-1)a + 2]\,a. \tag{3.80}$$

Table 3.2 summarises the results for the n_k expression with a ranging from 1 to 4. The expressions for a=1 and a=2 seemed acceptable while the ones for a>2 appeared to result in an excessive number of rays per area. However this does not mean that the expressions for a>2 are wrong; they could still be used to provide an equal area effect. The values of n_k for a=1 and a=2 were analysed and the latter was chosen due to a property that allows to use previously traced rays. This will be developed in the next section.

a	n_k
1	$2k+1$
2	$8k$
3	$18k-3$
4	$32k-8$

Table 3.2 - Expressions for the number of ray intersections (n_k) on a ring area (k) limited by radius R_k and R_{k-1} where $R_k=R_0+kaR_0$.

The initial value for R_0, controlling the ray density, cannot be constant for all object points. This is due to the fact that the aperture of the pencil of rays will depend on

pupil size, distance of the reflecting surface to pupil, surface parameters and object point taken. Therefore a constant value cannot be used since it could be adequate for one set of parameters but too low for another set and too high for another. To solve this problem the imaginary on-axis object point before the pupil was used (Figure 3.21 b) as described in section 3.8.

From Figure 3.23 the radial distance between points in adjacent areas is $2R_0$. The equal density pattern plane was placed perpendicular to the z axis at a distance N_{uti} from the imaginary object point (Figure 3.24 a). The symbol R_{0i} is going to be used for the imaginary object point to distinguish between R_0 for an ordinary object point. The upper tangential ray $[0,M_{uti},N_{uti}]$ marks the position of the outer point on the ray density pattern. The number of rays n_R will be the number of divisions to apply to M_{uti}. If each division is $2R_{0i}$ the relation between this parameter and M_{uti} is expressed by

(3.81) $$M_{uti} = 2R_{0i}n_R \,.$$

The angle of R_{0i} with the axis (representing the central ray in this case) is γ_{Roi} and is given by:

(3.82) $$\gamma_{R0i} = \arctan\frac{R_{0i}}{\sqrt{1-M_{uti}^2}} \,.$$

For an equal energy pattern associated with a central ray coming from any object point R_0 is related to the number of rays n_R by

(3.83) $$R_0 = \tan\gamma_{R0i} = \frac{M_{uti}}{2n_R\sqrt{1-M_{uti}^2}} \,.$$

It should be remembered that, for an ordinary object point, the plane used to define the ray pattern is placed perpendicular to the central ray at 1 mm from the object point measured along that ray (Figure 3.24 b). Now the parameter ρ representing the distance from the central ray to another ray in the plane perpendicular to the first is

(3.84) $$\rho = 2R_0 k\,,$$

with k taking integer numbers from 1 until a number that fails the reflecting surface. Angle α in equation(3.76), which represents the angular location of a point in the equal density pattern for an area k, is given by

(3.85) $$\alpha_k = j\frac{2\pi}{n_k}$$

The parameter j is incremented in steps of 1 from 0 to n_k-1.

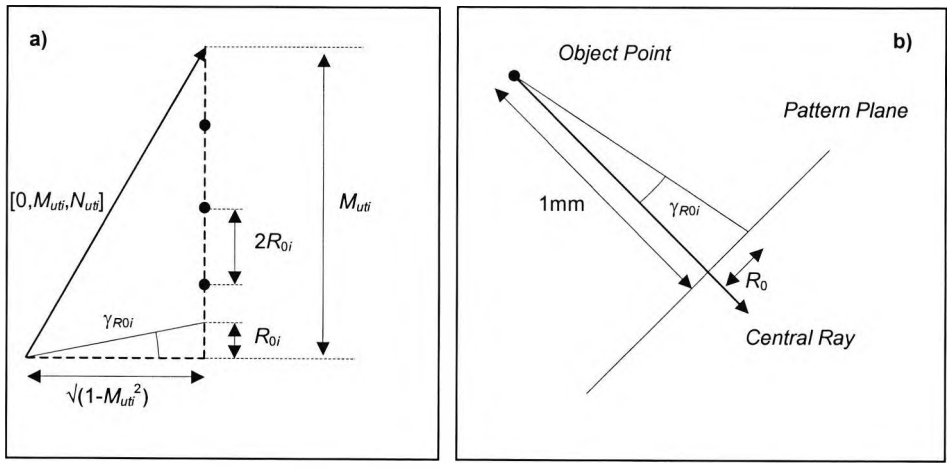

Figure 3.24 - a) Equal density pattern positioned perpendicular to the z axis (central ray for the imaginary object point) and limited by the upper tangential ray. R_{0i} depends on the number of divisions to M_{uti}. **b)** Angle γ_{R0i} is used to calculate R_0, for any object point, determining the ray density.

3.9.1 Retracing a pencil of rays with higher density

For purposes that will be discussed in the following sections it is necessary to recalculate the pencil of rays associated with a particular central ray for a higher density. When the ray density is too high this process takes a long time. A procedure was developed in order to use the rays traced previously under specific conditions resulting in faster execution time. Analysis of Figure 3.23 shows that the radial distance between rays in two consecutive areas is $2R_0$. If a new pencil of rays associated with the same central ray is traced with a new central radius $R_{0new}=R_{0old}/2$, the radial separation between consecutive areas will now be equal to $2R_{0new}=R_{0old}$ (Figure 3.25).

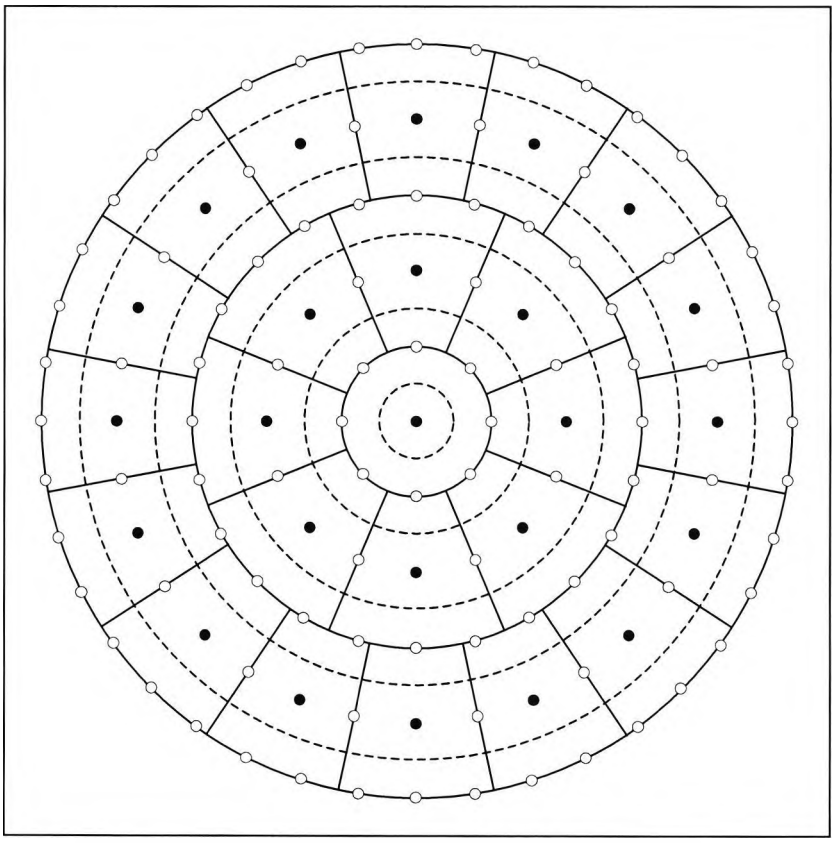

Figure 3.25 – The full lines and dark dots correspond to the pattern presented in the previous figure for areas 0, 1 and 2. The dashed lines and light dots correspond to a pattern where the central radius is halved from the previous value. The new odd numbered area centres will coincide with the inner borders of the old areas. The new even area centres will coincide with the old area centres needing twice as much rays therefore the old ones can be reused.

The centres of sectors in the new odd numbered areas will coincide with the internal borders of the old areas. However the centres of sectors in the new even numbered areas will be located at the same radial distance from the central ray as the old sector's centres. Therefore the sector centres for the new area $2k$ are at the same radial distance from the centre as the sector centres for the old area k. From the simplified expression for the number of rays in an area k $n_k=8K$ it is obvious that $n_{2k}=16k=2n_k$. Hence the rays in the new even areas will have doubled in relation to the old areas and are located at the same radial distance from the centre. If the position of the old rays was stored they will coincide with half the rays for the new even areas and therefore only the other half of the rays needs to be traced for those areas. All the rays for the new odd areas will have to be traced since there were none at these positions originally.

3.9.2 Special case: pencil of rays with central ray in the y axis direction.

For a ray in the y axis direction $M_c^2=1$ and $L_c=N_c=0$ hence equation(3.76), representing the position of a ray in the pencil of rays expressed in the local xyz axis system, cannot be used. In this case it is better to work directly in the xyz local system with angle α being described in a plane parallel to the xz plane located at the end of the unit vector representing the central ray direction (Figure 3.26). The angle will start from a line parallel to the z axis in the plane. The following equation

(3.86) $$\vec{R}_p = \rho \sin\alpha\, \hat{i} \pm \hat{j} + \rho \cos\alpha\, \hat{k}$$

represents the position vector R_P although the unit vector pointing in the direction of R_P is still given by equation(3.77). The $\pm$ sign in equation(3.86) depends on the direction of the central ray.

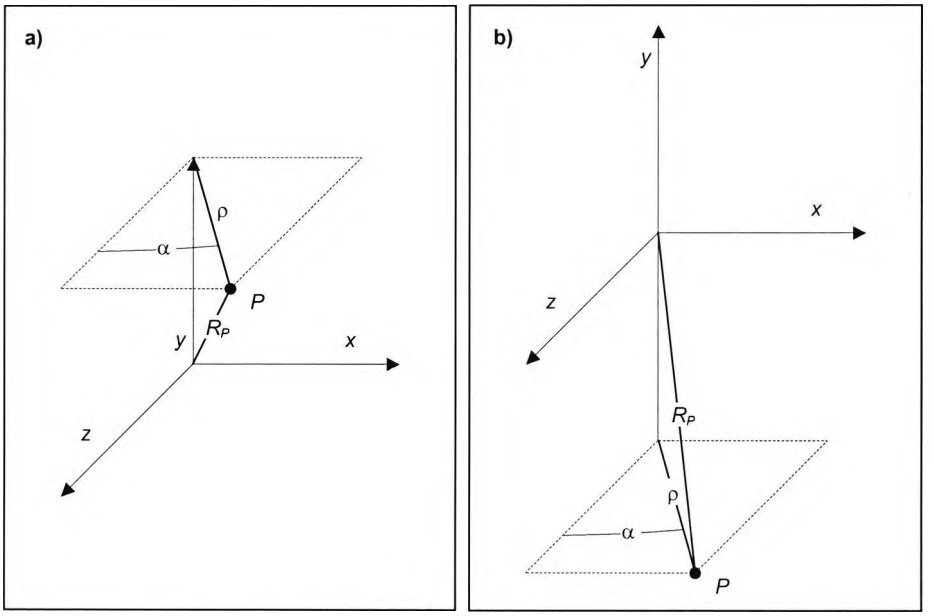

Figure 3.26 - Representation of the position of a ray in a pencil of rays with a central ray in the *y* direction (**a**) and -*y* direction (**b**).

3.9.3 The central ray

For a centred reflecting surface the central ray of a pencil of rays from an object point was considered to be in the meridional plane bisecting the directions of the upper and lower rim rays. For an object point in the 90° semi-meridian the bisection angle δ_c (Figure 3.27) is given by

(3.87) $$\delta_c = \frac{\arctan\left(\frac{M_{ut}}{\sqrt{1-M_{ut}^2}}\right) + \arctan\left(\frac{M_{lt}}{\sqrt{1-M_{lt}^2}}\right)}{2}.$$

It should be noted that this angle will be negative due to the previous equation for this particular case. The direction cosines $[L_c, M_c, N_c]$ representing the central ray direction are

(3.88) $$[L_c, M_c, N_c] = [0, \sin\delta_c, \cos\delta_c]$$

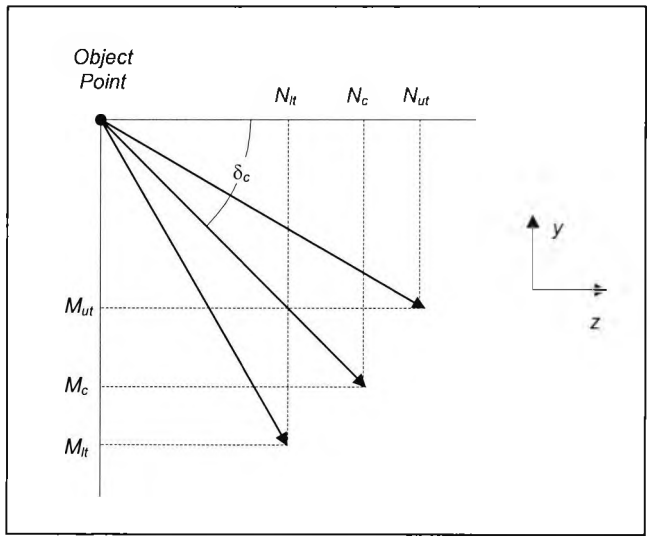

Figure 3.27 - Direction cosines representing the upper rim ray $[0,M_{ut},N_{ut}]$, lower rim ray $[0,M_{lt},N_{lt}]$ and central ray $[0,M_c,N_c]$, from an object point, for a centred reflecting surface. The central ray was considered to be the one bisecting the two rim rays.

For the present case $M_c<0$ and $N_c>0$, which is accurately represented by this equation.

The advantage of using the central ray of a pencil bisecting the rim rays in the meridional plane is illustrated in Figure 3.28. The best example is the imaginary on-axis object point for which the ray bisecting the rim rays is coincident with the z-axis since the rim rays are symmetrical. A section of the pencil in these conditions is perpendicular to the z-axis. The circle displayed in the figure is the front view of the corneal area for which rays from the on-axis object point are transmitted after reflection. Analysis of Figure 3.21 b), helps to understand this configuration. Due to rotational symmetry this area is determined in the pupil exploration algorithm with great accuracy and will remain constant independent of the ray density used. Any ray from the on-axis object point intersecting the reflecting surface outside this area will not be transmitted. In Figure 3.28 a), the central ray of the pencil is bisecting the rim rays and only 5 circular areas of the pencil section were needed to cover the reflecting surface area that transmits rays. On Figure b) the central ray is

directed elsewhere therefore more areas of the pencil section are needed to cover the same reflecting surface area. For this particular case section areas 6, 7, 8 and 9 had to be used as well which totals an extra 240 rays. It should be noted that all rays in a section area have to be traced to determine if they are transmitted or not. A low ray density was used in this example but for the simulation of an image a very high density has to be employed and the number of extra rays needed grows exponentially. However due to the equal density pattern applied this problem is only relevant in terms of execution speed since for a high ray density the final image will be the same regardless of the position of the central ray on the incident pencil. For an off axis object point the problem is not so easy to illustrate but the principle is the same. In this case the reflecting surface area that transmits rays will only be symmetrical in the sagittal plane. The upper and lower rim rays will limit this area in the meridional plane.

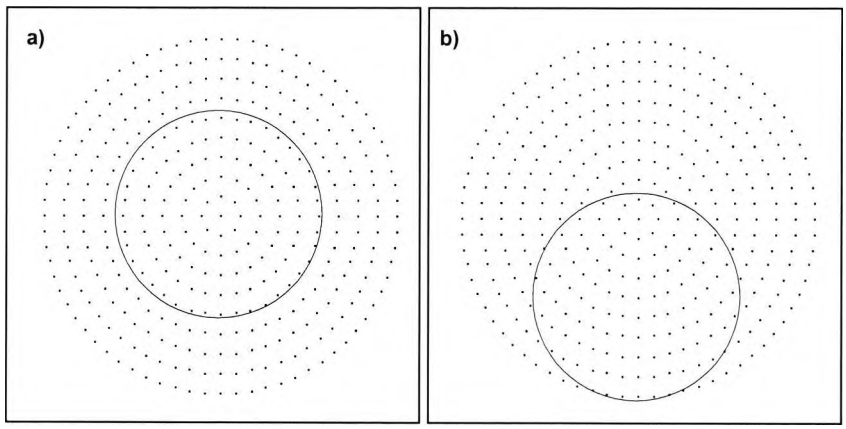

Figure 3.28 – Section of a pencil of rays coming from the imaginary object point on axis. The circle represents the front view of the reflecting surface area that transmits rays, after reflection, from the on-axis point. **a)** The central ray of the pencil is on-axis hence bisecting the upper and lower rim rays. **b)** The central ray is still in the meridional plane but is not bisecting, as a result more rays have to be traced to get the same effect.

For a non-centred reflecting surface (tilted and/or decentred) there is no meridional plane as the object point, faceplate and reflecting surface axis are not in the same plane. As a result all image symmetry will be lost. However if the tilting and/or

decentring are executed in the meridional plane then the image will still have planar symmetry for that object point. It was decided not to develop a special process for this situation and maintain a general procedure. At the start of the procedure the central ray of the pencil was directed to the reflecting surface vertex and rays were traced covering the surface completely. Then from the transmitted rays, the one closest to the pupil centre was selected to be the central ray of the effective pencil to be traced. The selection of this particular ray was done as a matter of simplicity, since the determination of the ray that strikes the centre of the reflecting surface area that transmits rays is a complex procedure.

The procedures developed for the centred surface are very powerful and if there was a single transmitted ray in the meridional plane it would be found by the routines. Unfortunately that is not the case for the non-centred surface routines. Due to the lack of a meridional plane the ray finding procedure has to be applied to the entire reflecting surface against a meridional plane analysis for the centred surface. As a result the ray density used in the search cannot be very high due to the long time it takes to cover the entire surface. This can lead to finding no transmitted rays when in fact there may be some.

3.9.4 Limiting the pencil of rays from an object point

As stated previously a pencil of rays is controlled by the number of circular areas in its section, hence the problem is the number of areas to use. The limit is reached when all the rays traced in a circular area fail to be transmitted. This can be pictured in Figure 3.28 a) all rays in area 6 won't be transmitted and on Figure b) the same happens to area 10 (not pictured). Although this figure was designed for an on-axis object point it can be extrapolated to any object point, tilting or decentring of the reflecting surface just to illustrate the principle.

An exception occurs for the central ray finding procedure used for a non-centred surface. The first step was to direct an initial central ray to the surface vertex and then trace a pencil of rays around it. However that first ray may not be transmitted

and this could also happen to the first area of the pencil as well, therefore the procedure cannot stop at the first area since the entire reflecting surface must be covered. The approach followed was to continue tracing rays in new circular areas until all the rays in an area failed to intersect the reflecting surface. It should be noticed that in order to cover the entire surface the aperture of the pencil is large and therefore the calculated section of the pencil won't represent a uniform density pencil. However in this case the image is not being calculated it is only a case of finding a transmitted ray suitable to be the central ray of the effective pencil. After that the normal pencil limits based on the transmitted rays is applied.

3.10 Central reference point of the ring images

Videokeratoscopes use the height of ring mire images along several semi-meridians for the reconstruction algorithms. This corresponds to a polar coordinate system, which is always associated with a local Cartesian system. The latter will be the *IMG* system defined in section 3.3. It should be noted that the origin of this system is not necessarily along the videokeratoscope axis (Figure 3.7 a).

If the ring mire images are perfectly centred on the videokeratoscope axis, it is obvious that the origin of the *IMG* system should be placed on the axis. The majority of investigators in the corneal topography field assume a perfect centration and specify ring image mire heights in terms of distance from instrument axis, for example Roberts (1994b).

One of the aims of this research project is to study the effect of decentration on the topographic maps. If the origin of the *IMG* system is kept on the videokeratoscope axis for a decentred reflecting surface the situation displayed in Figure 3.29 a) may arise. This can happen with a small pupil (hence small first ring) or for a reflecting surface with a short apical radius of curvature. It can be seen in Figure 3.29 that for the semi-meridian σ there would be two heights for ring 1 and the image height for semi-meridian $180°+\sigma$ would be negative, which doesn't make sense. This can be avoided if the origin of the *IMG* system is placed at the centroid of the inner ring

image mire. At least one team of researchers (Andersen et al. 1993a) has adopted this approach to allow for small decentrations due to alignment error. This was also the initial approach taken for this project. However it was also found that if a fixation light is used in the simulation, its image centroid was very close to the centre of the inner ring. The difference was negligible therefore the fixation light approach was followed since it is faster and simpler to implement in the program. The fixation light was considered to be located at the faceplate vertex for conoids, or in the middle of the pupil for cylindrical and flat faceplates.

Although the fixation light was the preferred method for the determination of the origin of the *IMG* system, the program still allows centring at the inner ring image mire centre if desired. For abbreviation the centre of the *IMG* system of axis will be referred by o_I. This point will have coordinates (o_{Ix}, o_{Iy}) in the *IMG* system (applied to the global system) and if expressed in the global system ($-o_{Ix}$, o_{Iy}).

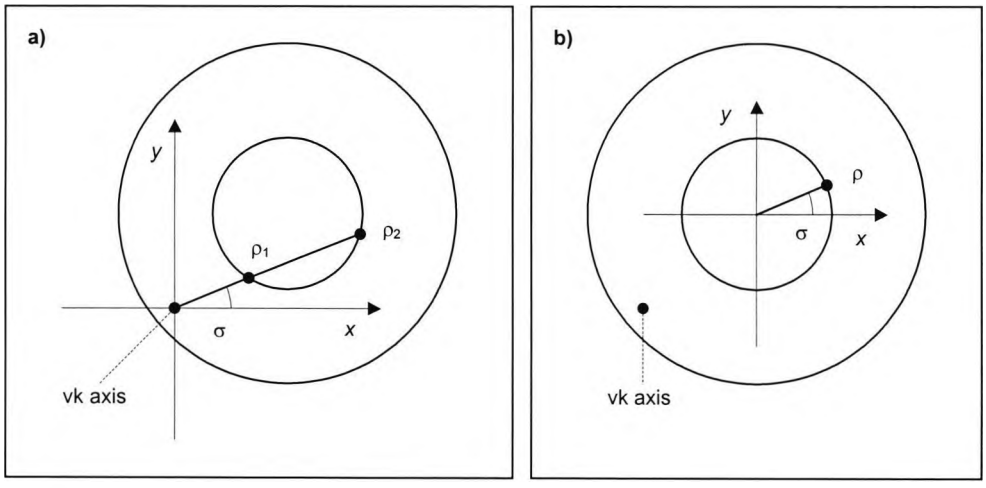

Figure 3.29 - Decentred image of the first and second ring mire images, the videokeratoscope axis is not located at the centre of the first ring. If the *IMG* system of axis used for the ring height is kept at the videokeratoscope axis than a ring may have two heights ρ_1 and ρ_2 in one semi-meridian σ (**a**). If the *IMG* system is placed at the inner ring mire image centre the problem will be solved (**b**).

It should be noted that if the image hasn't got rotational symmetry around the videokeratoscope axis, the position of the rings will change slightly with focus.

Therefore the point o_I has to be recalculated for each position of the image plane. This is the case for a non-centred reflecting surface.

3.11 Videokeratoscope alignment simulation

As stated in section 2, videokeratoscopes use a fixation light to align the reflecting surface with the instrument axis (*z* axis of the global system). When the image of the fixation light coincides with the centre of the screen (or other point representing the position of the instrument axis on screen) and the rings are in focus the image is captured.

Figure 3.30 a) shows a decentred reflecting surface and an axial ray coming from the centre of the fixation light. The image in the image plane will not coincide with the videokeratoscope axis, telling the instrument that the surface is misaligned. The operator will then move the instrument in the xy plane until the image of the fixation light is on axis (Figure b). This shows that surface decentring may not be significant, since is controlled by the instrument, although very small errors may still be possible.

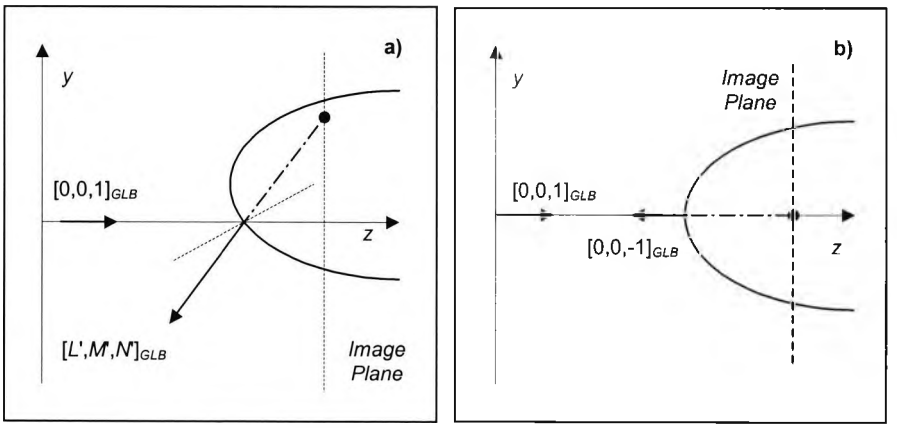

Figure 3.30 – a) The axial ray coming from the centre of the fixation light and striking a decentred reflecting surface. The image on the image plane won't coincide with the videokeratoscope axis. **b)**The same ray striking a centred reflecting surface, the image of the fixation light will coincide with the videokeratoscope axis therefore the alignment process was concluded.

When trying to align a tilted reflecting surface a peculiar situation arises. A perfect alignment can be achieved in a tilted surface without the need to realign its axis with the videokeratoscope axis. This is observed when an axial ray coming from the fixation light hits the reflecting surface in a point with a normal parallel to the incident ray. In these conditions the ray is reflected in the direction of incidence hence the image of the fixation light will appear to be in the centre of the image plane Figure 3.31.

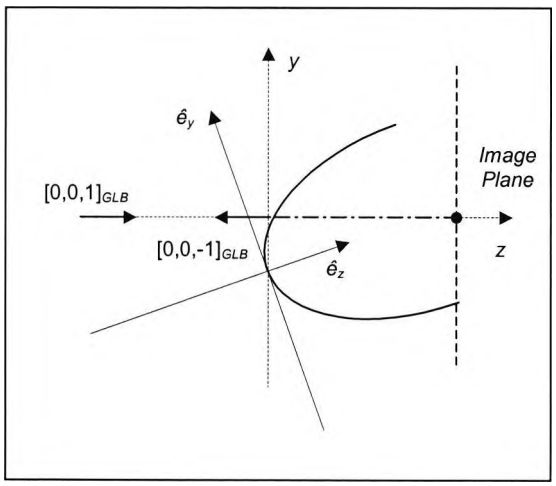

Figure 3.31 – Tilted and decentred surface in order for an axial ray from the fixation light (direction $[0,0,1]_{GLB}$) to strike a surface point with normal parallel to the incident ray. In this case the incident ray is reflected in the opposite direction $[0,0,-1]_{GLB}$. The normal to the tilted surface in the point where the ray strikes is also $[0,0,1]_{GLB}$. In these conditions the image (black dot) of the centre of the fixation light will be in the centre of the image plane. The videokeratoscope will assume that the surface is centred due to the correct alignment in the videokeratoscope axis (*z* axis).

To determine the coordinates of the surface point in question, consider a reflecting surface with rotational symmetry tilted by an angle θ around its vertex on the 90° semi-meridian. In this case an axial ray coming from the centre of the fixation light will be reflected down hence its image will be shifted upwards on the image plane (Figure 3.32 a).

As stated in section 3.6.3 it is better to use the tilted axis system *VTXTLT* for which the tilted surface will appear straight (Figure 3.32 b). It should be noted that the directions of the incident and reflected rays must be changed to this system by application of equation(3.37). The new directions for these rays will be respectively $[L,M,N]_{TLT}$ and $[L_2',M_2',N_2']_{TLT}$.

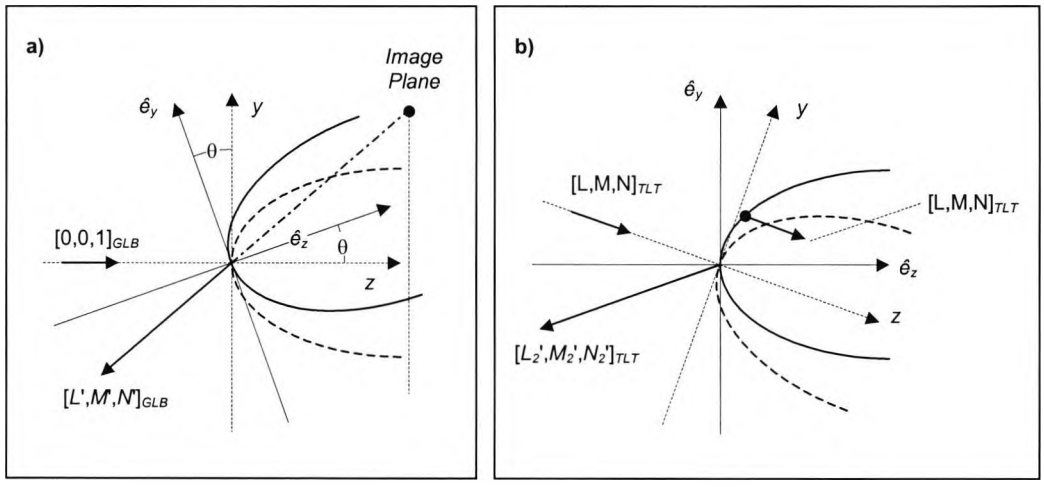

Figure 3.32 – a) A reflecting surface with rotational symmetry is tilted by an angle θ in the 90° semi-meridian. In this case an axial ray is reflected downwards. **b)** The system of axis is changed to *VTXTLT* and therefore the surface is straightened as explained in section 3.3. It is always possible to find a point on the surface (black dot) for which the normal has the same direction as the incident ray along the videokeratoscope axis.

It will always be possible to find a point on the surface with normal pointing in the same direction as the incident ray from the fixation light centre. This point will lie on the tilt plane and so will its normal. However this can only happen on a surface with rotational symmetry or in the principal meridians of non-rotational symmetric surfaces. This is due to the fact that for these cases the normal to the surface lies in the meridional plane (defined by the object point and the axis of the reflecting surface) (Wang et al. 1991 and Klein 1997). The coordinates of this point in the *VTXTLT* system of axis will be determined by equalising the incident ray direction with the normal equation(3.8) using $x_V=y_V=0$. This will result in coordinates given by

$$
(3.89) \qquad \begin{cases} x_N = -\dfrac{L}{c}\sqrt{1-2c(p-1)z+c^2p(p-1)z^2} \\ y_N = -\dfrac{M}{c}\sqrt{1-2c(p-1)z+c^2p(p-1)z^2} \\ z_N = \dfrac{\left[p-N^2(p-1)\right]-\sqrt{N^2\left[p-N^2(p-1)\right]}}{cp\left[p-N^2(p-1)\right]} \end{cases}.
$$

The parameter *wd* was defined as the distance from the pupil plane to the *z* coordinate of the reflecting surface vertex in the global system and should not be changed once defined. Therefore when moving the tilted surface this has to be taken into account decentring only on the *xy* plane of the global system. The reflecting surface will then be decentred along the line defined by the intersection of the *xy* plane of the global system and the tilt plane in order to match the incident ray with the surface point having a normal in the same direction. Figure 3.33 represents this decentration viewed in the *VTXTLT* system and Figure 3.31 the final result in the global system. Therefore a perfect alignment can be achieved with a tilted surface which will lead to reconstruction errors.

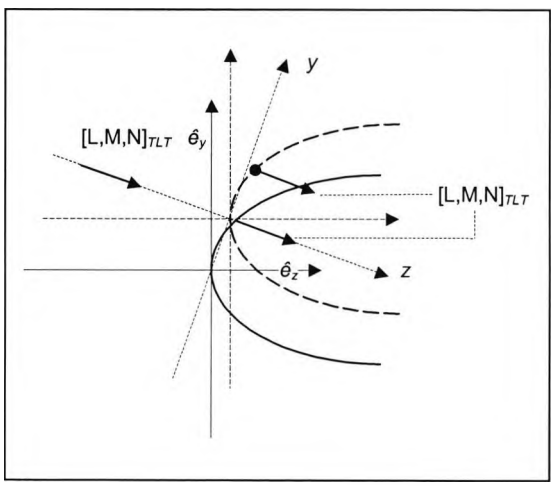

Figure 3.33 - The reflecting surface is decentred along the line defined by the intersection of the tilt plane (paper plane for this case) and the *xy* plane of the global system (left figure). The decentration is applied in order to match the incident ray from the centre of the fixation light with the point with a normal matching that direction.

In section 3.3. the tilt plane was defined in the *xy* plane of the global system by angle φ, Figure 3.8 a). Therefore the intersection of both planes is a line with direction $[\cos\varphi,\sin\varphi,0]_{GLB}$. If this direction is passed to the tilt system by application of equation(3.37) the resultant vector will be $[L\varphi,M\varphi,N\varphi]_{TLT}$. Considering Figure 3.33 it can be seen that the decentration applied to the surface will place the selected surface point $(x_N,y_N,z_N)_{TLT}$ at the *VTXTLT* axis system origin hence its coordinates are (0,0,0). If the vector line equation is written using these parameters it becomes

(3.90) $$(0,0,0)=(x_N,y_N,z_N)_{TLT}+\lambda\left[L_\varphi,M_\varphi,N_\varphi\right]_{TLT},$$

and solving this equation for λ gives

(3.91) $$\lambda=-\frac{x_N}{L_\varphi}=-\frac{y_N}{M_\varphi}=-\frac{z_N}{N_\varphi}.$$

This is very useful since one or two direction cosines of the vector $[L\varphi,M\varphi,N\varphi]_{TLT}$ may be zero and there will always be at least one component remaining to determine λ. The absolute value of the parameter λ is the decentration magnitude along the vector. If λ is negative it means that the decentration must be applied in the opposite direction of $[L\varphi,M\varphi,N\varphi]_{TLT}$. It should be recalled that this vector is $[\cos\varphi,\sin\varphi,0]_{GLB}$. Therefore, if λ is negative, the corresponding semi-meridian to apply the decentration to is $\varphi\pm180°$ depending on whether $\varphi<180°$ or $\varphi>180°$ respectively. If the semi-meridian needs to be specified from the examiner's point of view (angle σ) then the relations in Figure 3.7 can be applied.

The general principle specified in this section can be applied outside the principal meridians of a tilted reflecting surface without rotational symmetry. As stated earlier, in this case the normal to the surface is not in the meridional plane.

Therefore a decentration in this plane will never align the surface with the videokeratoscope axis. However a decentration outside the meridional plane makes the alignment possible.

3.12 Focus

3.12.1 Focus parameters

For a centred surface the position of the image plane was expressed in relation to the paraxial plane. The position of the latter (s_{parax}) was calculated by the paraxial formulas for a mirror (Hecht 1998) expressed by

(3.92) $$\frac{1}{s_o}+\frac{1}{s_{parax}}=-\frac{2}{R},$$

where R is the apical radius of curvature of the reflecting surface, s_o the distance from the object to the mirror vertex and s_{parax} the distance from the mirror to the paraxial plane (Figure 3.34 a). For a convex mirror $R>0$ and $s_{parax}<0$ (virtual image). The object point used was the imaginary object point on the faceplate vertex. For an object point located to the left of the mirror vertex $s_o>0$. Applying these conditions to the paraxial formula and simulation parameters the position of the paraxial plane was calculated from

(3.93) $$s_{parax}=\frac{R(wd+z_{PD})}{2(wd+z_{PD})+R}.$$

It should be noted that the negative sign was disregarded but s_{parax} is located to the right of the mirror vertex as displayed in the figure (virtual image). The position of the image plane is expressed by

(3.94) $$s_i=s_{parax}+DF,$$

where the user specifies the distance from the paraxial plane (*DF*). This parameter was considered positive if the shift was to the right of the paraxial plane and negative if to the left.

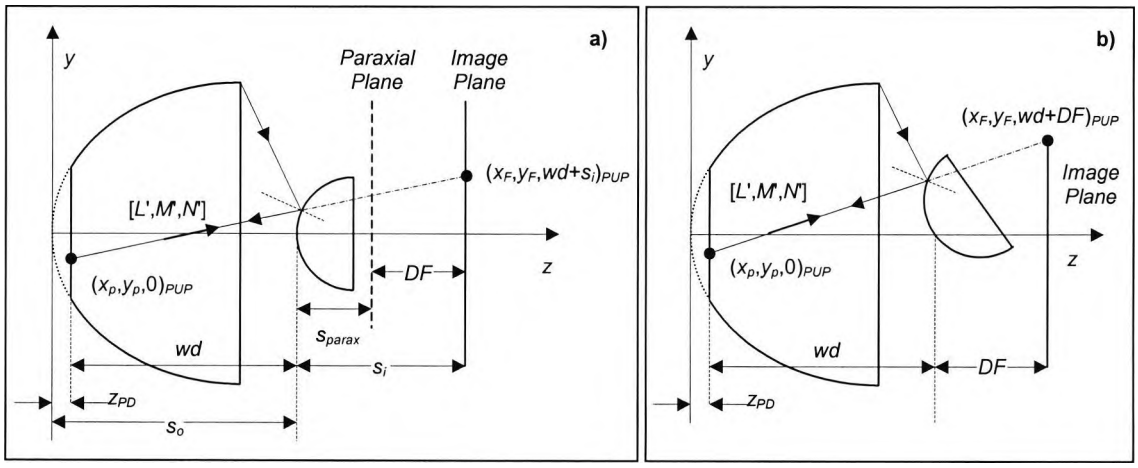

Figure 3.34 - Parameters defining the position of the image plane (*DF*) for a centred (**a**) and tilted or decentred reflecting surface (**b**). For a centred surface *DF* was measured from the paraxial plane while for a decentred or tilted surface it was measured from the vertex *z* coordinate in the global system.

After executing the ray tracing procedure for a single ray the point of intersection with the pupil plane (x_p,y_p,0) and the opposite direction of the reflected ray [*L*',*M*',*N*'] are available (see section 3.6). The point in the pupil is expressed in an axis system parallel to the global system but with origin at the pupil centre (abbreviated as *PUP*). The intersection of this ray with the image plane is obtained by following the path of the reflected ray beyond the reflecting surface (Figure 3.34). Using the pupil as the origin of the axis system, this point has coordinates (x_F,y_F,wd+s_i), which are calculated by applying the vector equation of a straight line resulting in

(3.95) $$(x_F, y_F, wd + s_i) = (x_p, y_p, 0) + \lambda[L', M', N'].$$

The result is a system of three equations with the solution for λ expressed by

(3.96) $$\lambda = \frac{wd + s_i}{N'}.$$

For a tilted or decentred reflecting surface there is no paraxial plane since the axis of the surface and faceplate are not coaxial. Therefore the focus cannot be expressed in relation to that plane. The position of the image plane was therefore measured from the surface vertex *z* coordinate expressed in the global system (Figure 3.34 b). The sign of the parameter *DF* follows the same convention adopted for the centred surface. The image plane also moves along the *z* axis of the global system although the reflecting surface may be tilted. The position of a point in the image plane follows exactly the same procedure applied to the centred surface, the only difference is that $s_i = DF$. It should be remembered that the ray tracing procedures for a tilted surface were executed in the tilted system but the final direction and intersection with the pupil plane were translated to the global system (with origin at the pupil plane).

3.12.2 Best focus for a centred reflecting surface

When a ring is used as an object the best focus is located at the tangential focal plane (Hecht, 1998). The problem is that oblique astigmatism cannot be isolated, the other aberrations are present as well. As a result it was found (using the simulation program) that a tangential focal line couldn't be obtained, but there was a position for which the spot diagram had a minimum blur in the meridional direction. The minimum meridional blur increased with object eccentricity. This observation lead to the assumption that the lack of a tangential focal line was due to coma. This aberration increases with object eccentricity explaining the increment in minimum meridional blur.

Figure 3.35 shows a sequence of spot diagrams obtained by shifting the image plane position. It can be seen that a minimum meridional blur is displayed on the top Figure c). This corresponds to the position of the image plane for which the upper and lower rim rays intersect. It is also curious to note that at this particular position the central ray marks the other end of the spot diagram.

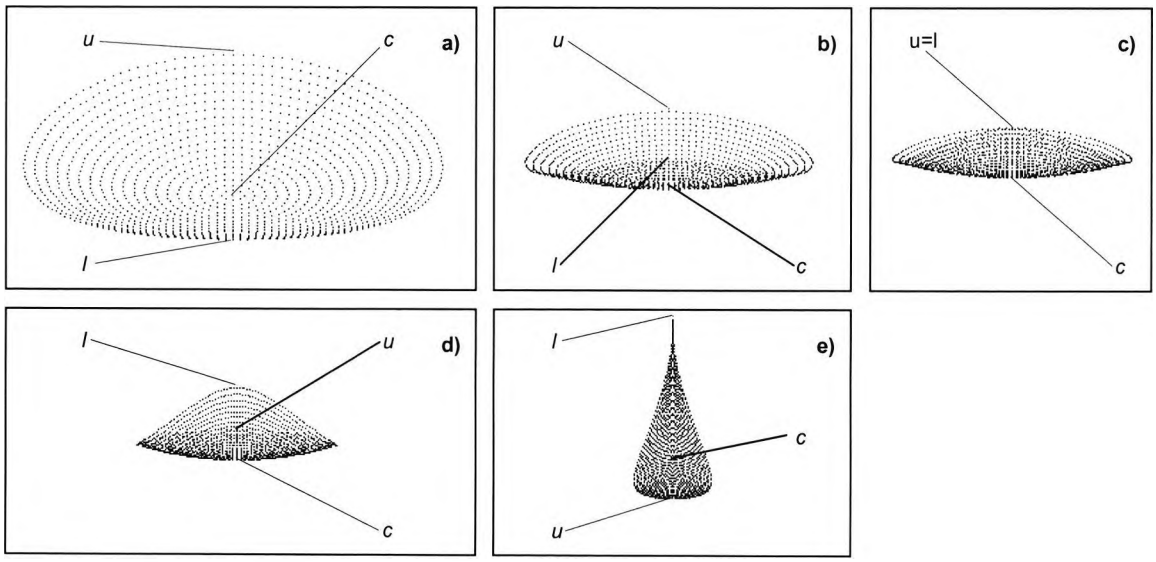

Figure 3.35 - Spot diagrams for a spherical faceplate with a 250mm apical radius limited by a maximum diameter of 300mm and a 9mm pupil. Reflecting surface p=0.82 apical radius of 7.75 mm limited by a 9mm diameter and wd=80mm. The object point has 15° eccentricity in the 90° semi-meridian and the images have a 720X enlargement with a ray density of 20 rays. Defocus in mm from the paraxial plane is 0 (**a**), 0.03 (**b**), 0.041 (**c**), 0.05 (**d**) and 0.08 (**e**). The best tangential focus is image **c)**. Labels *u*, *l* and c refer to the intersection of the image plane with the reflected upper rim ray, lower rim ray and central ray respectively.

To find the intersection point of the reflected upper and lower rim rays (Figure 3.36) it is necessary to equalise the vector line equations for the two rays hence

(3.97) $$(0, y_{plt}, 0) + \lambda_l [0, M'_{lt}, N'_{lt}] = (0, y_{put}, 0) + \lambda_u [0, M'_{ut}, N'_{ut}].$$

This is only applied to the meridional plane therefore the x components of points and directions are zero since the object point is in the 90° semi-meridian. Once again the origin of the axis system was taken to be the centre of the pupil for simplification. The intersection of the upper and lower rim rays with the pupil plane may not be at a pupil edge in cases of vignetting therefore these intersections were referred as y_{put} and y_{plt} instead of $+PD/2$ and $-PD/2$. Equation (3.97) represents a system of two equations from which the values of parameters λ_l and λ_u can be calculated. Either λ value can then be replaced in the z value for one of the vector line equations, for instance λ_l resulting in $z_F=\lambda_l N'_{lt}$. For the axes system centred at the pupil, it is also true that $z_F=wd+s_{parax}+DF$ from which the value of DF can be shown to be given by

(3.98) $$DF = \frac{y_{plt} - y_{put}}{\frac{N'_{lt}}{N'_{ut}} M'_{ut} - M'_{lt}} N'_{lt} - wd - s_{parax}.$$

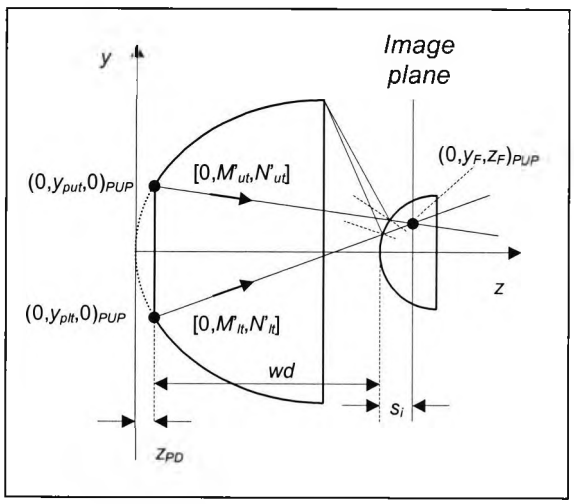

Figure 3.36 - Tangential focus for a centred surface corresponds to the intersection of the upper and lower reflected rim rays.

The previous procedure was developed to find the best tangential focus for a single ring (in practice just for one semi-meridian due to the rotational symmetry).

However the object is a set of concentric rings and hence each ring will have its best tangential focus at different positions. This phenomenon is a well known aberration known as field curvature. To determine the best focus for a set of rings the best tangential focus position for each ring was determined. It was considered that the best position for the image plane would be located somewhere along the range determined. The image plane was then moved along that range in 1μm intervals and the meridional blurs for each one of the image rings in the 90° semi-meridian added. The best focus was considered to be at the position for which the sum of the meridional blurs had a minimum value. Decreasing the step interval from 1μm will increase accuracy but at the cost of an increase in execution time. The selected interval seemed to be adequate since real instruments won't be able to move in smaller intervals.

3.12.3 Best focus for a non-centred reflecting surface

When the reflected surface is tilted and/or decentred, in general there won't be a meridional plane and hence there won't be a minimum meridional blur as specified for the centred surface. However the image of a circular object ring will still be a ring although not circular. For a ring to be considered in focus it should be as thin as possible measured radially in relation to the image ring centroid. The analysis was therefore applied in relation to the central reference point of the ring images (o_I), with radial blur denoted as b_{rad}. The distance from a point in the image $(x_F,y_F)_{GLB}$ to o_I when both are expressed in the global axis system, is given by

(3.99) $$d_{oI} = \sqrt{(x_F + o_{Ix})^2 + (y_F - o_{Iy})^2}\ .$$

If d_{oI} is calculated for all points of an image of a single object point a minimum and maximum value can be determined. The radial blur b_{rad} will be the difference between these two values. Figure 3.37 justifies the use of all points in the image to calculate the blur as opposed to using the points in image semi-meridian σ that contains point *c* corresponding to the central ray. Figure a) illustrates the image of

a single object point in a tilted and decentred surface. In such a case there is a lack of symmetry in the image and it can be seen that the points closer and further away from o_I are not in image semi-meridian σ. However the image ring is formed by summing the images from an infinite number of object points across the object ring. Therefore the image of adjacent object points with central rays striking at semi-meridians σ_1 and σ_2 will have their points of maximum and minimum distances respectively on semi-meridian σ. These angles are obviously very small hence images can be considered equal.

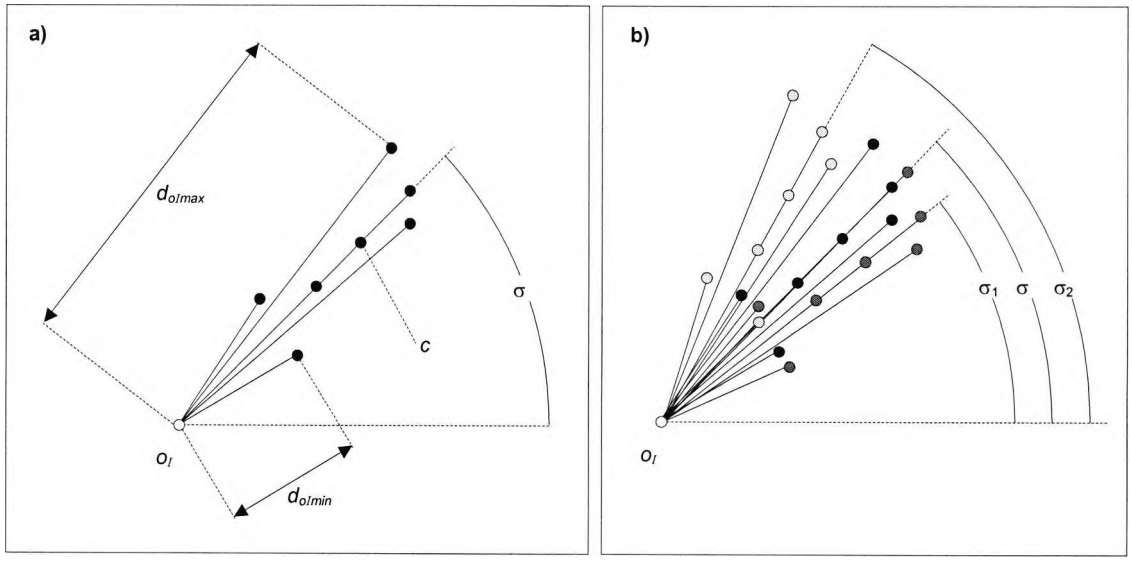

Figure 3.37 – a) The image of a single object point reflected in a tilted and decentred surface is represented (black dots) with low ray density. There is a lack of symmetry and the points closer and further away from o_I are not in the image semi-meridian σ (point *c* corresponds to the central ray). **b)** The effect of the images from adjacent object points is to place the maximum and minimum distance points aligned with semi-meridian σ. It is obvious that the images are grossly exaggerated in order to provide an explanation.

It should be noted that for a centred reflecting surface this problem is not an issue: Figure 3.35 demonstrates that the maximum and minimum distance points for any image are only located in the meridional plane that also contains the central ray intersection.

The best focus for a single point will correspond to the image plane position, *DF* (Figure 3.34 b), for which the radial blur b_{rad} will have a minimum value. An iterative process was developed to find the best focus. Each iteration of the new procedure uses an equal step approach between two limits and in the subsequent iteration the limits and the step are refined. The limits for the image plane position at each iteration will be labelled DF_{min} and DF_{max}, and the plane will move in constant steps in one iteration. The best image plane position for the typical reflecting surfaces used in this research will never reach 10mm from the vertex, since at that point a large blur will occur. It is also known that for a convex mirror the image is always located to the right of the vertex. Due to these factors the first iteration used DF_{min}=0mm and DF_{max}=10mm with steps k=1mm. The image plane will start moving from the minimum position in 1 mm steps and at each position the radial blur is calculated. The blur will start to decrease to a minimum after which it increases (Figure 3.38 a) meaning that the best focus position has been passed. This position DF_n will be taken as the maximum limit for the next iteration. To ensure the bracketing of the best focus the minimum position should be taken as DF_n-2k instead of DF_n-k. This is best explained by analysis of Figure 3.39 a) which shows that the position of the image plane for the minimum radial blur determined in the present iteration may have passed the best focus.

For the next iteration the image plane will be moved, within the limits specified in the previous iteration, in steps of k/2 (Figure b). New iterations will be executed until step k is smaller than 1μm. This was found to be a good limit since smaller steps may have no influence on the radial blur invalidating the procedure.

If the best focus for all the object rings is being determined the procedure is very similar. In this case, for each image plane position the radial blur for the image of each object point is calculated and an average is calculated. This average is calculated by adding all the radial blurs and dividing by the number of images.

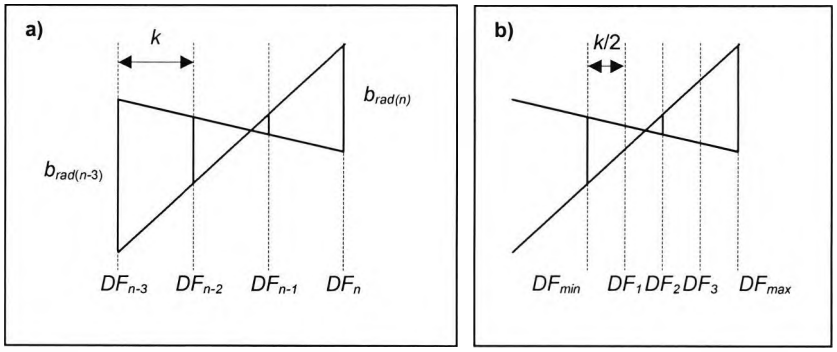

Figure 3.38 - Two successive iterations of the focus procedure. **a)** The image plane is moved in steps of *k*. The radial blur at each image plane position starts decreasing and then a point is reached in which the blur increases. This means that the best focus has been passed and the present image plane position will be the maximum limit for the next iteration. It can be seen in the figure that the minimum limit should be DF_n-2*k* rather than DF_n-*k* that way the best focus will be between the new limits. **b)** The next iteration for which the image plane will be moved between the two specified limits in steps of *k*/2.

3.13 Image relative irradiance

A on-screen display of a Spot diagram resulting from ordinary ray tracing, represents the geometrical distribution of light in the real image and does not correctly indicate irradiance variations. If the ray density is increased enough the image will be a black spot in the screen. Figure 3.39 illustrates this point in which an image from the same object point is traced with 5 (a), 20 (b) and 200 rays density (c). With 20 rays the geometrical distribution of light in the image is already apparent and it can be observed that some parts of the image will have higher irradiance than others.

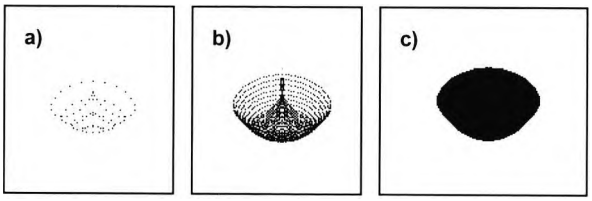

Figure 3.39 - Image of an object point using a ray density of 5 (**a**), 20 (**b**) and 200 rays (**c**).

To take into account the irradiance variations across the image a relation with the screen display was established since the image will be represented by pixels on screen. An array was used that matched the pixels on screen. A computer can usually display 256 levels of grey from 0 (black) to 255 (white). Taking this property into account all the elements of the array were initialised with 255 and then, as the image was traced, each time a ray struck a particular pixel on the screen the corresponding array element data was decremented by one unit. When the ray tracing procedure was concluded each array position contained the grey level of the corresponding screen pixel, which is a measure of the number of times that that point was hit by traced rays. The general principle developed is simple but its implementation is complex. It is also much simpler to implement the process for a centred reflecting surface, where there is image symmetry about the meridional plane, than for a non-centred surface.

If a display on the screen wasn't desired it would be much simpler to work with the real dimensions of the image, defining equal areas in the image plane and accounting the number of rays falling in each area.

3.13.1 Image display on screen

This section is necessary since the image on the screen is going to determine the number of elements in the array that controls the image irradiance. The screen represents a part of the image plane. The screen axis system in almost all computers has its origin located at the top left of the screen. The *x* axis positive direction is to the right and the *y* axis positive direction is down (Figure 3.40). Screen coordinates are integer numbers since they represent pixels. All the parameters related to screen coordinates are going to have the suffix *px* for pixel. The magnification of the display is controlled by the scaling factor *MMPX* indicating how many pixels will correspond to 1mm.

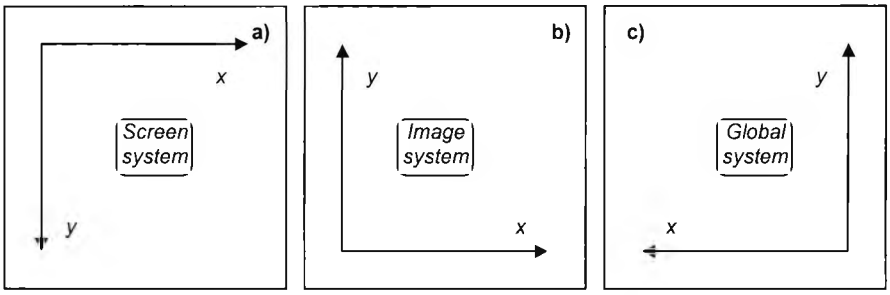

Figure 3.40 – Relationship between the *xy* direction of the several system of axis used. They are all presented from the examiner's point of view.

Equation (3.95) represents the position of an image point (x_F,y_F) on the image plane in relation to the global system. The position of the corresponding point on screen coordinates (x_{px},y_{px}) with magnification *MMPX* is

(3.100) $$x_{px} = o_{pxx} - MMPX\ x_F$$

(3.101) $$y_{px} = o_{pxy} - MMPX\ y_F\ ,$$

where parameters o_{pxx} and o_{pxy} represent the position of the global system origin in screen coordinates. The previous equations return real numbers for x_{px} and y_{px} that must be rounded in order to provide the integer values corresponding to screen pixels. To keep the image of the selected object point on screen at all times the intersection of the central ray with the image plane was always represented by the same pixel on screen. In screen coordinates this point will have coordinates (x_{pxc},y_{pxc})=(350,195) corresponding to (x_{Fc},y_{Fc}) in the global system. This position on the screen was selected based on a low resolution screen that allowed a good image magnification and still left enough room to present more data. If the coordinates of the intersection of the central ray with the image plane and the desired position on the screen are known, then if replaced in equations(3.100) and (3.101) o_{pxx} and o_{pxy} can be calculated by

(3.102) $$o_{pxx} = x_{pxc} + MMPX\ x_{Fc}$$

(3.103) $$o_{pxy} = y_{pxc} + MMPX\ y_{Fc}.$$

These equations can be replaced in equations (3.100) and (3.101) respectively yielding

(3.104) $$x_{px} = x_{pxc} + MMPX\left(x_{Fc} - x_F\right)$$

(3.105) $$y_{px} = y_{pxc} + MMPX\left(y_{Fc} - y_F\right).$$

Since screen coordinates are integer numbers the previous equations have to be rounded to obtain the final value. Due to this operation it is not possible to revert to the original point on global system coordinates (x_F,y_F) unless that point directly produced integer values in the previous equations without the need for rounding.

Using this process the desired image will always be on the screen although parts of it may lie outside if the magnification is too large. This problem will be addressed in the next section.

3.13.2 Image magnification for a centred reflecting surface

Due to rotational symmetry, the image section in the meridional plane contains the image points nearest and furthest from the videokeratoscope axis. This section is going to be used to determine the ring height therefore it should have an adequate dimension on screen to allow a proper analysis. It was stipulated that approximately 50 pixels would provide an adequate dimension of the image section on screen. Since all the calculations so far have been done for an object point in the 90 degrees semi-meridian those 50 pixels will correspond to the approximate vertical dimension of the image on screen. The image is initially traced with a ray density of 20 rays which allows an approximate estimate of its dimensions. The radial blur b_{rad} in the vertical semi-meridian (vertical dimension of the image) is calculated and is used to determine the magnification by equation

(3.106) $$MMPX = \frac{50}{b_{rad}},$$

This procedure will provide an adequate vertical fit of the image on screen. However this magnification may cause the image to extend outside the screen horizontally (Figure 3.41 a). To prevent this a limit must be established. Since the horizontal dimensions are irrelevant for the irradiance calculation this limits were established solely on the basis of an horizontal screen fit.

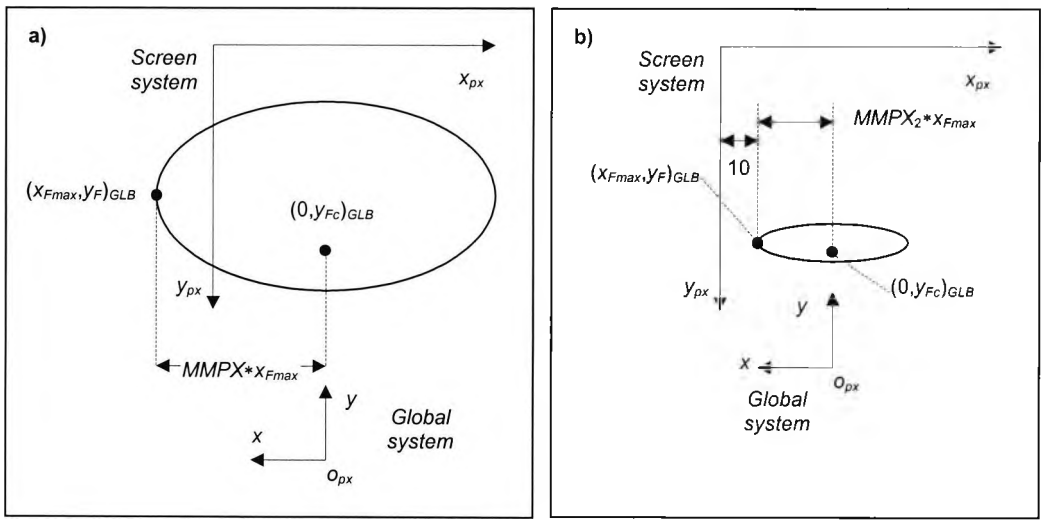

Figure 3.41 – Procedure to decrease the magnification to fit the image on screen and still leave around 10 pixels tolerance from the left screen limit. Note that the screen point corresponding to the central ray remains unchanged, it is the screen point corresponding to the global system origin o_{px} that changes to make that possible. The coordinate x_{Fmax} is the maximum positive value of the x coordinate, for that particular image, measured in the global system.

It can be seen in Figure 3.41 b) that in order for the image to fit the screen with some tolerance (10 pixels were considered) the condition $o_{pxx}=10+MMPX*x_{Fmax}$ must be met. Solving this expression for *MMPX* yields

(3.107) $$MMPX = \frac{o_{pxx} - 10}{x_{F\max}}.$$

In summary equation (3.106) is applied and then if the image extends outside the screen limits, equation(3.107) is used. In these conditions the last equation corresponds to a smaller value for *MMPX*.

3.13.3 Transforming screen coordinates to array elements for a centred reflecting surface.

As stated in the beginning of section 3.13 the array elements correspond to pixels on the screen. Each array element keeps the grey level of the corresponding screen point. However to save memory another unidimensional array was used to store the radial irradiance variation in the 90 degrees semi-meridian which is the one to be analysed. The position of the point corresponding to the central ray was considered to be at the centre of the array. The worst case that can happen is for the best tangential focus (Figure 3.35 c) in which the central ray point is one limit of the image. This will make the 50 pixels stipulated for the image vertical length to extend up from the central point. While the best case is a total blur like Figure a) for which the central point is at the middle of the image so its approximately 25 pixels to each side. To account for the worst case an array of 121 elements was used. The array elements will range from 0 to 120 with the central point located at position 60. This will allow for more than 50 pixels to extend either side of the central ray point, which includes a tolerance. For the radial section in the 90 degrees semi-meridian, position 60 of the array has to correspond to the vertical position of the central ray point on screen (y_{pxc}), hence the relation between a screen point vertical coordinate y_{px} and array position M is

(3.108) $$M = y_{px} - y_{pxc} + 60.$$

It should be noted that the array elements increase downwards as the y coordinate on the screen system.

3.13.4 Image magnification for a non-centred reflecting surface

For a non-centred reflecting surface there is no symmetry of any kind in the image hence each semi-meridian is a separate case. The only exception is for an object point in the same meridian where a tilt and/or decentration has been applied. Object points in that meridian will have images symmetrical in relation to the meridional plane. Outside that meridian a meridional plane cannot be defined thus the image will have no symmetry.

Due to the variability of the object point position and great variability of the geometrical distribution of light across the image a square bidimensional array should be used to keep the image irradiance. This is done to try to avoid favouring a particular direction. However this would only be possible if the array was circular. A square array ends up favouring the diagonal directions, nevertheless this shape was considered superior to a rectangle.

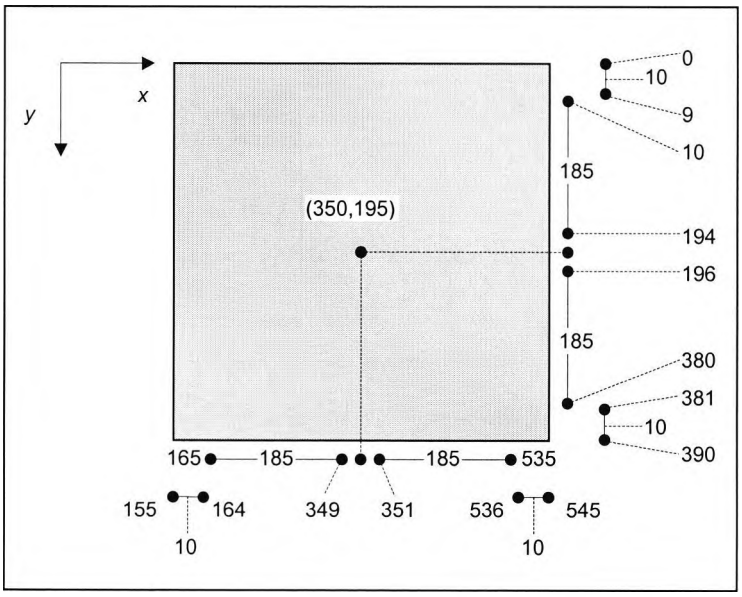

Figure 3.42 - Screen area used to represent the image of an object point reflected in a non-centred reflecting surface. It is a square area centred at pixel (350,195) extending 195 pixels for each side. The useful area will extend 185 pixels for each side allowing a 10 pixel tolerance on each side as well. Labels adjacent to points in the figure are *x* or *y* screen coordinates (pixels) while labels in the middle of line segments represent their length in pixels.

Since the point on screen chosen to represent the intersection of the central ray has coordinates (x_{pxc},y_{pxc})=(350,195), it was also selected to be the central point of the square image area (Figure 3.42). Therefore the area will extend 195 pixels each side of the central point (exclusive). A 10 pixel tolerance from each side of the square was allowed as was considered appropriate for the centred reflecting surface. This tolerance was sufficient in all examples tested, therefore the useful area will extend 185 pixels for each side of the central point.

In order for the image to fit the designated useful screen area the magnification parameter *MMPX* must be limited. If the limiting *x* and *y* coordinates of the image in the global system are considered, then the *MMPX* limits can be calculated in order for those coordinates to fall inside the useful screen area (Figure 3.43).

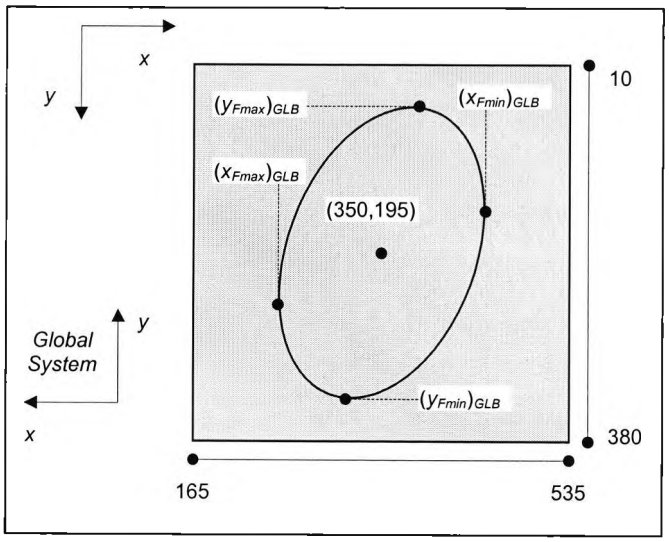

Figure 3.43 – Image fitted to the useful screen area with *x* pixels ranging from 165 to 535 and *y* pixels from 10 to 380. The limiting *x* and *y* coordinates of the image in the global system are also presented. The magnification parameter *MMPX* must be limited in order for all the limiting *x* and *y* image coordinates in the global system to fall inside the useful screen area.

Equations (3.104) and (3.105) represent the x_{px} and y_{px} screen coordinates corresponding to global system coordinates x_F and y_F respectively. It can be said that the former coordinates are a function of the latter, that is, $x_{px}(x_F)$ and $y_{px}(y_F)$ in mathematical notation. Using this notation it can be seen by analysis of the last figure that for the image to fall inside the useful screen area (185 pixels in each direction from the central ray) the conditions $x_{px}(x_{Fmax})\geq 165$, $x_{px}(x_{Fmin})\leq 535$, $y_{px}(y_{Fmax})\geq 10$ and $y_{px}(y_{Fmin})\leq 380$ must be met simultaneously. Replacing the values in the respective equations ((3.104) for x_{px} and (3.105) for y_{px}) and bearing in mind that $(x_{pxc},y_{pxc})=(350,195)$ the conditions become

(3.109) $$MMPX\left(x_{Fc}-x_{F\max}\right)\geq -185,$$

(3.110) $$MMPX\left(x_{Fc}-x_{F\min}\right)\leq 185,$$

(3.111) $$MMPX\left(y_{Fc}-y_{F\max}\right)\geq -185,$$

(3.112) $$MMPX\left(y_{Fc}-y_{F\min}\right)\leq 185.$$

The coordinates of the central ray point on the global system (x_{Fc},y_{Fc}) must be within the image limiting coordinates $x_{Fmin}\leq x_{Fc}\leq x_{Fmax}$ and $y_{Fmin}\leq y_{Fc}\leq y_{Fmax}$ therefore the conditions in equations (3.109) to (3.112) become

(3.113) $$MMPX\leq\frac{185}{x_{F\max}-x_{Fc}},$$

(3.114) $$MMPX\leq\frac{185}{x_{Fc}-x_{F\min}},$$

(3.115) $$MMPX\leq\frac{185}{y_{F\max}-y_{Fc}},$$

(3.116) $$MMPX\leq\frac{185}{y_{Fc}-y_{F\min}}.$$

It is obvious that these conditions are not valid if $x_{Fc}=x_{Fmin}$ or $y_{Fc}=y_{Fmax}$ which means that any *MMPX* value will fulfil the condition since that particular coordinate will always be at the centre of the designated screen area. Since all four conditions must be met the conjunction corresponds to the smallest value of *MMPX*, which must be rounded down to be an integer. If this value of *MMPX* were to be used the process would be very simple, the problem is that this magnification may be too big for the necessary image section to analyse. A larger image area will cause a greater dispersion of the incident energy on it, requiring a bigger ray density. This will increase computation time exponentially. To avoid this problem it was stipulated that 50 pixels in the analysis direction would be an adequate screen dimension for the image in agreement with what was done for the centred reflecting surface. However, for the centred surface, the image section analysed was in the 90 degrees semi-meridian whereas for a non-centred reflecting surface it is only known that the image section to be analysed shouldn't be too far away from the object semi-meridian.

It is possible that every line joining the videokeratoscope axis to an image point is outside of the object semi-meridian σ_o (Figure 3.44 a). This can also happen if the image point semi-meridians are measured in relation to o_I (Figure b). This implies that the object point semi-meridian (σ_o) cannot be used to determine the image size in the direction in which the image is going to be analysed since there may be no object points in that direction. However the image point corresponding to the central ray is always known thus the semi-meridian σ_c in relation to o_I was chosen to calculate the image size. In section 3.14.2 it will be shown that this semi-meridian may not be the direction of analysis either. Unfortunately in order to determine the direction of analysis an image size must be selected and cannot be changed, therefore a starting point must be established.

Calculating the image size in the specified direction is not straightforward since only the dimension across the intersection of the line that marks the direction

(direction marker) with the image is required (b_{DM}) and not the total image dimension in that direction (b_{DMTot}) (Figure 3.45).

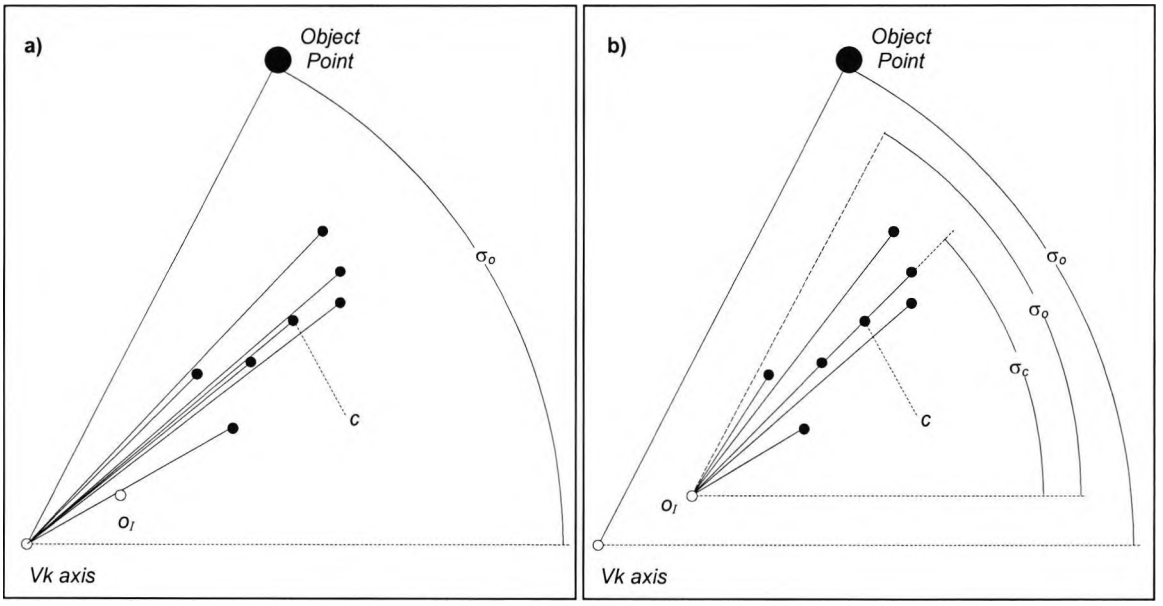

Figure 3.44 - The videokeratoscope axis is perpendicular to the paper plane, intersecting it at the white dot. The other white dot is o_I the centre of the fixation light image or the centre of the ring mire image. The small dark dots represent the image of the object point presented (large dark dot) with a low ray density formed by a non-centred reflecting surface. In this case it is possible that no point in the image falls in the object semi-meridian σ_o. This can happen whether the image points semi-meridians are measured in relation to the videokeratoscope axis (**a**) or in relation to o_I (**b**).

An approximation to b_{DM} was calculated from the positions of the image points closer to the direction marker. An image point was considered to be close to the direction marker if its distance to the marker was smaller or equal to the average distance of all image points to the marker. It is only possible to calculate an approximation to b_{DM} since the only point in the image that lies exactly on the direction marker is the point corresponding to the central ray (Figure 3.46). This point was used to calculate the marker.

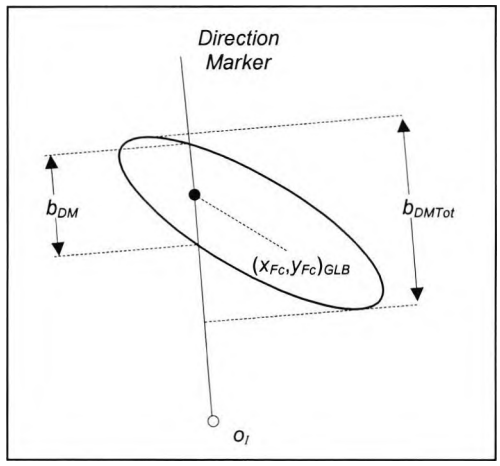

Figure 3.45 - Image dimensions along the direction marker. This marker is the line passing through o_I and the central ray position on the image plane (x_{Fc},y_{Fc}). The total image dimension along the direction marker b_{DMTot} is not of any interest. The dimension desired is the line segment that intersects the image b_{DM}.

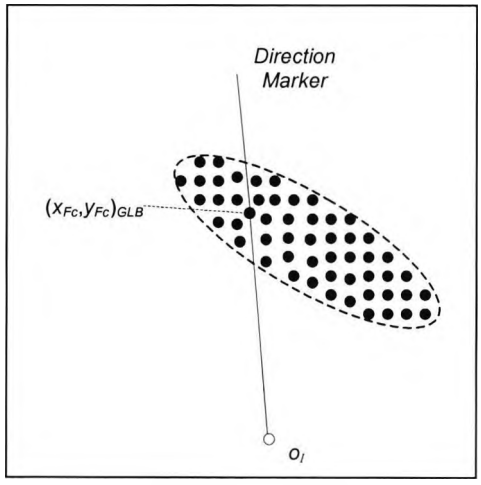

Figure 3.46 – The image is a set of points disposed in a particular arrangement. If the ray density is not very high there will only be a point in the image that will coincide with the direction marker. That is the point corresponding to the central ray, which was used to calculate the marker.

In order to calculate b_{DM} it is necessary to determine the angle α_{DM} between the direction marker and the global system x axis (Figure 3.47). Knowing that the

marker is a line joining the image origin o_I with the intersection of the central ray with the image plane, angle α_{DM} is calculated by

(3.117) $$\alpha_{DM} = \arctan\left(\frac{y_{Fc} - o_{Iy}}{x_{Fc} + o_{Ix}}\right).$$

The only exception is if $x_{Fc}+o_{Ix}=0$ meaning that $\alpha_{DM}=90°$. The direction corresponding to α_{DM} can be expressed by the unit vector

(3.118) $$\hat{e}_{DM} = \cos\alpha_{DM}\,\hat{i} + \sin\alpha_{DM}\,\hat{j}.$$

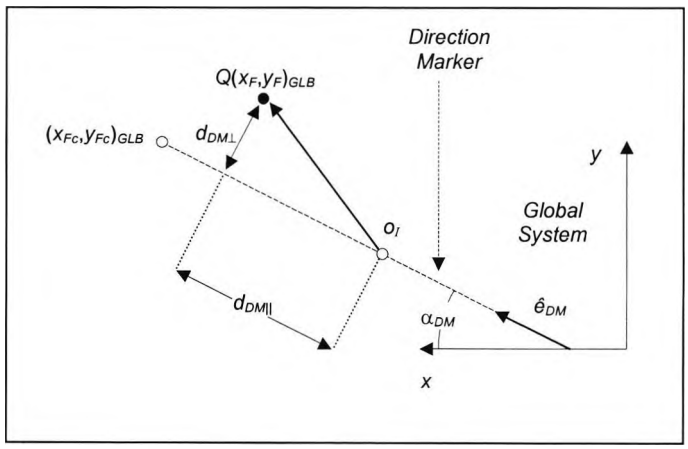

Figure 3.47 – The vector from the image origin o_I to an image point Q can be decomposed in one component perpendicular to the direction marker ($d_{DM\perp}$) and another component parallel to it ($d_{DM||}$). The perpendicular component represents the distance from the image point to the direction marker.

The vector joining the image origin o_I to a general image point Q is

(3.119) $$\overrightarrow{o_I Q} = (x_F + o_{Ix})\hat{i} + (y_F - o_{Iy})\hat{j},$$

and hence the distance from the image point Q to the direction marker is then calculated by

(3.120) $$d_{DM\perp} = \left|\overrightarrow{o_I Q} \wedge \hat{e}_{DM}\right| = \left|(x_F + o_{Ix})\sin\alpha_{DM} - (y_F - o_{Iy})\cos\alpha_{DM}\right| .$$

After the average $d_{DM\perp}$ has been calculated using all points in the image, each point is analysed again to check if its $d_{DM\perp}$ is less than or equal to the average value. In such case the parallel component (Figure 3.47) is calculated by

(3.121) $$d_{DM\|} = \overrightarrow{o_I Q} \bullet \hat{e}_{DM} .$$

Note that this value is negative when the projection of the vector $o_I Q$ in $\hat{e}_{DM}$ is in the opposite direction to $\hat{e}_{DM}$ which will correspond to an angle bigger than 90° between the two vectors. After calculating $d_{DM\|}$ for all relevant image points a maximum and minimum value can be obtained from the set. Finally the image blur is calculated by

(3.122) $$b_{DM} = d_{DM\|\max} - d_{DM\|\min} .$$

The magnification parameter *MMPX* is then calculated by equation (3.106) but using b_{DM} instead of b_{rad}. This will make b_{DM} correspond to 50 pixels on screen. However this value has to be checked against the limiting *MMPX* value calculated from equations (3.113) to (3.116). If the value corresponding to b_{DM} is larger than the limiting value then the latter must be used, otherwise the former will prevail. It should be noted that the calculated b_{DM} is not really the one represented in Figure 3.45 since it can only be calculated accurately using a very high ray density. It is just an approximation that will be better than b_{DMTot} when used to calculate *MMPX*.

3.13.5 Transforming screen coordinates to array elements for a non-centred reflecting surface.

Due to the lack of image symmetry the array to be used will have to match the entire screen area designated for the image, including the tolerances (Figure 3.42). It should be recalled that the tolerances were used since the image magnification was calculated with a much lower ray density than that used to calculate the final image. The final image will be slightly bigger in the global system, so that the magnified image will fall outside the boundaries designated by the useful screen area. The total square area on screen, including tolerances, to fit the image was 391 x 391 pixels side therefore the array to use will be bidimensional with an equal number of rows and columns ranging from 0 to 390, totalling 391x391 elements. The row and column numbers will increase in the same pattern as screen coordinates. Row numbers (corresponding to y_{px}) increase downwards and column numbers (corresponding to x_{px}) increase to the right. The row number is given by y_{px} (Figure 3.42), while the column number has to be 0 when x_{px}=155, hence this quantity has to be subtracted from x_{px} in order to get the column number. In summary the array position (*row*,*col*) is

(3.123) $$row = y_{px}$$

(3.124) $$col = x_{px} - 155.$$

Parameters x_{px} and y_{px} are the screen coordinates of an image point calculated from equations (3.104) and (3.105) respectively.

3.13.6 Automatic ray density calculation

As stated previously each time a traced ray falls on a particular screen point the corresponding array element is decremented starting from 255. If the number stored in an array element [row, col] is denoted by *B* a black pixel will be placed in the corresponding screen position whereas if *B*=0 and a white pixel will be placed

on the white screen if B=255. In the latter case it means that there is no light from the image at that particular screen position. It is obvious that if B<0 the corresponding screen point cannot be darker than black. The aim of the automatic ray density calculation is to find a value for the parameter R_0 (radius of the central area of the equal density pattern of rays Figure 3.23) for which the minimum B value found is 0.

An iterative procedure was developed to calculate the optimum R_0 value which was divided into two stages. The first consists in bracketing R_0 between a value that provides a positive minimum B for the array elements and another providing a negative minimum B. The second stage uses the bracketing to get to an R_0 value that results in a minimum B of zero. The R_0 value corresponding to a positive minimum B labelled $B^{<+}$ will be referred to as $R_0^{B<+}$. The second R_0 and negative minimum B will be referred to as $R_0^{B>-}$ and $B^{>-}$ respectively.

The first iteration starts with an initial R_0 value for a ray density of 20 (equation (3.83)). This value was found to be adequate by experimentation. After concluding the ray tracing process all the array elements are analysed and the minimum B value determined. If the minimum B is positive (which generally happens since 20 rays is a low ray density) then $B^{<+}$ is set to that value and $R_0^{B<+}$ set to the initial R_0. This means that the ray density used is low and hence needs to be increased. The program then sets R_0=R_0/2 and starts a new iteration (note that decreasing R_0 will increase the ray density). The iterations will continue until a value R_0 is found for which the minimum B is negative. This means that the last R_0 was too small (ray density too high) and $B^{>-}$ is set to the negative minimum B and $R_0^{B>-}$ will be the R_0 used for this iteration. At this point the bracketing procedure will be completed. This process is illustrated for an array with 4 elements in Figure 3.48. Note that when R_0 is halved the procedure illustrated in Figure 3.24 is used for the pencil of rays sent from an object point.

Start		Iteration 1 R_{01}		Iteration 2 $R_{02}=R_{01}/2$		Iteration 3 $R_{03}=R_{02}/2$		Iteration 4 $R_{04}=R_{03}/2$		Iteration 5 $R_{05}=R_{04}/2$	
255	255	255	245	255	225	255	150	255	32	255	-90
255	255	250	252	247	250	175	190	110	100	17	0
		B_{min} 245		B_{min} 225		B_{min} 150		B_{min} 32		B_{min} -90	
		$B^{<+}=245$		$B^{<+}=225$		$B^{<+}=150$		$B^{<+}=32$		$B^{>-}=-90$	
		$R_0^{B<+}=R_{01}$		$R_0^{B<+}=R_{02}$		$R_0^{B<+}=R_{03}$		$R_0^{B<+}=R_{04}$		$R_0^{B>-}=R_{05}$	

Figure 3.48 - First step of the Iterative procedure to bracket R_0 between a value that provides a negative minimum B and another that results in a positive minimum B. The present example is for an array with 4 elements where the bracketing has been achieved in the 5th iteration. The initial ray density was too low and had to be increased by decreasing R_0.

If on the other hand when using the initial R_0 the minimum B value is negative, it means that a ray density of 20 is too high. It is then necessary to decrease it. In this case it is $B^{>-}$ that is set to the minimum B and $R_0^{B>-}$ to the initial R_0. The program then sets $R_0=2R_0$ and a new iteration is started. However the array must be reinitialised to 255 after each iteration since the ray density is decreasing. The iterations will continue until a value R_0 is found for which the minimum B is positive. This means that the last R_0 was too big (ray density too low) and $B^{<+}$ is set to the positive minimum B and $R_0^{B>-}$ will be the R_0 used for this iteration. At this point the bracketing procedure will be completed. This process is illustrated in Figure 3.49.

The second step of the automatic ray density procedure is a refinement to get to the optimum R_0 value. It uses the established bracketing limits in the equation

(3.125) $$R_0 = R_0^{B<+} - \frac{R_0^{B<+} - R_0^{B>-}}{1 - \frac{B^{>-}}{B^{<+}}}.$$

Start		Iteration 1 R_{01}		Iteration 2 $R_{02}=R_{01}$x2		Iteration 3 $R_{03}=R_{02}$x2		Iteration 4 $R_{04}=R_{03}$x2		Iteration 5 $R_{05}=R_{04}$x2	
255	255	255	-99	255	-80	255	-40	255	-8	255	22
255	255	-45	-30	-32	-20	-10	0	30	45	50	70
		B_{min} -99		B_{min} -80		B_{min} -40		B_{min} -8		B_{min} 22	
		$B^{>-}$=-99		$B^{>-}$=-80		$B^{>-}$=-40		$B^{>-}$=-8		$B^{<+}$=22	
		$R_0^{B>-}=R_{01}$		$R_0^{B>-}=R_{02}$		$R_0^{B>-}=R_{03}$		$R_0^{B>-}=R_{04}$		$R_0^{B<+}=R_{05}$	

Figure 3.49 - First step of the Iterative procedure to bracket R_0 between a value that provides a negative minimum B and another that results in a positive minimum B. The present example is for an array with 4 elements where the bracketing has been achieved in the 5th iteration. The initial ray density was too high and had to be decreased by increasing R_0.

To analyse the effect of this equation it should be remembered that $R_0^{B<+} > R_0^{B>-}$ and that $B^{>-}<0$ and $B^{<+}>0$. Therefore the quotient in the equation is positive meaning that R_0 is going to be smaller than $R_0^{B<+}$. The subtracted value will be a fraction of the difference of the R_0 bracket limits. If $|B^{>-}|=B^{<+}$ the denominator is 2, if $|B^{>-}|>B^{<+}$ it's bigger than 2 and if $|B^{>-}|<B^{<+}$ it's smaller than 2 but bigger than 1. For each one of these cases the new value for R_0 will be respectively the average of the two bracket limits, closer to $R_0^{B<+}$ and closer to $R_0^{B>-}$.

After completing the ray tracing procedure for this value of R_0 the array is again analysed and the minimum B value taken. If $B_{min}<0$ it will be a better estimate for $B^{>-}$ and the present R_0 will then become $R_0^{B>-}$. If $B_{min}>0$ it will be a better estimate for $B^{<+}$ and the present R_0 will become $R_0^{B<+}$. The array is then reinitialised to 255 and the process repeated until a value of R_0 is found for which $B_{min}=0\pm1$. This procedure is illustrated in Figure 3.50 starting from the last iteration in Figure 3.48.

It was found by experimentation that at a given point in the procedure, although R_0 is changed, the minimum B tends to be found in the same array element. This means that the image irradiance variation in one semi-meridian will be proportional

to the image irradiance variation in the same semi-meridian for the ideal ray density. For a centred reflecting surface, where the ray tracing is fast, the procedure was stopped when $B_{min}=0\pm1$. This measure was adopted since it was found that when B_{min} is one unit away from 0 the procedure needed several iterations to take it to 0 although the ring edge would be detected at the same image point. For a non-centred reflecting surface, where the ray tracing is very slow, the procedure was stopped at the bracketing point by taking the last R_0 before the bracketing. However if only one object point is of interest the user is allowed to select if the procedure should continue beyond the bracketing point.

Iteration 5		*Iteration* 6		*Iteration* 7		*Iteration* 8	
$R_{05}=R_{04}/2$		R_{06}		R_{07}		R_{08}	
255	-90	255	20	255	-10	255	0
17	0	85	80	60	50	30	25
B_{min} -90		B_{min} 20		B_{min} -10		B_{min} 0	
$B^{>-}=-90$		$B^{>-}=-90$		$B^{>-}=-10$		$R_0=R_{08}$	
$B^{<+}=32$		$B^{<+}=20$		$B^{<+}=20$		***END***	
$R_0^{B>-}=R_{05}$		$R_0^{B>-}=R_{05}$		$R_0^{B>-}=R_{07}$			
$R_0^{B<+}=R_{04}$		$R_0^{B<+}=R_{06}$		$R_0^{B<+}=R_{06}$			

Figure 3.50 - Second stage of the iterative procedure to find a value of R_0 for which $Bmin=0$. Iteration 5 refers to the last first stage iteration. The values in grey background are the ones that were not changed in a particular iteration.

3.14 Ring edge detection

3.14.1 Centred reflecting surface

In this case the image section for analysis will be in the 90° semi-meridian for simplicity. However due to rotational symmetry the image irradiance variation will be the same for all semi-meridians. At this point the array representing the image irradiance has been calculated. This array is unidimensional with 121 elements (see section 3.13.3) containing values (referred to as B) ranging from -1 to 255.

These values are inversely related to the irradiance in an image point, that is, a lower B corresponds to a higher irradiance. The irradiance I corresponding to an array element is therefore I=255-B. It should also be recalled that the array elements increase with the y screen coordinates.

It was assumed that a ring edge detection algorithm uses a value $I=0.5I_{max}$ as reference. (I_{max} is the maximum irradiance in the radial section, corresponding to the minimum B of all array elements). However the program user is allowed to change the fraction of I_{max} from 0.5. The irradiance stored in the array elements is a discrete set of points, hence it is most likely that no I will be equal to $0.5I_{max}$. To account for this problem a procedure was developed treating inner and outer ring edges of an image ring differently. The edges are counted from the videokeratoscope axis (Figure 3.51 a and b).

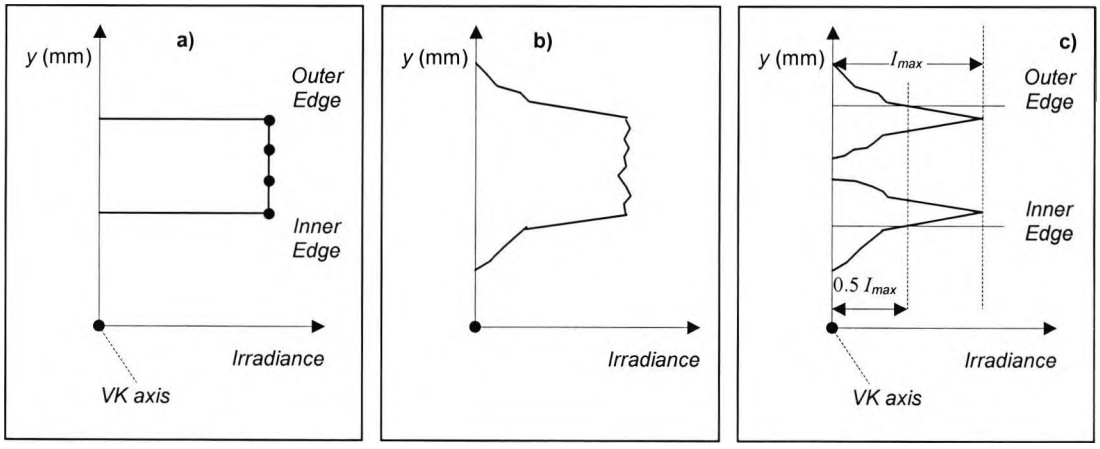

Figure 3.51 – a) Irradiance of the vertical radial section of an object ring. **b)** Example of the image irradiance of the radial section sampled by the CCD detector. However only the images of the edges of the object ring were considered. An example of the irradiance of these points is represented in **c)**. The image ring edge detection uses an irradiance value of $0.5I_{max}$ as a reference. If an inner edge of a ring is being detected the smallest y for which $I \geq 0.5I_{max}$ is considered to be the edge. If an outer edge is being detected the larger y for which $I \geq 0.5I_{max}$ is considered to be the edge. The y values represented are in the global system.

Only the object points located at the edges of the vertical radial section of an object ring were accounted for. The irradiances of the images of all other object points between the edges are summed inside the radial irradiance curve for the ring section (central figure), hence are not important for edge detection. If an inner edge of an image ring is being detected, the smallest y value for which $I \geq 0.5 I_{max}$ was considered (Figure c). If an outer edge of an image ring is being detected, the largest value of y for which $I \geq 0.5 I_{max}$ was considered.

However since the irradiance variation is stored in an array it is an array position that must be identified as the ring edge and then transformed into y coordinates of the global system. It should be remembered that the array positions correspond to screen coordinates, as these increase global system coordinates decrease. This means that for an inner edge, the ring edge is the largest array position for which $I \geq 0.5 I_{max}$. For an outer edge, the ring edge is the smallest array position for which $I \geq 0.5 I_{max}$. Since the array position M, considered to be the ring edge, is known, the corresponding pixel position on screen can be calculated by solving equation(3.108) for y_{px}. This screen position is finally translated to the global system y coordinate (y_F) by solving equation(3.105) for y_F.

3.14.2 Non-centred reflecting surface

Due to the lack of image symmetry a single object point cannot account for all cases on a ring. The object point may then be located at any semi-meridian and the developed model must take this into consideration. Furthermore since there is no meridional plane the image of a given object point may not lie in the same meridian as the object point. Therefore the irradiance variation on a given semi-meridian is affected by the image of several adjacent object points.

The overlapping effect of the images of several adjacent object points was simulated considering that the image of a single object point was rotated around o_I (centre of *IMG* system, see section 3.10) in both directions between the angular limits of the image described at o_I (Figure 3.52 a). As a result of the image rotation

an angular sector will be described (b). The irradiance of that sector at a distance d_{oI} from o_I was considered to be the maximum irradiance displayed by image points at the same distance in the original image.

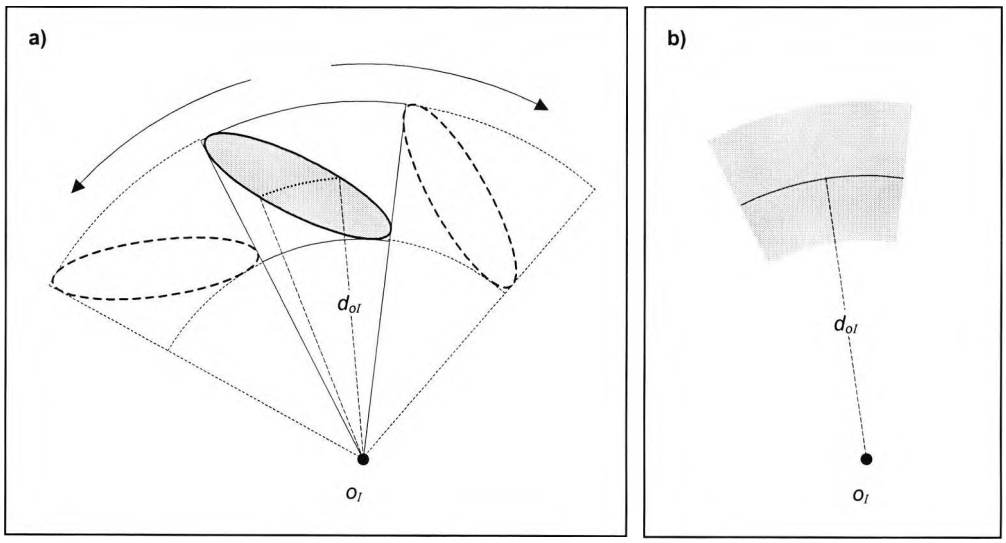

Figure 3.52 - Simulation of the summing effect of images of adjacent points on a ring edge. The image of a single object point on a ring edge (grey tilted ellipse) is rotated on both directions around o_I in order to completely cover the angular sector defined by the image limits at o_I (**a**). The resultant sector is represented in **b)**. The irradiance of this sector at a distance d_{oI} from o_I was considered to be constant and equal to the maximum irradiance displayed by the image points at the same distance on the original image. The image size is grossly exaggerated to illustrate the point.

To apply this method the array containing the irradiance of the image, generated by ray tracing, was analysed element by element and only the ones for which $I \geq 0.5 I_{max}$, were considered (see section 3.14.1). Each of the considered elements (*row*,*col*) was transformed into the corresponding screen coordinates (x_{px},y_{px}) by rearranging equations (3.123) and (3.124). The screen coordinates were then transformed to global system coordinates (x_F,y_F) by rearranging equations (3.104) and (3.105). These coordinates allow the distance to o_I (d_{oI}) to be calculated using equation(3.99).

As for the centred reflecting surface, the edge detection depends on whether the object point is in an inner or outer ring edge. For an object point on an inner edge the inner edge of the image was considered to be the image point with $I \geq 0.5 I_{max}$ closest to o_I (shortest d_{oI}). For an object point in an outer edge the outer edge in the image was considered to be the image point with $I \geq 0.5 I_{max}$ further away from o_I (longest d_{oI}). The selected value of d_{oI} will correspond to the ring mire image height on that semi-meridian.

3.15 *Reconstruction algorithms adaptation*

Several reconstruction algorithms have been described briefly in section 2.2. However in order for them to work in the computer model developed for this research they have to go through considerable transformations. Two reconstruction algorithms have been chosen for this effect, the spherical biased and the van Saarloos algorithm. The former was used due to its simplicity and availability of several research papers on the subject. The van Saarloos algorithm was selected due to several advantages over other algorithms, namely the use of an arc step approach and fewer approximations. Arc step methods are the most widely used today since they do not force the surface to fit a particular shape.

The most important adaptation to the algorithms was to make them independent of the objective lens used in the CCD camera. It was assumed that the camera optics would have a good quality, accurately representing the image reflected on the cornea. Therefore it was best to work directly with the reflected image considering only the rays that would enter the instrument pupil located in the faceplate.

3.15.1 Adaptation of the spherical biased algorithm.

Instead of the six calibrating spheres used by Rowsey and Isaac (1983) it was decided to use 10 spheres in the same interval to increase accuracy. The 10 spheres ranged from 5.5mm to 9.5mm in 0.5mm intervals. A second modification consisted in extending the calibration graph to the outer ring edges doubling the number of calibration lines and again increasing accuracy.

The calibration lines in the original algorithm resulted from a linear regression applied to the available points for a given ring edge. To increase accuracy instead of calculating a line, a linear interpolation was used between the two closest bracketing points. This approach could not be used by Rowsey and Isaac since their data was based in slightly decentred reflecting surfaces. The decentration was possibly due to poor centration control on the corneascope. This was done manually by centring the rings on a crosshair in a viewer in the instrument according to Goss (1991).

For the spherical biased algorithm the image height h is considered equal to the reflection point y coordinate. To calculate the radius of curvature at a surface point with height h in between ring mire image heights h_i and h_{i+1} in the graph, the corresponding radius of curvature R is given by

(3.126) $$R = \frac{R_{i+1} - R_i}{h_{i+1} - h_i}(h - h_{i+1}) + R_{i+1}.$$

This method can only be applied to hemi-chord heights between the minimum and maximum hemi-chords available in the graph.

The tangential radius of curvature was calculated using equation(3.16), which is only adequate for a conic curve.

3.15.2 *Adaptation of the van Saarloos algorithm*

All equations of the original algorithm had to be transformed in order to be expressed in relation to the global coordinate system (*GLB*) centred at the faceplate vertex. Only the corneal coordinates (y_i, z_i) are expressed in an axis system with origin at the corneal vertex.

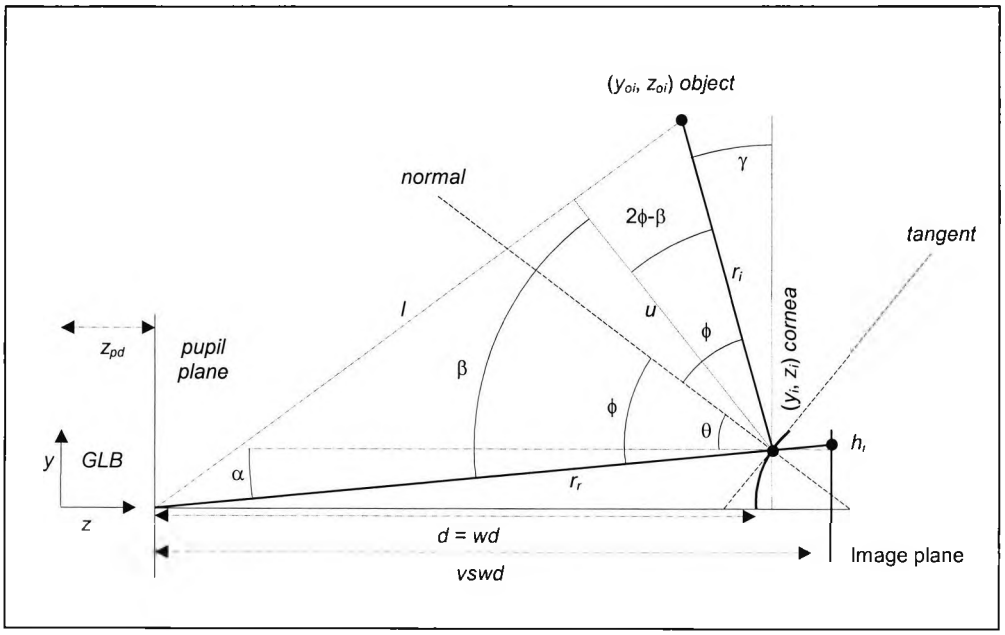

Figure 3.53 – Modified geometry for van Saarloos algorithm. A ray with origin at a general object point is reflected in the corneal surface and enters the faceplate pupil.

The angle between the reflected ray and the z-axis can be calculated from the image height h_i, measured in the image plane and the position of this plane by

(3.127) $$\tan\alpha = \frac{h_i}{vswd} = \frac{h_i}{wd + s_{parax} + DF}.$$

To understand the previous equation it should be remembered that the simulation program considers the image plane to be located at a distance *DF* from the paraxial plane position (s_{parax}). The latter is measured from the surface vertex (see section 3.12).

In the original van Saarloos algorithm the real image height (h_i) was unknown. Since the videokeratoscope will only know the image height on the CCD array (which is the reflected image imaged by the CCD camera) and the distance from the CCD camera objective to the CCD array. Angle α was calculated from these two parameters. If this approach was followed for the simulation program it would

imply using a particular CCD camera. This way the simulation would test the algorithm plus camera arrangement instead of the algorithm alone. Since the simulation calculates h_i directly this value was used to calculate α.

Considering that the image plane is the paraxial plane, the paraxial formula for a convex mirror, equation (3.92), can be used yielding

(3.128) $$\frac{2}{R} = \frac{1}{vswd - d} - \frac{1}{d - z_{oi} + z_{pd}},$$

where R is the apical radius of curvature. Notice that the original equation was multiplied by –1 in both members and that s_{PARAX} = -($vswd$-d) was considered negative according to the sign convention, since the image of a convex mirror is virtual. If the previous equation is solved for d (distance from the pupil plane to the reflecting surface vertex) a quadratic equation is obtained. There are two solutions for the equation and the correct one has a plus sign before the square root, thus

(3.129) $$d = \frac{1}{2}\left(vswd + z_{oi} - z_{pd} - R + \sqrt{(vswd - z_{oi} + z_{pd})^2 + R^2} \right).$$

To understand this choice of sign consider an object point in the pupil edge (z_{oi} = z_{pd}). Knowing that $vswd >> R$, if the solution with a negative sign before the square root was selected d would tend to zero, which would mean that the corneal vertex was coincident with the instrument pupil. Therefore the correct solution is the positive root.

Since the apical radius of curvature has its centre of curvature at the reflecting surface axis the following relations are valid:

(3.130) $$\sin\theta = \frac{y_i}{R},$$

(3.131) $$y_i = (d + z_i)\tan\alpha\,,$$

and

(3.132) $$z_i = R(1 - \cos\theta)\,.$$

Combining the three previous equations yields

(3.133) $$\sin\theta = \left(\frac{d}{R} + 1 - \cos\theta\right)\tan\alpha\,,$$

which can be solved for cos θ to give a quadratic equation with solution

(3.134) $$\cos\theta = \frac{b^2(a+1) + \sqrt{1 - b^2 a(a+2)}}{1 + b^2}\,,$$

where $a = \frac{d}{R}$ and $b = \tan\alpha$. Since α is a small angle the solution with a positive sign before the square root was selected otherwise *cos* θ would be negative, meaning θ would be bigger than 90 degrees.

From Figure 3.53 the angle between the incident ray and the surface axis (2ϕ-α), considered to be positive, can be calculated by

(3.135) $$\tan(2\phi - \alpha) = \frac{y_i - y_{oi}}{z_{oi} - z_{pd} - d - z_i}\,.$$

From the previous figure it is also straightforward to see that θ = ϕ - α, which can be rearranged to give

(3.136) $$\theta = \frac{1}{2}((2\phi - \alpha) - \alpha)$$

Combining equations (3.127), (3.130), (3.135) and (3.136) the apical radius *R* can be calculated from

(3.137) $$R = \frac{y_i}{\sin\left\{\frac{1}{2}\left[\arctan\left(\frac{y_i - y_{oi}}{z_{oi} - z_{pd} - d - z_i}\right) - \arctan\left(\frac{h_i}{vswd}\right)\right]\right\}}.$$

The iterative procedure to calculate R follows the sequence:

1. *R* = 7.8 mm
2. Equation(3.129) to estimate *d*.
3. Equation(3.134) to estimate *cos* θ.
4. Equation(3.132) to estimate z_i.
5. Equation(3.131) to estimate y_i.
6. Equation(3.137) to estimate *R*.
7. Return to step 2.

The iteration will stop when the difference of the *R* values between two successive iterations is smaller than 1nm. The first value for *R* that starts the iteration is the average corneal radius used by van Saarloos. The problem with this procedure lies in equation(3.128), the paraxial equation for spherical mirrors. This is because it considers the image plane to be the paraxial image plane when it isn't. Still a good estimate for *R* can be found.

Doss's method of considering corneal points joined by arcs was also used by van Saarloos. Figure 3.54 illustrates the geometry of this method, for which

(3.138) $$\frac{\cos\theta_i - \cos\theta_{i-1}}{\sin\theta_i - \sin\theta_{i-1}} = \frac{\frac{z_c - z_i}{R_i} - \frac{z_c - z_{i-1}}{R_i}}{\frac{y_i - y_c}{R_i} - \frac{y_{i-1} - y_c}{R_i}} = -\frac{z_i - z_{i-1}}{y_i - y_{i-1}}.$$

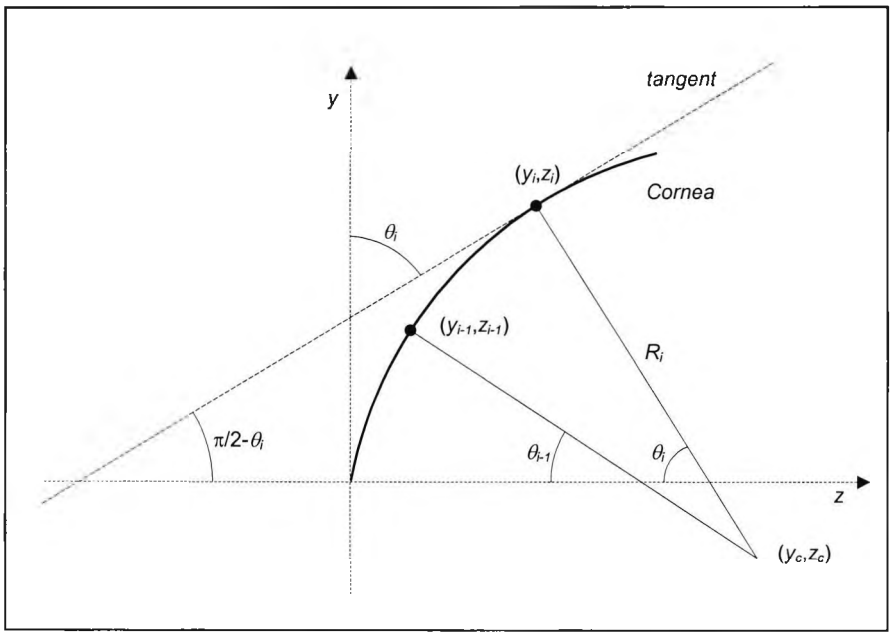

Figure 3.54 – Doss geometry for determining the next corneal point. It considers two adjacent points joined by arcs.

The corneal point (y_{i-1}, z_{i-1}) was determined in the previous iteration. Point (y_i, z_i) which is to be determined in the present iteration, is obtained by drawing an arc with radius R_i centred at (y_c, z_c).

From analysis of Figure 3.53 the following relations can be obtained:

(3.139) $$l^2 = y_{oi}^2 + (z_{oi} - z_{pd})^2 ,$$

(3.140) $$r_i^2 = (y_{oi} - y_i)^2 + (d + z_i - z_{oi} + z_{pd})^2 ,$$

(3.141) $$r_r^2 = y_i^2 + (d + z_i)^2 ,$$

(3.142) $$r_i^2 = u^2 + \left(\vec{r_i} \cdot \vec{l}\right)^2,$$

(3.143) $$r_r^2 = u^2 + \left(\vec{r_r} \cdot \vec{l}\right)^2,$$

(3.144) $$\cos(2\phi) = \cos[\beta + (2\phi - \beta)] = \cos\beta\cos(2\phi - \beta) - \sin\beta\sin(2\phi - \beta) = \frac{u}{r_r}\frac{u}{r_i} - \frac{\left(\vec{r_r} \cdot \vec{l}\right)}{r_r}\frac{\left(\vec{r_i} \cdot \vec{l}\right)}{r_i}.$$

Solving equations (3.142) and (3.143) for u^2, adding them and replacing the result in equation (3.144) angle 2ϕ can be calculated by

(3.145) $$2\phi = \arccos\left\{\frac{\left[\left(\vec{r_r} \cdot \vec{l}\right) + \left(\vec{r_i} \cdot \vec{l}\right)\right]^2 - r_r^2 - r_i^2}{-2r_r r_i}\right\} = \arccos\left(\frac{l^2 - r_r^2 - r_i^2}{-2r_r r_i}\right).$$

From analysis of Figure 3.53 another set of equations can be obtained:

(3.146) $$\theta = \frac{\pi}{2} - \phi - \gamma = \frac{\pi}{2} - \phi - \arctan\left(\frac{d + z_i - z_{oi} + z_{pd}}{y_{oi} - y_i}\right),$$

(3.147) $$y_i = r_r \sin\alpha_i,$$

(3.148) $$y_i = (R - z_i)\tan\theta.$$

The iterative procedure to determine a surface point (y_i, z_i) follows the sequence:

1. Use corneal point (y_{i-1}, z_{i-1}) and θ_{i-1} determined for the previous ring.
2. Consider θ_i as half the angle between the horizontal and the line joining the object point and centre of curvature of the apical radius given by

(3.149) $$\theta_i = \frac{1}{2}\arctan\left(\frac{y_{oi}}{d + R - z_{oi} + z_{pd}}\right).$$

3. The reflection point coordinate y_i is located at the intersection between line r_r and the surface normal at that point (Figure 3.53). Angle α, which determines the inclination of line r_r, is constant for a particular ring and determined using known variables by equation(3.127). Angle θ, which determines the surface normal inclination, is calculated by equation(3.148). Combining the two previous equations results in

(3.150) $$z_i = \frac{R\tan\theta - d\tan\alpha}{\tan\theta + \tan\alpha}.$$

The initial estimate for y_i can now be calculated from equation(3.127) or equation(3.148) using the previously calculated z_i.

4. Equation (3.138) for a better estimate of z_i.
5. Equations (3.140), (3.141), (3.145), and (3.146) to calculate a better θ_i.
6. Equation (3.147) for a new estimate of y_i.
7. Return to step 4.

Step 3 of the iteration in van Saarloos' original work was simply to consider the initial estimate for the reflection point height $y_i = h_i$. The new approach provides a better first estimate.

The sagittal radius of curvature (R_s) for each calculated corneal point is obtained by equation(3.130), as originally suggested by Doss et al. (1981). It's like finding a centred spherical surface containing the calculated corneal point that reflects the ray to the instrument pupil.

For the surface tangential radius of curvature (R_t) at (y_i,z_i), Klein's procedure (1992) was used. This method fits an arc of a circle to three consecutive corneal

points. The centre of curvature of the arc will be located at (c_y,c_z), outside the reflecting surface axis. This method is summarised in the following system of equations:

$$\begin{cases} R_t^2 = (y_{i-1} - c_y)^2 + (z_{i-1} - c_z)^2 \\ R_t^2 = (y_i - c_y)^2 + (z_i - c_z)^2 \\ R_t^2 = (y_{i+1} - c_y)^2 + (z_{i+1} - c_z)^2 \end{cases} . \tag{3.151}$$

The solutions for the centre of curvature coordinates and radius are respectively

$$c_y = \frac{(z_i - z_{i+1})\left[(z_{i-1} - z_i)(z_{i-1} - z_{i+1}) + (y_{i-1}^2 - y_i^2)\right] + (z_{i-1} - z_i)(y_{i+1}^2 - y_i^2)}{2\left[(z_i - z_{i+1})(y_{i-1} - y_i) + (z_{i-1} - z_i)(y_{i+1} - y_i)\right]}, \tag{3.152}$$

$$c_z = \frac{1}{2}\left[z_{i-1} + z_i + \frac{y_{i-1} - y_i}{z_{i-1} - z_i}(y_{i-1} + y_i - 2c_y)\right], \tag{3.153}$$

$$R_t = \sqrt{(y_i - c_y)^2 + (z_i - c_z)^2} . \tag{3.154}$$

This procedure can't be applied to the last ring image, for which there is no next ring available. Therefore the tangential radius of curvature corresponding to the last ring image is considered to be the same as that of the previous ring.

To calculate the sagittal or the tangential radius of curvature at a surface point, with *y* coordinate in between two *y* coordinates with known radius, a linear interpolation was used. The equation is similar to (3.126) using surface *y* coordinates instead of ring mire image heights *h*.

For a non-centred surface several modifications are required in order for the algorithm to work. For a centred surface the system has axial symmetry around the z-axis hence a single semi-meridian was sufficient to analyse the reflecting surface

(the 90 degrees semi-meridian). The variables used are now extended to represent general semi-meridians. Variable h_i and y_i will now represent the image height and a reflective surface point height in a general semi-meridian.

The denominator of equation (3.127), representing the distance from the instrument pupil to the image plane, is changed from $wd+s_{parax}+DF$ to $wd+DF$. The reasons for this change were explained in section 3.12.1.

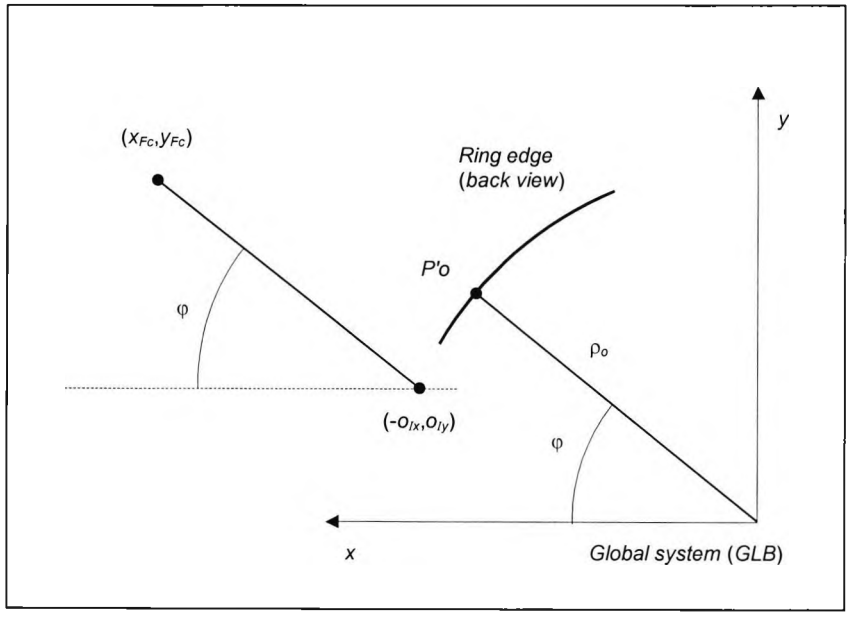

Figure 3.55 – Videokeratoscope selection of the object point corresponding to a given image point. If the image point describes an angle φ with the horizontal the instrument will assume the object point describes the same angle. It considers that the image rings are centred in the instrument axis.

The choice of the object point corresponding to a given image must be obtained using the data available from the videokeratoscope. As an example consider an object point located on the 90 degrees semi-meridian. If the reflecting surface is not centred it may be possible for the image of that object point to be located in the 89 degrees semi-meridian when the semi-meridians are measured centred at o_I (see section 3.10). A videokeratoscope will only know the data taken from the ring mire images and will assume a centred reflecting surface. In this case the

instrument will consider that the object point was in the 89 degrees semi-meridian. The general case for object point selection is represented in Figure 3.55.

The selected object point x, y coordinates in the global system will be expressed by

(3.155) $$P_o' = (\rho_o \sin\varphi, \rho_o \cos\varphi)$$

where

(3.156) $$\sin\varphi = \frac{y_{Fc} - o_{Iy}}{\sqrt{(x_{Fc} + o_{Ix})^2 + (y_{Fc} - o_{Iy})^2}}$$

and

(3.157) $$\cos\varphi = \frac{x_{Fc} + o_{Ix}}{\sqrt{(x_{Fc} + o_{Ix})^2 + (y_{Fc} - o_{Iy})^2}}.$$

Variable ρ_o will replace y_{oi} in the van Saarloos algorithm equations. The other important change will be in the calculation of the apical radius of curvature. Originally van Saarloos considered that the ring mire images could present a lack of symmetry. To account for this he replaced the image height in the 90 degrees semi-meridian in equation(3.127) by the average of the first ring image heights. However this is not very effective, it is best to calculate the apical radius for each image height for the first ring and then calculate the average. This was the approach taken for the simulation program. It should be noted that this increase in accuracy comes at the expense of computation time, which would pose a problem for computers available in 1991 when van Saarloos developed his algorithm.

The fact that for a non-centred surface the image of object points in the same semi-meridian does not fall in the same semi-meridian creates a problem for the application of this algorithm. It should be remembered that the image points need to be in the same semi-meridian for all rings since the data from the previous ring

is used to reconstruct the next surface point. This problem doesn't happen in a videokeratoscope since an image ring is made of an infinite number of image points corresponding to infinite object points hence there are always image points in any semi-meridian. In the simulation program this situation is not possible (except for the centred surface where there is rotational symmetry). However, as explained in section 3.14.2, the ring edge detection procedure executes a rotation of the image resulting in a sector (Figure 3.52). It is reasonable to say that all sectors will share common semi-meridians thus van Saarloos' algorithm is valid in these conditions.

3.16 *Difference maps*

The simulation program calculates a point by point difference of a reference map from a sample map (sample - reference). These two maps can be obtained from any parameters allowed for the simulation. A difference can be obtained from two different algorithms using the same surface and keratoscope geometry or two different targets using the same surface, etc. Differences were calculated in terms of sagittal and tangential radius of curvature or paraxial dioptric power for each one of these radiuses.

Since for centred surfaces there is axial symmetry it is sufficient to calculate the differences for a single semi-meridian. The chosen one was 90 degrees since it has been used previously. The difference must be calculated for the same reflecting surface point radius or power in both maps. A problem arises due to the fact that power or radius calculated in both maps correspond to different surface points. In order to calculate these parameters at the same corneal points equation(3.126) was applied to the spherical biased or van Saarloos algorithm depending on the selected one. It starts at the corneal point closest to the axis in both maps and ends at the last point further from the axis on the map where the last point is smaller. This is due to the fact that an interpolation cannot be achieved beyond the last point of a surface even if the other surface map has several points beyond that.

In between the first and last point an interpolation in both surfaces is executed. This means that for each point on the reference map, a corresponding point on the sample map is calculated by interpolation and vice-versa. These method provides a maximisation of data points for the difference.

If a non-centred surface is used, the only difference map that needs calculating is the one resulting from the centred and the non-centred surface using exactly the same surface and keratoscope parameters. Since there is no axial symmetry for the non-centred surface map, the differences must be calculated for each semi-meridian. The exact semi-meridian of an image point for the non-centred surface can be matched from one of the centred surface since there is axial symmetry in this case. There is only the need to calculate an interpolation to match the radial position. It was decided not to interpolate on the map corresponding to the non-centred surface since that would not provide an adequate value.

In summary, the simulation program is initiated by inputting the data for the designed faceplate, including shape, number of rings, pupil diameter, maximum diameter and working distance. The reflecting surface data is then inputted, including shape, diameter and tilt and decentration if required. The number of object points to use on each ring is the introduced and the focusing mode selected between automatic and manual. After all the parameters have introduced, the program calculates the reflected ring edge heights for the selected object points and generates a sagittal power map or sagittal radius of curvature map based on the spherical biased or the van Saarloos algorithm. The tangential power or radius of curvature is also calculated and stored in file. A second map can then be calculated using different parameters and a difference map is generated. This allows studying the effect of individual parameters.

The developed simulation programs allows to study the impact of several parameters on power or radius of curvature maps, such as:

- Effect of faceplate shape
- Effect of working distance
- Effect of pupil diameter (excluding diffraction)
- Reflecting surface shape
- Reflecting surface decentration
- Reflecting surface tilt
- Focus
- Two reconstruction algorithms (spherical biased and van Saarloos).

Difference maps can also be generated from almost any combination of parameters, including reconstruction algorithms.

The following chapter consists on applications of the simulation program on faceplate shape studies and tilt, decentration and focus errors.

4 Methods

The videokeratoscope computer model was used to assess the design of faceplates in videokeratoscopes to determine the effect of faceplate geometry on image quality and hence accuracy of the radius of curvature maps. This would allow us to understand the advantages of the plethora of designs that are currently available and to know whether changes produced by different faceplate geometries are clinically significant.

Stone (1962) suggested that an accuracy of 0.02 mm is needed for instruments designed to measure radius of curvature of ophthalmic surfaces. This is due to the fact that contact lenses are manufactured in 0.05 mm steps therefore the accuracy should be approximately half that value. Taking this into account a difference between two radii of curvature equal or larger than 0.02 mm was considered as clinically significant for the scope of this work.

Roberts (1996) pointed out that in keratometry, which measures a central region of the cornea, power and radius of curvature are inversely proportional [$P=(n-1)/R$]. However videokeratoscopes can measure a wider area including the peripheral cornea where this relation is no longer valid. In fact the refractive power increases for the periphery of a positive spherical lens where according to the previous equation it should be constant over the entire surface. This power increment is the basis of spherical aberration. To avoid this error the research work on faceplate design was based on radius of curvature rather than power.

The study was divided into two parts: the determination of the best faceplate design and comparison of the resultant radius of curvature errors with errors generated from other faceplate designs to search for clinically significant differences.

4.1 *Determination of best faceplate design*

The average corneal surface used as a model for all faceplate designs had a 7.72-mm central radius of curvature, and a *p* value of 0.81 (see section 3.2), corresponding to a prolate ellipsoid. This corneal model was considered reasonable over a 9 mm corneal diameter.

All the modelled faceplates had a pupil diameter of 9 mm, which is approximately the average aperture seen in several commercial instruments. The models were tested at 120, 80 and 50 mm distances from the corneal vertex to the instrument pupil plane (Figure 4.1 b). These values cover the range used by several commercial instruments.

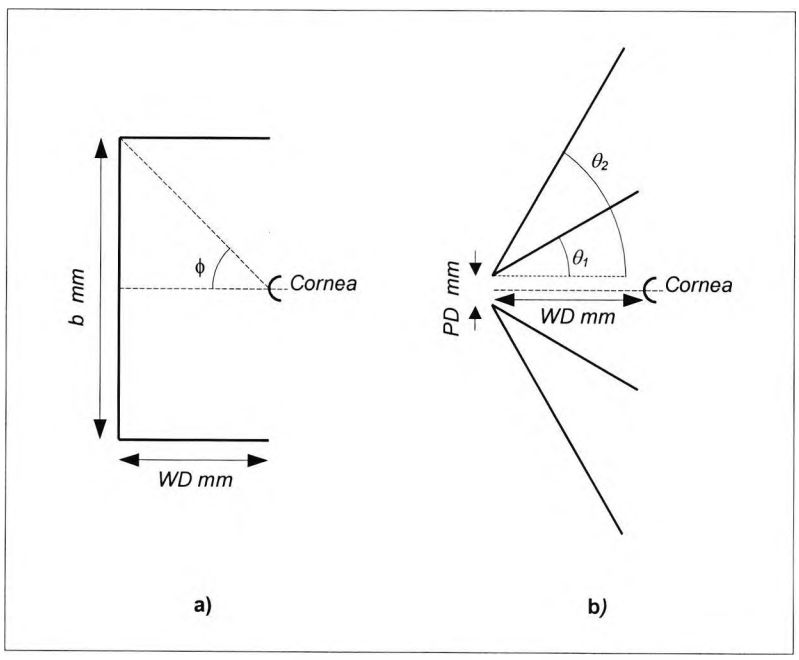

Figure 4.1 - Sections of cylindrical and cone shaped faceplates. **a)** The angle ϕ from the cylinder base to the opposite corner can be used to control the diameter *b* and the length *WD*. **b)** Cones with semi-aperture angles θ_1 and θ_2. Both cones start at a 9mm pupil aperture.

A flat surface was tested at the three specified distances. For the cylindrical surfaces tested, at each distance the diameter of the cylinder was changed from 25

mm to 240 mm in 1 mm steps. Diameters less than 25 mm were not tested because it would be difficult to manufacture such surfaces engraving the rings accurately and in a smaller surface less rings can be fitted. The maximum diameter 240 mm corresponds to a 45 degree angle between the corneal vertex and the cylinder corner at a 120 mm distance (Figure 4.1 a). Larger diameters would make the cylinder approach a flat surface. Naturally for the shorter distances the angle at the cylinder corner will be bigger than 45 degrees for a 240 mm diameter.

Cones were tested at each distance with semi-aperture angles ranging from 1 to 89 degrees in 1 degree steps (Figure 4.1 b). The other conoidal surfaces were modelled by *p* value and apical radius of curvature. For each *p* value the radius of curvature was changed from 5 to 250 mm in 5 mm steps. A radius of curvature larger than 250 mm would represent almost flat surfaces for the diameter analysed. Negative *p* values, corresponding to a hyperbolic surface, were tested and incremented in such a way that the asymptotic line (Figure 4.2) would change by 1 degree in each increment, similar to the procedure for the cone.

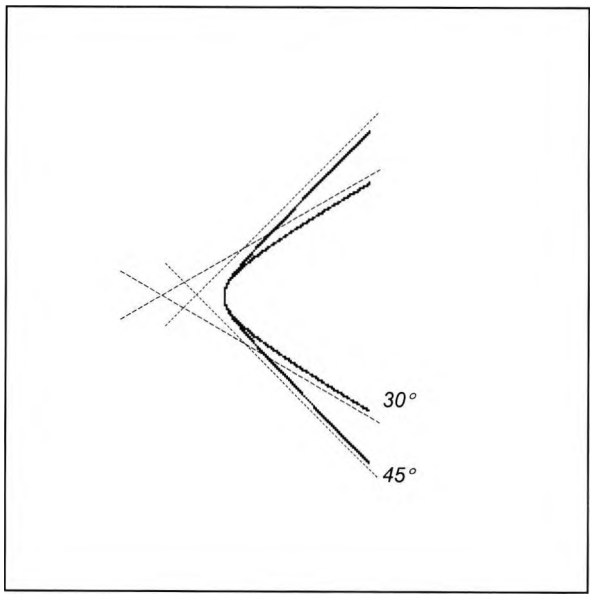

Figure 4.2 - Hyperboles with the same apical radius of curvature and asymptotic lines at 30 and 45 degrees inclination. The curves are similar to a cone in the periphery, but different at the centre.

When the *p* value reached zero, corresponding to a parabolic surface, the value of *p* was incremented in 0.1 intervals until a surface that wouldn't intersect a 45 degree line from the corneal vertex was obtained (Figure 4.3). The constant increment to *p* wasn't used for the hyperbola since it would be too small for steep asymptotic lines and too large for asymptotic lines closer to horizontal. As an example the *p* values for asymptotic lines with 88 and 89 degree inclinations are respectively –820.04 and –3282.14. The *p* values for asymptotic lines with 29 and 30 degree inclinations are respectively –0.31 and –0.33.

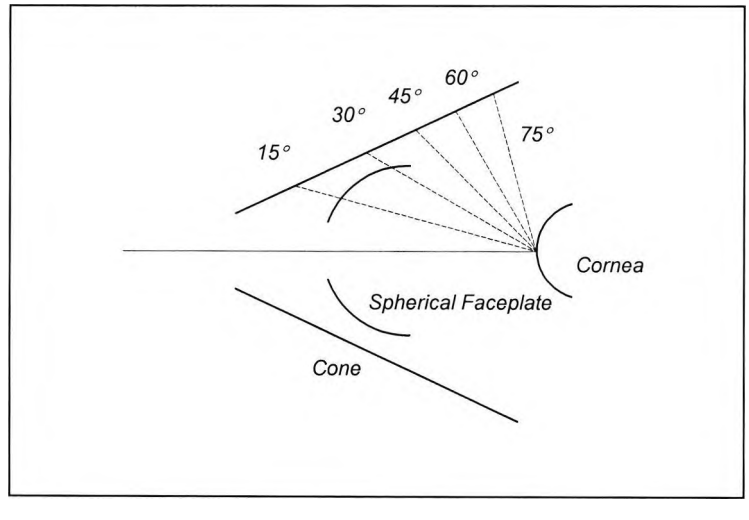

Figure 4.3 - In a cone shaped faceplate it is always possible to define the five points (see text) as long as the cone has sufficient length to either side. The same applies to cylindrical, hyperbolic and parabolic faceplates. In spherical and ellipsoidal faceplates the surface can only increase in diameter until a certain point, after which it starts to close. In these cases it is not always possible to find the five points. The figure represents a case where it is only possible to define two of the five points.

One important factor in selecting an appropriate faceplate design refers to the most peripheral corneal point that reflects rays through the instrument pupil. If such point is near the central area, accuracy in the corneal reconstruction would be compromised since conoidal surfaces can be very similar in the centre and

different in the periphery (Figure 3.1). In order to maximise accuracy peripheral corneal points must transmit rays through the instrument pupil. The program only processes faceplate shapes such that the ray that strikes the cornea furthest away from the axis and is transmitted through the instrument pupil, strikes the cornea at a distance no smaller than 4 mm from the axis. This condition allows the analysis of at least an 8 mm corneal diameter, the total coverage claimed by several instruments manufacturers.

Five points in the faceplate subtending 15, 30, 45, 60 and 75 degrees at the corneal apex were selected. Cones, cylinders, hyperboloids and paraboloids will always have points that subtend these five angles. Spheres and ellipsoids can only increase in diameter until a certain point, and then start decreasing, hence it was not always possible to find the five points. The choice of these five equispaced points was based on an empirical relation between faceplate sampling points and computation time. Although increasing the number of points results in better accuracy, the great number of surfaces tested would result in a excessively large computation time.

For each faceplate design the minimum blur sum was calculated adding the tangential blurs of each point at the best focus position (see section 3.12.2). The surface that provided the sharpest image was the one with the lowest minimum blur sum. All faceplate designs that passed the 8 mm corneal coverage criterion were divided in four classes. The first class included the ones that produced minimum blur sum differences $\leq$ 0.001 mm from the best, the second $\leq$ 0.01 mm, the third $\leq$ 0.1 mm and the fourth > 0.1 mm.

4.2 *Influence of faceplate design on radius of curvature maps*

The best faceplate design and a surface representing each of the minimum blur sum based classes, mentioned above, were compared. Since each surface is tested separately and there are only five surface geometries to compare, computation time is no longer a problem, hence the number of points tested in

each faceplate can increase. Sixteen points were selected, which is equivalent to eight rings on the faceplate. This number is similar to the one used in videokeratoscopes that analyse ring edges. Videokeratoscopes that have a large number of rings do not analyse ring edges but the average position of the complete image ring, since the image is very thin.

Sagittal and tangential radius of curvature for the simulated cornea were calculated by the van Saarloos algorithm (see section 3.15.2) for the best and for a representative of each of the other four minimum blur sum based classes. These designs were also selected with the criterion of not being too different from faceplates used in commercial instruments. For example a cylinder with the base larger than its length is not found in videokeratoscopes.

As mentioned in section 3.16, the problem with difference maps is that for different faceplate shapes (with the same number of rings) the reflection points on the simulated cornea will not be the same. To overcome this problem the corneal reflection points radial coordinates for the best faceplate surface were used as a reference and the radius of curvature for the same points based on the data from other faceplates were calculated. This was done by linear interpolation of radius of curvature between two calculated corneal points using equation(3.126) applied to the van Saarloos algorithm. After this step the radius of curvature values for corneal points with the same radial coordinates, calculated from different faceplates, will be available. For the selected reference points the accurate sagittal and tangential radius of curvature were calculated from the simulated cornea parameters (apical radius and p value) using equations(3.14) and (3.16) respectively. For each faceplate design, the radius of curvature error was calculated for each corneal reference point. This error was determined for each point, subtracting the calculated radius of curvature (in the van Saarloos algorithm) from the accurate radius of curvature. This process was applied both to the sagittal and tangential radius of curvature resulting in the sagittal radius error and tangential radius error. These errors were plotted on graphs and compared

between surfaces for several videokeratoscopes parameters. These parameters were:

- Faceplates with 9 mm pupils and image plane at best focus.
- Faceplates with 9 mm pupils and image plane at first ring focus.
- Faceplates with 4 mm pupils and image plane at best focus.

4.3 *Effect of reflecting surface decentration on radius of curvature maps*

Using the best faceplate design, the average simulated cornea was decentred 0.5 mm (ρ) along the 0° semi-meridian (σ) (see section 3.4). The image plane position was set to focus on the inner ring mire image, as indicated by the conclusions of the faceplate design research (see section 6.2). Since the decentration led to an axial symmetry loss, the inner ring mire image couldn't be focused on all meridians at once. The best focus for the inner ring mire image was calculated from 8 equispaced points. This position was used as the image plane position for all image rings.

Although there is a loss of axial symmetry, the decentration along the horizontal direction still leaves planar symmetry about the horizontal meridian. This means that the image above the horizontal direction is a mirror image of the image below that direction. Therefore only the data for the horizontal and 1st and 2nd quadrant semi-meridians are presented.

4.4 *Effect of reflecting surface tilt on radius of curvature maps*

Using the best faceplate design, the average simulated cornea was tilted 1° (θ) along the 0° semi-meridian (σ = 0° $\rightarrow$ φ = 180°) (see section 3.3). A decentration was also applied in order to simulate the videokeratoscope alignment procedure (see section 3.11). The focusing procedure and image semi-meridian selection followed the same criteria applied to the decentration effect research.

In summary, the simulation program was used in four experiments. This chapter describes the methods used for each experiment. For the determination of the best faceplate design (section 4.1), flat, cylindrical, conical and conoidal faceplates were used and the minimum tangential blur sums for five object points were calculated. Each faceplate was tested at 50, 80 and 120 mm working distances. In the cylindrical faceplate group several base diameters were tested, in the cones group several cone apertures were tested and in the conoidal group several conoids with different apical radius and *p* values were tested. For all faceplate designs the same reflecting surface was used with parameters of an average corneal surface. The best faceplate design was the one that provided the minimum blur sum (sharpest image) and the other designs were divided in four classes accordingly to their minimum blur sums. For the influence of faceplate design on radius of curvature maps experiment, the best faceplate design with eight rings (sixteen ring edges) was used on the average cornea to determine the sagittal and tangential radius of curvature errors, using the van Saarloos algorithm on sixteen points of a corneal semi-meridian. This was done for 4 and 9 mm pupil diameter with best focus and focus at the central ring image mire. Four other faceplate designs from each of the minimum blur sums classes defined in the best faceplate design experiment were used. For each design the sagittal and tangential radius of curvature errors were compared to the errors of the best faceplate design at the same corneal points. This procedure was repeated for the 4 and 9 mm pupils and focus at the best and inner ring image mire focus. The error differences between faceplate results were then analysed to search for clinically significant differences, defined as a difference equal or larger than 0.02 mm.

For the effect of reflecting surface decentration on radius of curvature maps (section 4.3) a 0.5 mm decentration was applied to the average corneal surface using the best faceplate design with a 9 mm pupil and 8 rings, focusing at the inner image ring mire. The sagittal radius error was calculated for 16 points of a semi-meridian and compared to the sagittal radius error for a centred corneal surface at

the same corneal points; differences were then analysed. The process was repeated for four other semi-meridians.

For the effect of reflecting surface tilt on radius of curvature map experiment (section 4.4) a 1° tilt was applied to the average corneal surface and the rest of the experiment followed the same steps as the decentration experiment.

The following chapter shows the results of each one of the four experiments. The displayed graphs were obtained from the error values given by the computer simulation.

5 Results

5.1 *Determination of best faceplate design*

Table 5.1 summarises the lowest minimum blur sums for each type of surface tested.

Surface	Minimum Sum (mm)
Flat	0.102678
Cone	0.029046
Cylinder	0.028208
Other conic surfaces	0.055651

Table 5.1- Minimum blur sums for the tested surfaces

The minimum sum displayed for the flat surface corresponded to a distance of 80 mm from the corneal vertex. The best cylinder had a diameter of 26 mm and base located at 120 mm from the cornea. The best cone had the pupil aperture located at 120 mm from the cornea with a total aperture angle of 8 degrees (4 degrees semi-aperture). The best conoidal surface was a hyperboloid with the pupil aperture at 120 mm from the cornea, 20 mm radius of curvature and a *p* value of –0.163237.

The total of surfaces initially tested ascended to 112781. From those only 13058 fulfilled the 8 mm corneal coverage condition and were subject to the minimum blur sums calculation routine. The lowest minimum blur sum, (0.028208 mm), corresponded to the cylindrical surface previously specified. Statistics on the number of surfaces that matched the best sum within 0.001 mm, from 0.001 to 0.01 mm, from 0.01 to 0.1 mm and more then 0.1 mm were also registered. Table 5.2 summarises the frequency of each group for the different types of surfaces. It should be noted that the frequencies are not cumulative.

	Tested	Pass 8 mm	Δ<=0.001mm	0.001<Δ<= 0.01	0.01<Δ<=0.1	Δ>0.1mm
Flat	3	2	0	0	1	1
Cone	267	192	1	1	120	70
Cylinder	648	550	2	7	350	191
Other	111863	12314	0	0	5785	6529
Total	112781	13058	3	8	6256	6791

Table 5.2 – Frequency table for differences (Δ) from the smallest minimum blur sum.

Two surfaces closely matched the best, the first (second best) was another cylinder with the base located at 120mm from the cornea and a diameter of 27-mm (1mm larger than the best). The other surface (third best) was a cone (best cone in Table 5.1).

5.2 *Influence of faceplate design on radius of curvature maps*

The surfaces selected to represent each class in Table 5.2 were:

- Best surface (min blur 0.028208 mm)
- Cone 8 degrees total aperture, 25.5 mm maximum diameter, 119 mm length (min blur 0.029046 mm).
- Cylinder 34 mm diameter, 119 mm length (min blur 0.037396 mm)
- Cylinder 49 mm diameter, 49 mm length (min blur 0.126955 mm)
- Cone 160 degrees total aperture, 240 mm maximum diameter, 49 mm length (min blur 0.182992 mm).

For simplicity the selected surfaces will be labelled surfaces 1 to 5 respectively. The sagittal radius of curvature errors (*SRE*) and tangential radius of curvature errors (*TRE*) calculated for each one of the five faceplate designs are represented in Figure 5.1 and Figure 5.2 respectively. These errors were calculated using a 9 mm pupil in the faceplate and image plane at best focus. In the abscissas *d* is the

distance from the corneal point to the axis of the simulated cornea measured perpendicular to the axis. From the dots on the error curve for surface 5, radial coordinates *d*, for which radii of curvature were calculated for all surfaces, can be identified.

The sagittal and tangential radius of curvature errors for a 9 mm pupil diameter in the faceplate and image plane at the focus of the first ring mire image are represented in Figure 5.3 and Figure 5.4 respectively.

The sagittal and tangential radii of curvature errors for a 4 mm pupil and image plane at best focus are represented in Figure 5.5 and Figure 5.6 respectively.

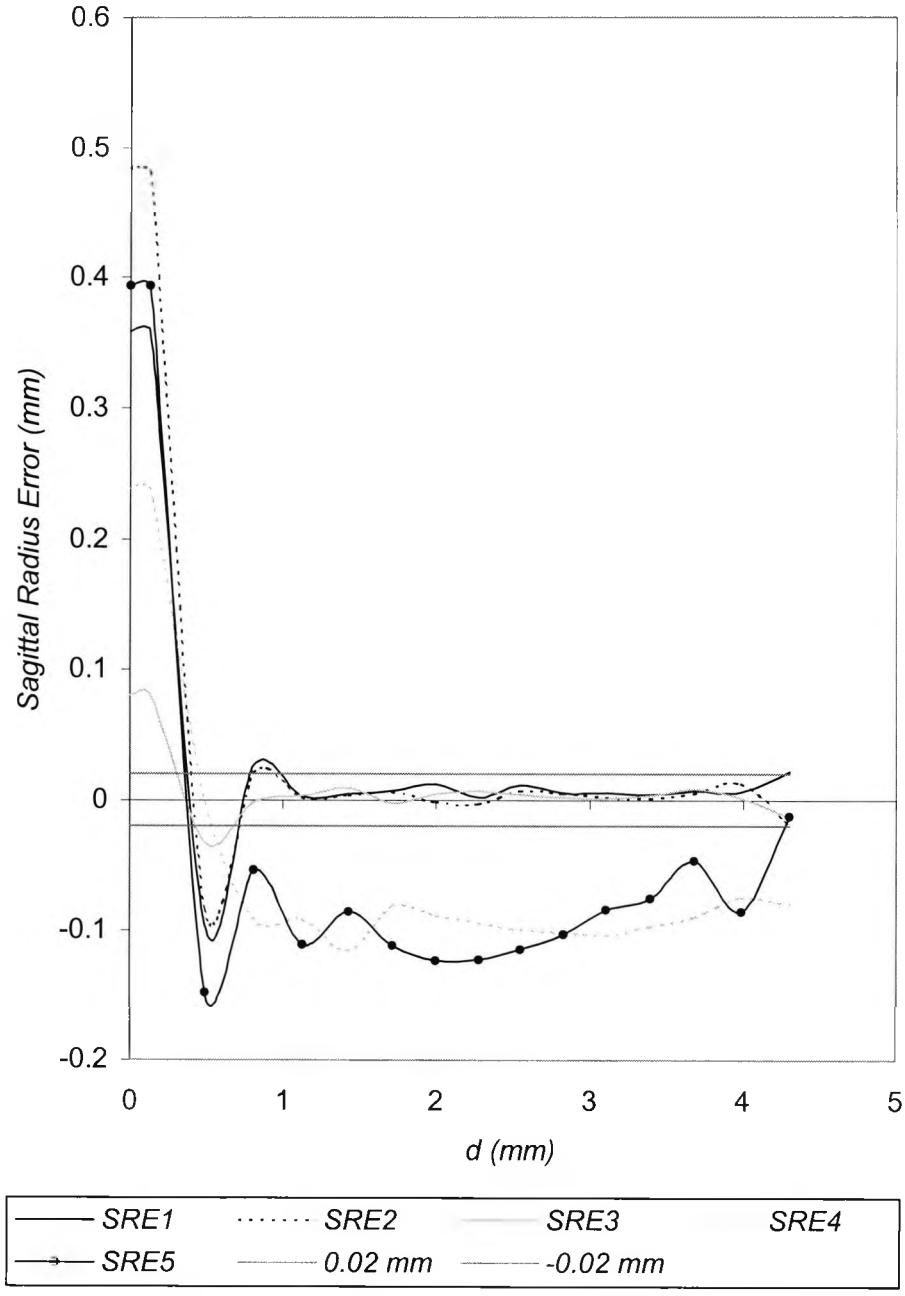

Figure 5.1- Differences (*SRE*) between accurate sagittal radii of curvature and sagittal radii of curvature calculated by the van Saarloos algorithm for surfaces 1 to 5. Faceplate pupil with 9 mm diameter and image plane at best focus.

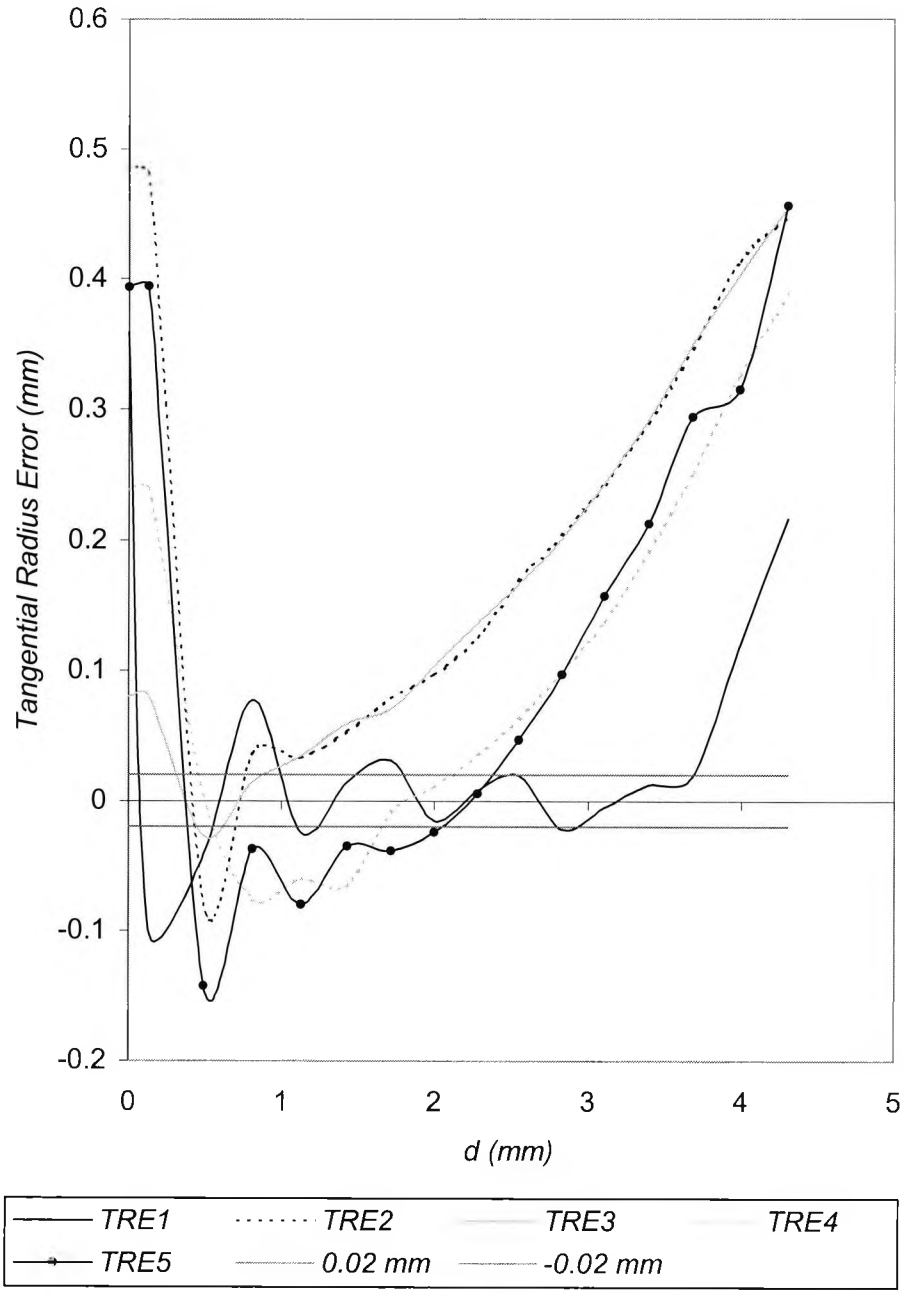

Figure 5.2 - Differences (*TRE*) between accurate tangential radii of curvature and tangential radii of curvature calculated by the van Saarloos algorithm for surfaces 1 to 5. Faceplate pupil with 9 mm diameter and image plane at best focus.

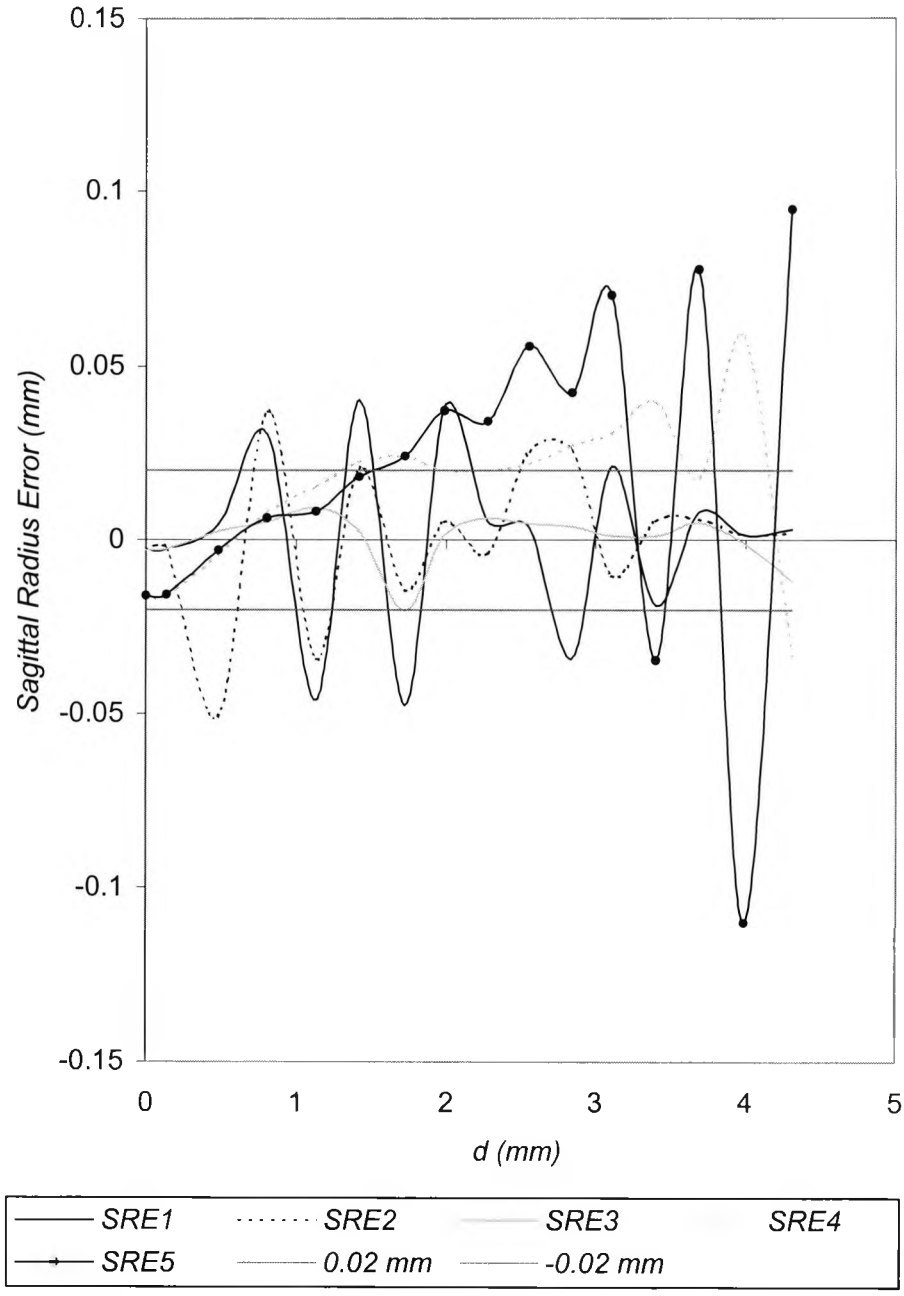

Figure 5.3 - Differences (*SRE*) between accurate sagittal radii of curvature and sagittal radii of curvature calculated by the van Saarloos algorithm for surfaces 1 to 5. Faceplate pupil with 9 mm diameter and image plane at first ring mire image focus.

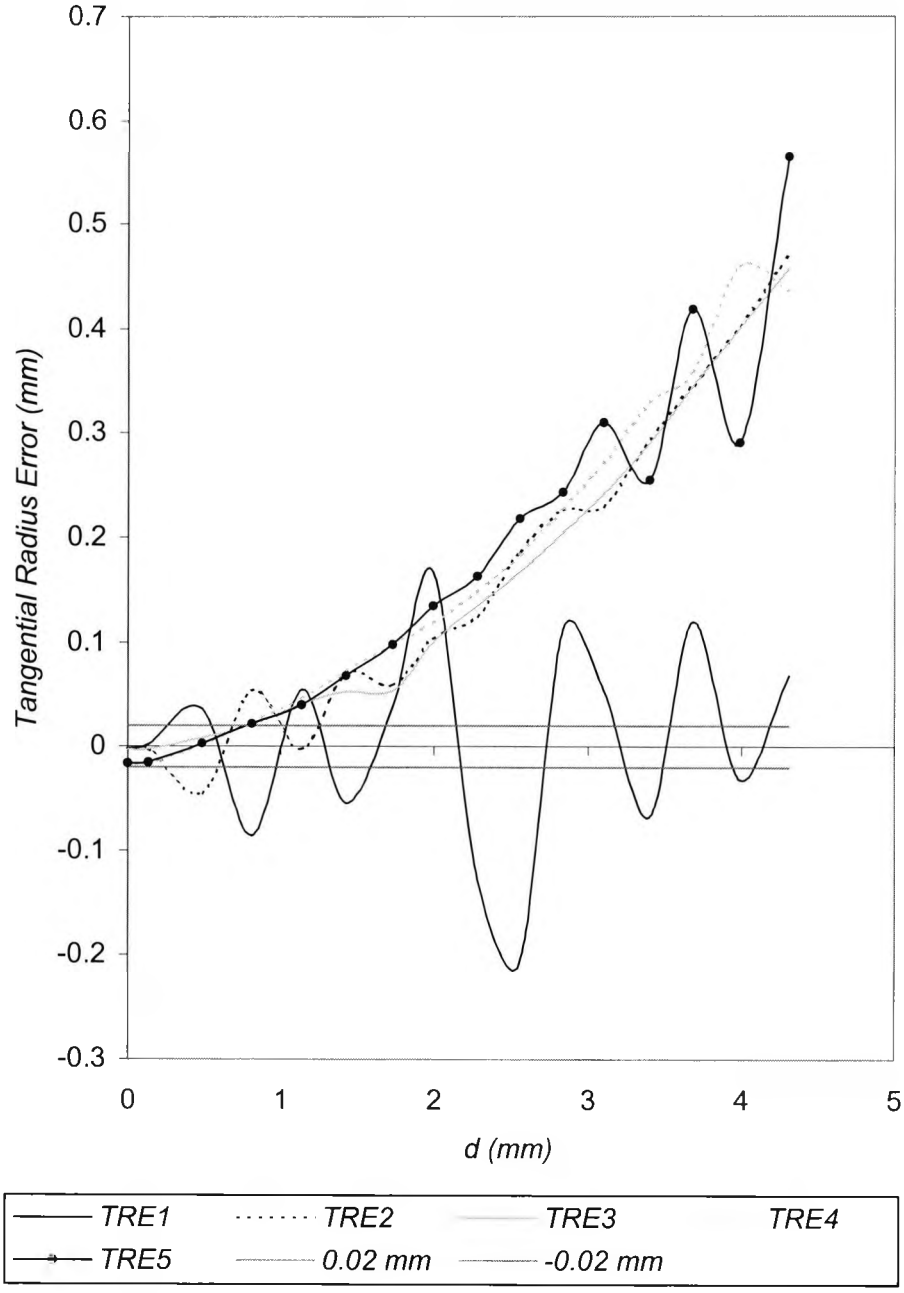

Figure 5.4 - Differences (*TRE*) between accurate tangential radii of curvature and tangential radii of curvature calculated by the van Saarloos algorithm for surfaces 1 to 5. Faceplate pupil with 9 mm diameter and image plane at first ring mire image focus.

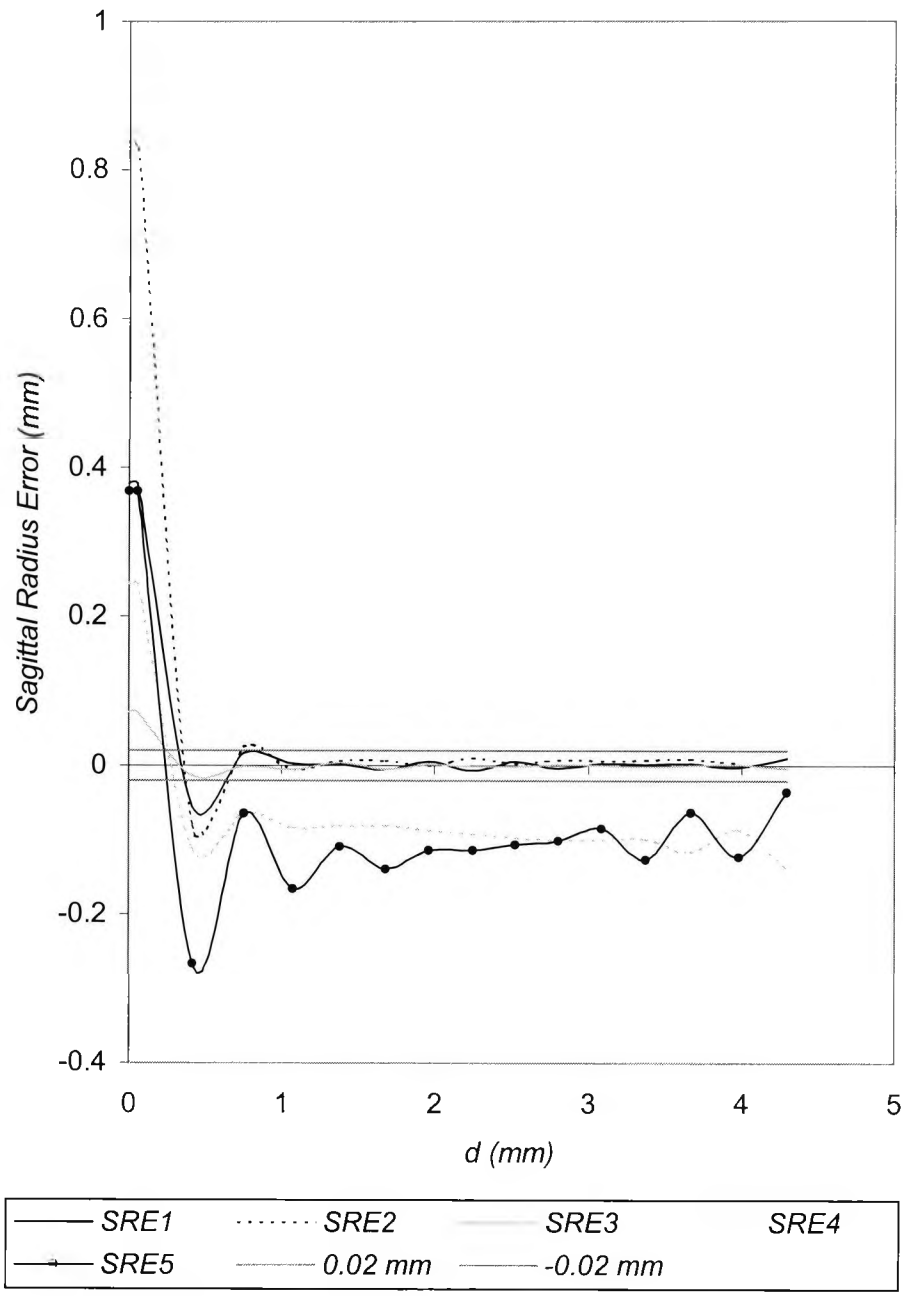

Figure 5.5 - Differences (*SRE*) between accurate sagittal radii of curvature and sagittal radii of curvature calculated by the van Saarloos algorithm for surfaces 1 to 5. Faceplate pupil with 4 mm diameter and image plane at best focus.

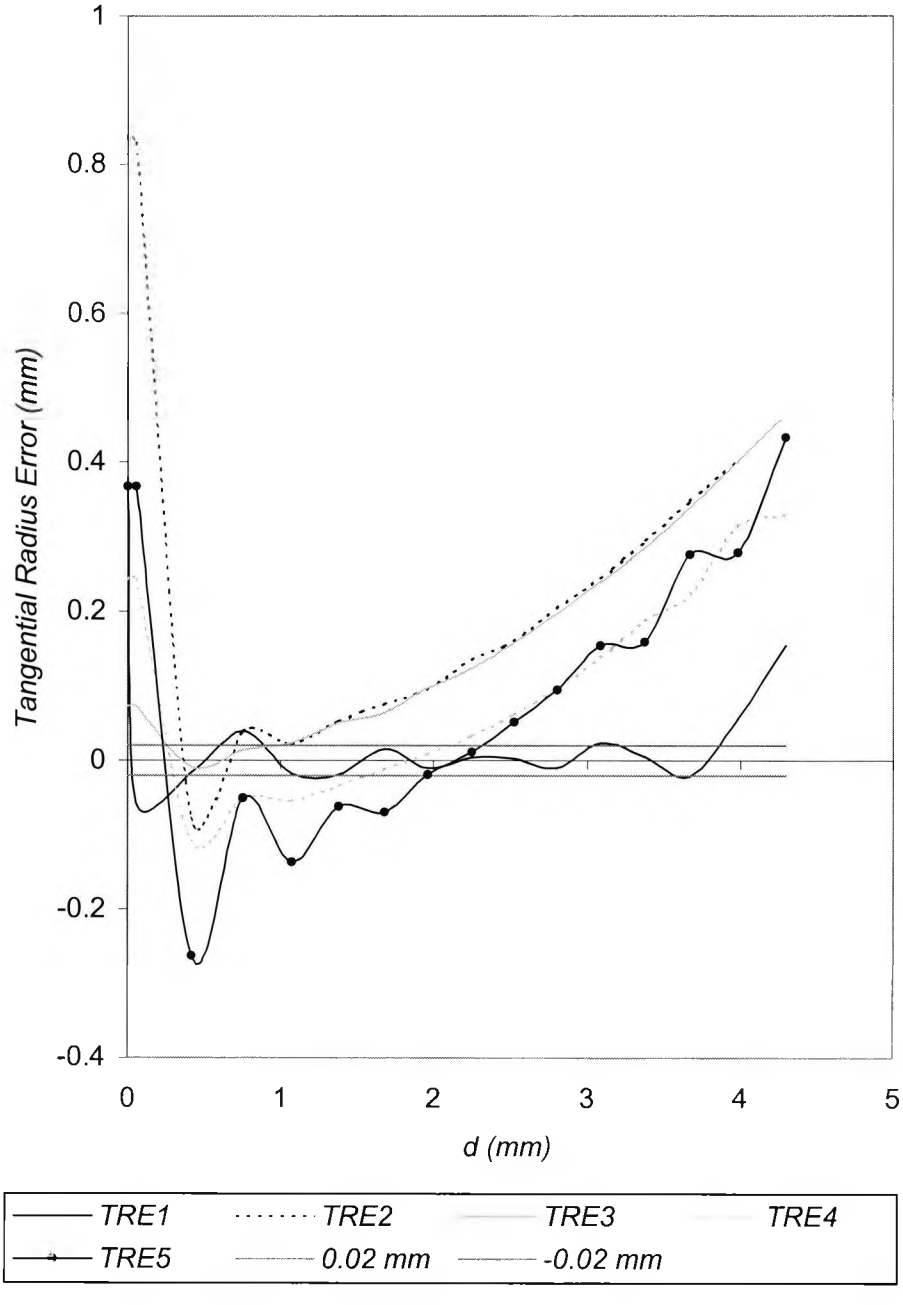

Figure 5.6 - Differences (*TRE*) between accurate tangential radii of curvature and tangential radii of curvature calculated by the van Saarloos algorithm for surfaces 1 to 5. Faceplate pupil with 4 mm diameter and image plane at best focus.

5.3 *Effect of reflecting surface decentration on radius of curvature maps*

The average focal plane position for the eight semi-meridians was 3.74 mm from the surface vertex. The sagittal radius error, *SREDEC* (exact-calculated sagittal radius of curvature), is represented for each semi-meridian (σ) in Figure 5.7 to Figure 5.11. Each figure also displays the sagittal radius error for the centred reflecting surface, SRECTR, at the same points for comparison.

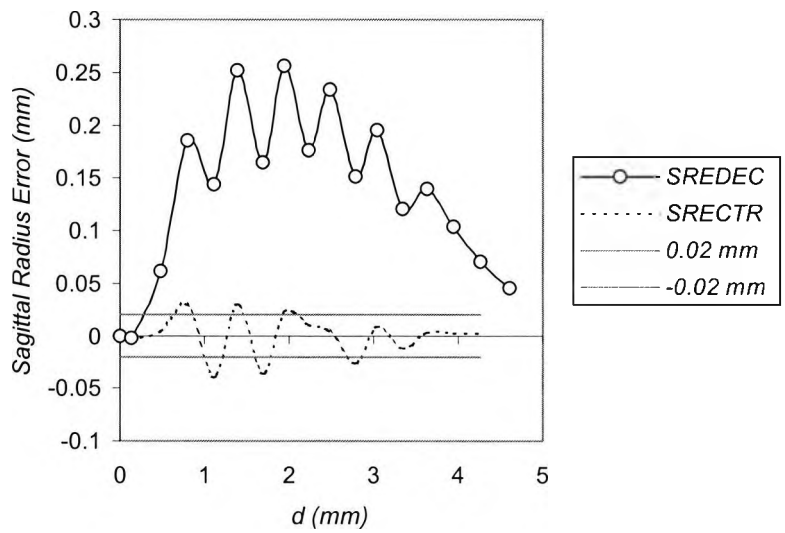

Figure 5.7 - Sagittal radius error for the decentred surface measured along the 0° semi-meridian (*SREDEC*) and sagittal radius error for a centred surface (*SRECTR*) in the same points.

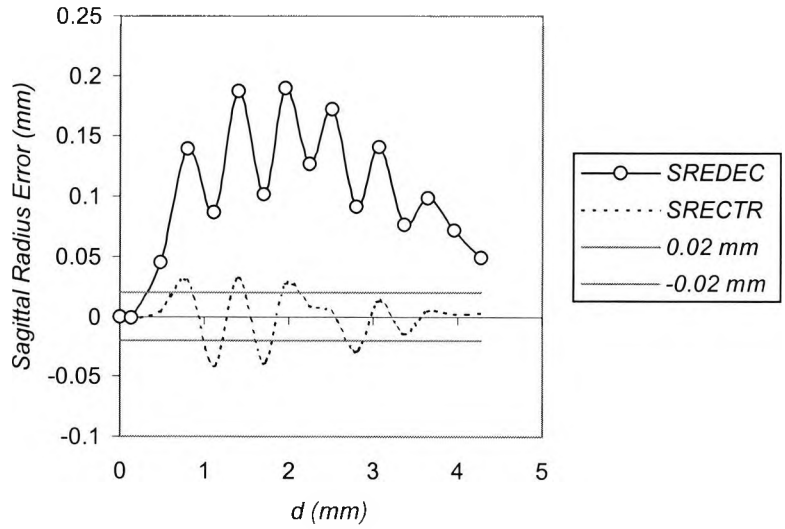

Figure 5.8 – Sagittal radius error for the decentred surface measured along the 45° semi-meridian (*SREDEC*) and sagittal radius error for a centred surface (*SRECTR*) in the same points.

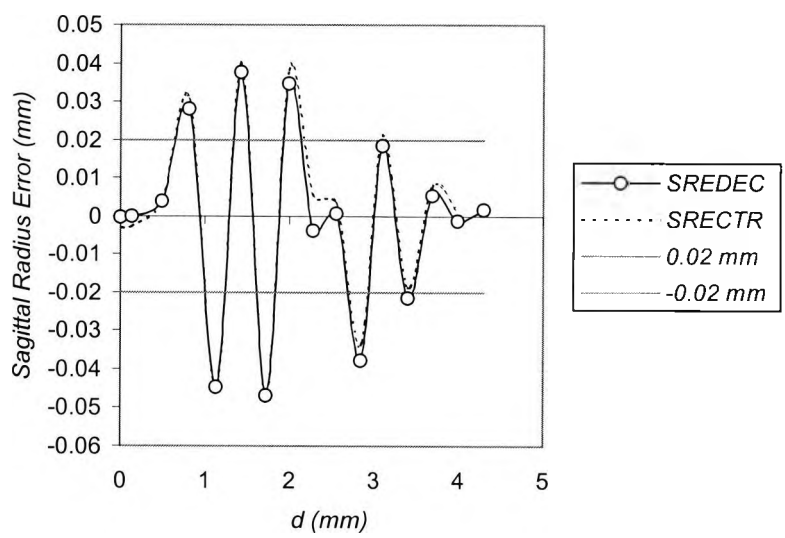

Figure 5.9 – Sagittal radius error for the decentred surface measured along the 90° semi-meridian (*SREDEC*) and sagittal radius error for a centred surface (*SRECTR*) in the same points.

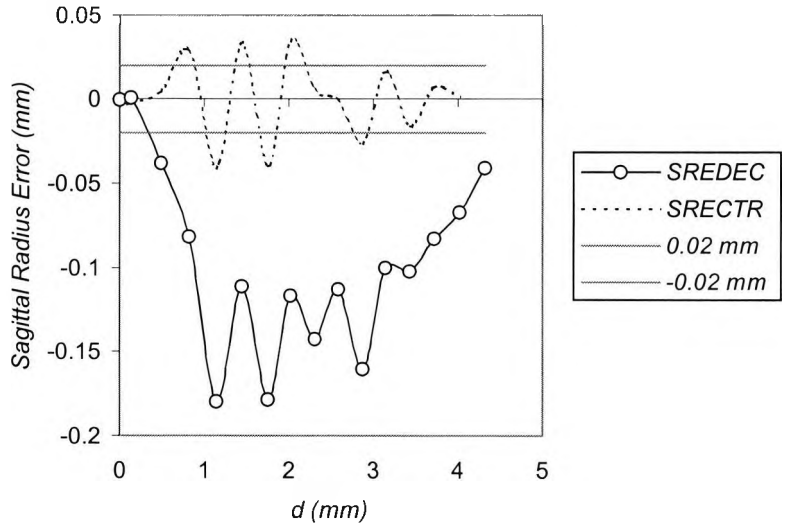

Figure 5.10 – Sagittal radius error for the decentred surface measured along the 135° semi-meridian (*SREDEC*) and sagittal radius error for a centred surface (*SRECTR*) in the same points.

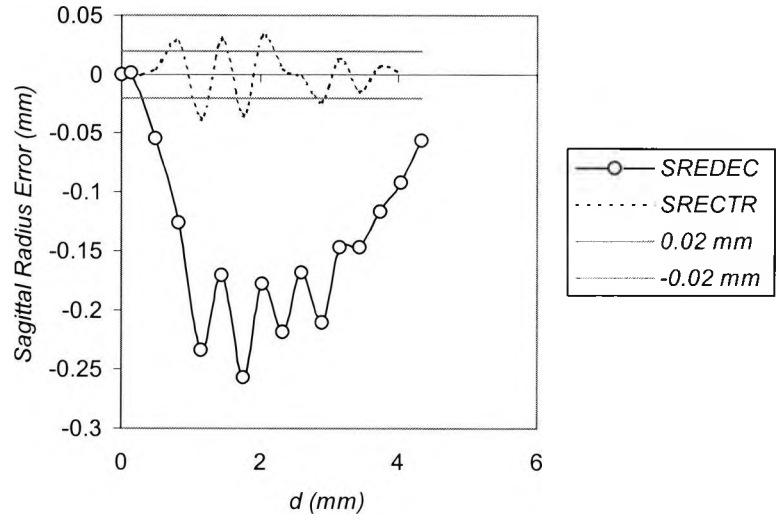

Figure 5.11 – Sagittal radius error for the decentred surface measured along the 180° semi-meridian (*SREDEC*) and sagittal radius error for a centred surface (*SRECTR*) in the same points.

5.4 *Effect of reflecting surface tilt on radius of curvature maps*

After applying the 1° tilt in the 0° semi-meridian, a decentration has to be done to align the surface. Since the videokeratoscope axis is on the positive *z*-axis direction it's represented by the vector $[0,0,1]_{GLB}$ (global system). This direction is changed to the tilted system applying equations (3.37) with φ=180° and θ=1° resulting in a vector with components L=sin 1°, M=0 and N=cos 1°. Now equations (3.89) can be applied to determine the coordinates of the tilted surface point with normal in the same direction resulting in (x_N,y_N,z_N)=(-0.135, 0, 0.001). If these coordinates are applied to equations (3.38) the respective coordinates on the global system (but centred at the reflecting surface vertex) can be obtained. From these only *x* is important since it's the direction of decentration. The value for x will be -0.135 (to three decimal places). This means that the tilted surface point with normal in the same direction of the videokeratoscope axis is located at x=-0.135 mm (global system coordinates) from the videokeratoscope axis. In order to align this point with the axis the surface must be shifted 0.135 mm towards the positive *x*-axis direction, corresponding to semi-meridian σ=180° (*IMG* system used to define tilt and decentration directions).

The average focal plane position for the eight semi-meridians was 3.739 mm from the surface vertex. The sagittal radius error, *SREDEC* (exact-calculated sagittal radius of curvature), is represented for each semi-meridian (σ) in Figure 5.12 to Figure 5.16. Each figure also displays the sagittal radius error for the centred reflecting surface, *SRECTR*, at the same points for comparison.

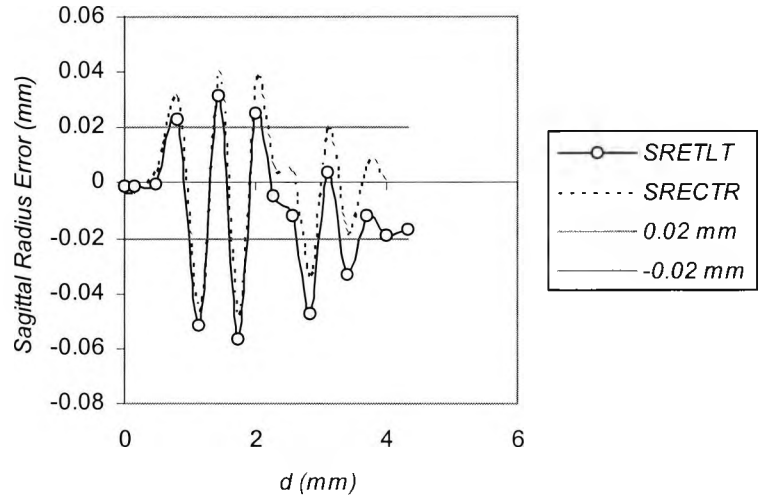

Figure 5.12– Sagittal radius error for the tilted surface measured along the 0° semi-meridian (*SRETLT*) and sagittal radius error for a centred surface (*SRECTR*) in the same points.

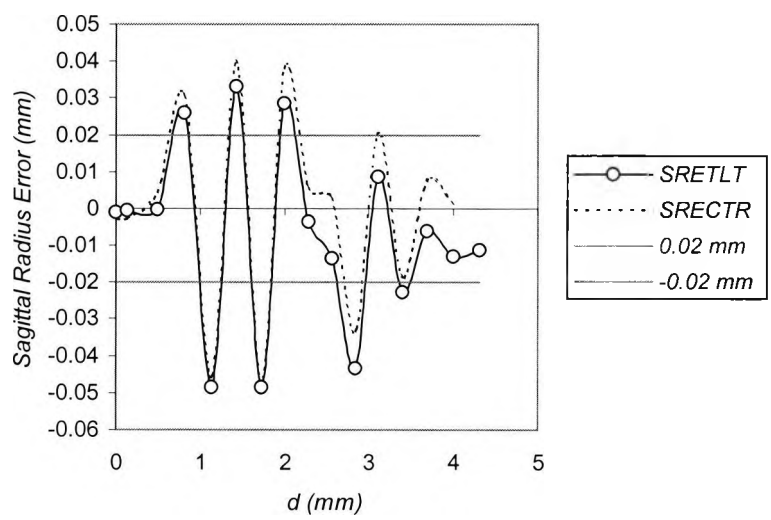

Figure 5.13 – Sagittal radius error for the tilted surface measured along the 45° semi-meridian (*SRETLT*) and sagittal radius error for a centred surface (*SRECTR*) in the same points.

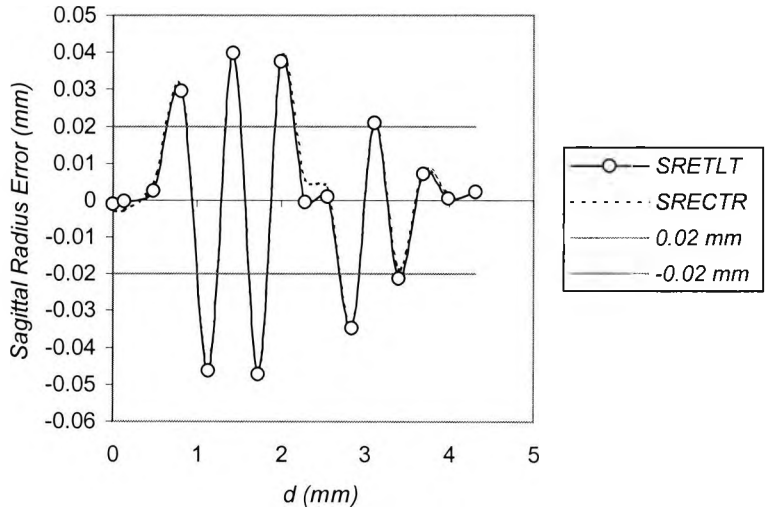

Figure 5.14 – Sagittal radius error for the tilted surface measured along the 90° semi-meridian (*SRETLT*) and sagittal radius error for a centred surface (*SRECTR*) in the same points.

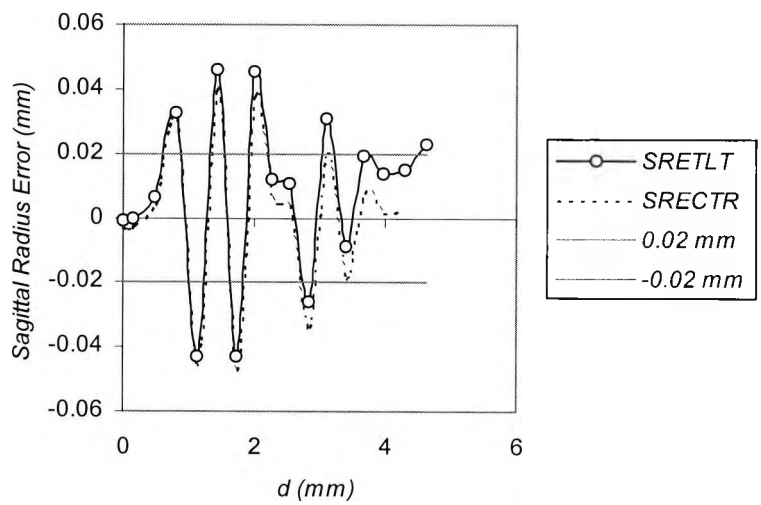

Figure 5.15– Sagittal radius error for the tilted surface measured along the 135° semi-meridian (*SRETLT*) and sagittal radius error for a centred surface (*SRECTR*) in the same points.

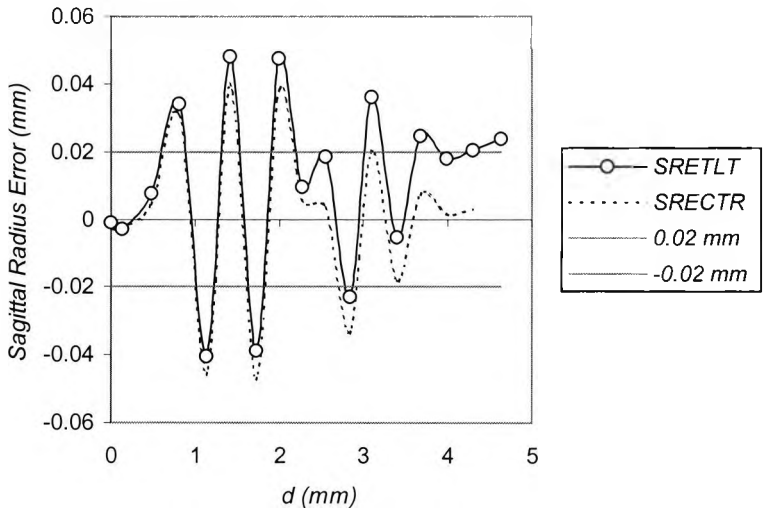

Figure 5.16 – Sagittal radius error for the tilted surface measured along the 180° semi-meridian (*SRETLT*) and sagittal radius error for a centred surface (*SRECTR*) in the same points.

In summary, the best faceplate design was a cylinder with a 26 mm base located at 120 mm from the corneal vertex. Two other faceplate designs had minimum blur sums 1 μm larger than the best. Most faceplate designs had minimum blur sums larger than 10 μm in relation to the best design. There was a large error in the calculated apical radius of curvature when the best focus was used. If focus at the inner edge of the image ring mire is used, the apical radius of curvature error becomes negligible. This focal plane position also decreases overall error. Focus has more influence on the results than geometrical aberrations controlled by pupil size. Reducing pupil size or changing focus has a small effect on tangential radius of curvature errors.

Reflecting surface decentration has a large effect on the radius of curvature errors when compared to the errors for a centred surface. The error differences are clinically significant in the semi-meridian of decentration and become negligible in the perpendicular semi-meridian. Ring crowding occurs for the semi-meridian of decentration and ring spacing for the opposite semi-meridian.

The findings for the reflecting surface tilt are similar to the decentration, since to simulate the videokeratoscope alignment procedure a vertex decentration has to be executed. The only difference was that the error difference in relation to the centred surface error increased towards the periphery.

On the following chapter this results are analysed and their importance discussed.

6 Discussion

6.1 *Determination of best faceplate design*

In the best conoidal and best flat surface the blur patterns are partially vignetted at the 75 degrees points. This vignetting is an artefact of the program due to the corneal diameter being limited to 9 mm. In the periphery the real cornea adopts a flatter shape and the rays would strike that part without being vignetted. As a result the blur would be bigger than actually is measured in the simulation. Within the minimum blur sums (minimum value of the sum of the radial geometrical blurs for five predefined object points) for each type of surface, the flat and conoidal surface present the highest values. For these two cases the vignetting is of no concern because it would make the minimum blur sums even larger. The best cone and the best cylinder do not induce vignetting at the 75 degrees points. The minimum blur sums for these two particular surfaces are therefore correct.

Figure 6.1 displays the distance of the best focus position from the paraxial plane for 15 image ring edges for the best cylinder. From this figure it can be seen why that cylinder produces the minimum blur sum. The first and last set of edges are focused near the paraxial plane (0 mm on the graph) and only the intermediate edges are focused away from the paraxial plane. Hence if the image plane is set for the first ring edge (paraxial plane) the blur sum will be small since only the intermediate rings will be out of focus.

In order to fill the pupil, a bundle of rays reflected on the cornea must spread less if the cornea is further away. This explains why surfaces placed at larger working distances present smaller blur sums. On the other hand the distance has to be limited for an adequate corneal area to be analysed since it was found by experimentation that as the working distance increases the analysed corneal area is reduced.

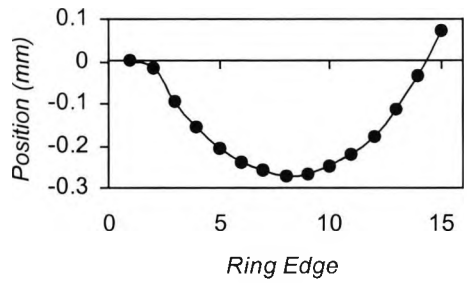

Figure 6.1 - Best focus position from the paraxial plane (0 mm) for 15 image ring edges for the best cylinder.

6.2 *Influence of faceplate design on radius of curvature maps*

Analysis of Figure 5.1 shows large sagittal radii errors for all surfaces until ring edge 4. From ring edge 5 only surfaces 4 and 5 present errors outside the ±0.02 mm tolerances. The large central error is due to the defocusing of the central rings, resulting in incorrect ring mire image edge position. Since these curves were calculated for the best focus based on the minimum blur sum, this shifts the focus to the intermediate rings. The central and peripheral rings will be out of focus. However focusing errors in the smaller mires (central) and hence errors in edge position will have a bigger effect than in larger mires (peripheral). The same amount of error will represent a substantial percentage of a smaller ring mire image height and a smaller percentage of a large mire.

Analysis of Figure 5.2 shows large tangential radii errors for all surfaces for central and peripheral rings, while intermediate rings display less error. Central ring errors result from the same causes specified for sagittal error. Peripheral ring errors are due to the method used by the van Saarloos algorithm to calculate tangential radius of curvature. It considers that three consecutive corneal points share the same centre of curvature (see section 3.15.2) to obtain surface smoothness. However in an aspheric surface (with $p<1$) the centre of curvature for peripheral points is different for each points and gets progressively further away from the surface axis. This fact explains the larger error for outer rings.

On Figure 5.3 the image plane was changed from best focus to focus on the inner edge of the first ring mire image. This leads to an accurate edge position resulting in an accurate apical radius calculation for all surfaces. This shift in focus increases the blur for peripheral points. However it doesn't result in a clinically significant error increment when compared to Figure 5.1. This finding suggests that focusing at the first ring mire image inner edge is better than focusing at the best focus position. An interesting effect, magnified by the scale change, is the oscillation of the graphs. It can be explained by the effect of focus on consecutive ring edges. The image of the inner ring edge of an image ring will look smaller when out of focus, while the image of the outer edge will look larger. This results in a decrease and an increase in the calculated radius of curvature respectively.

Figure 5.4 shows that once again the tangential radius of curvature error is larger than the sagittal radius of curvature error. The error also increases to the peripheral points for the reasons explained earlier. It can also be concluded that the large tangential radius error is not caused by focus but by the algorithm itself. It is also interesting to note that surface 1 does not seem to be affected by this algorithm error that leads to an tangential radius of curvature error increment for the peripheral rings.

Figure 5.5 displays the sagittal radius of curvature error for a smaller pupil with image plane at best focus. With the exception of a few points the error curves are very similar to the ones in Figure 5.1, for a 9 mm pupil with best focus. This suggests that aberrations (controlled by the instrument pupil size) play a minor role on radius of curvature error when compared to focusing errors.

Figure 5.6 (4 mm pupil) also shows that with the exception of a few points, the tangential radius of curvature error is similar to the tangential radius error for a 9 mm pupil displayed on Figure 5.2.

As to the influence of faceplate design on radius of curvature maps, analysis of all data shows that different faceplate designs will lead to clinically significant differences. Although the curves displayed do not show differences directly they represent them, since the radius error for the same point in each curve results from the subtraction of the calculated radius of curvature from the accurate radius of curvature. The accurate radius of curvature for each curve point is the same for all curves at that point.

6.3 *Effect of reflecting surface decentration on radius of curvature maps*

Analysis of Figure 5.7 to Figure 5.11 shows that the errors are larger in the direction of decentration (horizontal) and smaller towards the direction perpendicular to the decentration (vertical). In the 90° semi-meridian the sagittal radius error is very similar to the sagittal radius error of a centred surface. Comparison of sagittal radius errors for the opposite semi-meridians in the decentration direction, 0° and 180°, shows a sign change. The error is positive for the 0° semi-meridian and negative for the 180° semi-meridian. Since the error is given by exact-calculated sagittal radius of curvature the sagittal radius of curvature values are smaller for the 0° semi-meridian and larger for the 180° semi-meridian. This implies that ring crowding occurs for the semi-meridian of decentration (0°) and ring spacing for the opposite semi-meridian. These findings confirm the observations of Rowsey and Isaac (1983) and Legeais et al. (1993) but are in opposition to the observations of Wang et al. (1991) (see section 2.5).

Comparison of the error graph peaks for the 0 and 180° semi-meridians (Figure 5.7 and Figure 5.11 respectively) also shows that from ring edges 3 to 13 (marked by the open dots, starting at 0 for the first dot) the two graphs are in phase. This means that peaks and valleys are observed at the same ring edges on opposite semi-meridians. This is due to the effect of focus on the image ring edges, already mentioned on section 6.2. Inner (odd) ring edges get smaller and outer (even) edges get larger when out of focus. Ring edges 1, 2, 14 and 15 are not affected since they are near best focus (see Figure 6.1).

Figure 5.7 and Figure 5.11 show that a decentration as small as 0.5 mm greatly increases the sagittal radius error and that this error is magnified for the image ring edges out of focus.

6.4 *Effect of reflecting surface tilt on radius of curvature maps*

Analysis of Figure 5.12 to Figure 5.16 shows that the errors are larger in the direction of tilt (horizontal) and smaller towards the direction perpendicular to the tilt (vertical). In the 90° semi-meridian the sagittal radius error is very similar to the sagittal radius error of a centred surface. Comparison of sagittal radius errors for the opposite semi-meridians in the tilt direction, 0° and 180°, shows a shift on opposite directions from the centred surface error. The error is more negative than the centred surface error for the 0° semi-meridian and more positive than the centred surface error for the 180° semi-meridian. Since the error is given by exact-calculated sagittal radius of curvature the sagittal radius of curvature values are larger for the 0° semi-meridian and smaller for the 180° semi-meridian. This implies that ring spacing occurs for the semi-meridian of tilt (0°) and ring crowding for the opposite semi-meridian. Although it seems that tilting had the opposite effect of decentration it really has the same effect. After the surface was tilted it had to be realigned by a decentration in the 180° semi-meridian. Such decentration will have the described effect; ring crowding in the 180° semi-meridian and ring spacing in the 0° semi-meridian.

Comparison of the error graphs for the 0 and 180° semi-meridians (Figure 5.12 and Figure 5.16) also shows that although the sagital radius error is similar for the tilted and centred surfaces, the difference between both errors progressively increases towards the peripheral ring edges. This effect wasn't observed for the decentration and might be a characteristic of the image formed by a tilted surface.

In summary, the best faceplate design produced the smallest minimum blur sum of all surfaces due to its unique distribution of best focus for each individual object point. The best focus for the points near the surface centre and on the surface periphery have best focus positions on the paraxial plane with the intermediate points best focus shifted from that position.

Focus has more influence on sagittal radius error since it produces a change on the edges of the image ring mires. This change has a larger effect for the smaller mires that's why the apical radius of curvature calculation is very influenced by focus. Since the determination of the sagittal radius of curvature for one point is dependent on the radius for the previous point (arc step method), if the inner points have less error the outer points will follow the same trend decreasing overall error. The tangential radius of curvature error is less dependent on focus and aberrations since there is a problem in Klyce's procedure to calculate it. It considers that 3 surface points in a semi-meridian can be joined by a single circular arc, thus sharing a common centre of curvature. That is not true for a conoid that's why the error is large.

The ring asymmetry presented in decentration with ring crowding in the semi-meridian of decentration, ring spacing in the opposite semi-meridian and little change in the perpendicular semi-meridian can be used to detect decentration in a videokeratoscopic image.

The ring asymmetry for surface tilt is similar to the decentration pattern since a decentration has to be applied in order to achieve alignment. The only difference was that the error increased towards peripheral rings. In the future this findings may be used to predict surface tilt from videokeratoscopic images.

The next chapter summarises the main conclusions of the research project and comments on future work.

7 Conclusions

The surface that provides the sharpest image for an average cornea is a cylinder with base 120-mm away from the corneal vertex and a diameter of 26-mm. Increasing the working distance improves image quality but decreases the analysed corneal area. A balance must be found to provide optimum results.

These results don't show that any cylindrical faceplate provides better results than any other geometry. We can only conclude that this particular cylinder at the specified working distance is the best design. In this section of the work better results mean that the sums from the blurs of all image points are smaller, which means a sharper image.

Focusing errors have a major effect on radius of curvature errors. Focusing on the image of the first ring edge results in an accurate calculated reflecting surface apical radius and a smaller overall error when compared with best focus.

The instrument pupil aperture, which controls aberrations, has a negligible effect on overall radius of curvature error when compared to focusing errors. Although not tested, it is reasonable to assume that focusing at the inner rings associated with a smaller pupil will result in a smaller error. This is due to the fact that the van Saarloos algorithm uses a pinhole camera approach. However the pupil cannot be too small, the finite wavelength of light and the small numerical aperture will result in significant diffraction (Charman 1972). Therefore reducing the instrument pupil size below a certain level may decrease accuracy.

The method used by the van Saarloos algorithm to calculate the tangential radius of curvature is not adequate for peripheral points.
Sagittal radius of curvature errors are larger in the direction of decentration and smaller towards the direction perpendicular to the decentration. In the latter direction the sagittal radius error is very similar to the sagittal radius error of a centred surface. Ring crowding occurs for the semi-meridian of decentration and

ring spacing for the opposite semi-meridian. Oscillation of the sagittal radius error curves is apparent for image ring edges out of focus. The sagittal radius error due to decentration is also larger for image ring edges out of focus.

When the reflecting surface is tilted it has to be translated in order to fulfil the alignment conditions (see section 3.11). This shift can be considered a decentration since the reflecting surface apex has to be moved away from the instrument axis. In this sense the ring crowding effect is the same observed in a decentred surface. The effect of tilt is also smaller in the direction perpendicular to the tilt. The difference between sagittal radius errors for the tilted and the centred surface increases towards the peripheral rings.

The observations for tilt and decentred surfaces were based on a single faceplate design and reflecting surface. They were meant to display the capabilities of the videokeratoscope simulation program and not as a complete research on the subject. To validate the findings other faceplate designs and reflecting surfaces would have to be tested.

The main part of this research was the development of a videokeratoscope computer model. It allows handling tilted and decentred reflecting surfaces and also considers the irradiance distribution across ring mire images. Novel aspects include a new ray tracing method for tilted surfaces, retracing a bundle of rays of higher density using the previous results and determining irradiance distribution taking into account the influence of adjacent object points.

According to Klyce (2001), the future of corneal analysis seems to point in the direction of aberrometry. At some point in time videokeratoscopes will no longer be used. However it will take many years for that to happen therefore this research work is still very up to date. Videokeratoscopes present many advantages over keratometers but these are still the most widely used instrument for corneal

analysis by clinicians. This is probably due to the low cost when compared to a videokeratoscope.

Surprisingly in 2002 there has been virtually no new research papers in tilt, decentration and defocus on videokeratoscopes. No new algorithms for Placido disk systems have been published either. There is still a lot to be done in this area since the only theoretical tilt correction algorithms have been developed for telecentric systems and the videokeratoscopes don't belong to that class. The simulation program developed in this research project will aid in the development and testing of correction algorithms, which can be applied to non-telecentrical systems.

8 Bibliography

- Andersen, J., Koch-Jensen, P., and Osterby, O. (1993a). Corneal topography: Photokeratoscopy including the central region. *Acta Ophthalmologica* 71(2):145-150.
- Andersen, J., Koch-Jensen, P., and Osterby, O. (1993b). Corneal topography: Image-processing and numerical analysis of keratoscopy. *Acta Ophthalmologica* 71(2):151-159.
- Applegate, R.A. and Howland, H.C. (1995). Noninvasive measurement of corneal topography. *Ieee Engineering In Medicine And Biology Magazine* 14(1): 30-42.
- Baker, T.Y. (1943). Ray tracing through non-spherical surfaces. *Proceedings - Physical Society* 55:361-364.
- Bennett, A.G. (1988). Aspherical and continuous curve contact lenses. *Optometry Today* 28(1):11-14.
- Bers (1969). Calculus. (New York: Holt, Rinehart and Winston inc: 732).
- Binder, P.S.(1995) Videokeratography. *the CLAO Journal* 21(2):133-144.
- Borowski, E.J.; Borwein, J.M. (1989). Collins dictionary of Mathematics (UK: Harper Collins publishers).
- Brenner, D. (1997). Modelling the cornea with the Topographic Modeling System videokeratoscope. *Optometry And Vision Science* 74(11):895-898.
- Busin, M., Wilmanns, I., and Spitznas, M. (1989). Automated corneal topography: computerised analysis of photokeratoscope images. *Graefe's archives of Clinical and Experimental Ophthalmology* 227:230-236.
- Campbell, C. (1997). Reconstruction of the corneal shape with the MasterVue Corneal Topography System. *Optometry And Vision Science* 74(11):899-905.
- Chan, J.S. and Mandell, R.B. (1997). Alignment effects in videokeratography of keratoconus. *The CLAO Journal* 23(1):23-28.
- Chapra, S.C.; Canale, R.P. (1988). Numerical methods for engineers (2nd Edition) New York: McGraw-Hill book company: 478-489.

- Charman, W.N. (1972). Diffraction and the precision of measurement of corneal and other small radii. *American Journal of Optometry* 49(8):672-680.
- Clark, B.A.J. (1973). Less common methods of measuring corneal topography. *Autralian Journal of Optometry* 56:182-192.
- Doss, J.D., Hutson, R.L., Rowsey, J.J. and Brown, D.R. (1981). Method for calculation of corneal profile and power distribution. *Archives Of Ophthalmology* 99(7):1261-1265.
- Douthwaite, W.A., Pardhan, S., and Burek, H. (1996). Extent and effect of surface tilt on the data display of the Eyesys videokeratoscope. *British Journal Of Ophthalmology* 80:986-993.
- Douthwaite, W.A. and Pardhan, S. (1998). Surface tilt measured with the EyeSys videokeratoscope: influence on corneal asymmetry. *Investigative Ophthalmology & Visual Science* 39(9):1727-1735.
- Edmund, C. and Sjontoft, E. (1985). The central-peripheral radius of the normal corneal curvature. A photokeratoscopy study. *Acta Ophthalmologica* 63(6):670-677.
- Edwards, J.E. (1930). A treatise on the integral calculus. (London: MacMillan and co., limited).
- Eghbali, F., Yeung, K.K., Maloney, R.K. (1995). Topographic determination of corneal asphericity and its lack of effect on the refractive outcome of radial keratotomy. *American Journal of Ophthalmology* 119(3):275-280.
- El Hage, S. (1971). Suggested new methods for photokeratoscopy a comparison for their validities. Part I. *American Journal of Optometry and Archives of the American Academy of Optometry* 48(11):897-912.
- El Hage, S.G. (1972). Differential equation for the use of the diffused ring photokeratoscope. *American Journal of Optometry and Physiological Optics* 49(5):422-436.
- El Hage, S.G. (1989) A computerised corneal topographer for use in refractive Surgery. *Refractive & Corneal Surgery* 5(6):418-424, 1989.
- Fincham, E.F. (1953). The photo-keratoscope. *Medical and Biological Illustration* 3:87-93.

- Fisher, K.D. and Applegate, R.A. (1990). Test re-test reliability of a new topographic modelling system using known surfaces. *Investigative Ophthalmology & Visual Science (supplement)* 31(4):479.
- Fowler, C.W. and Dave, T.N. (1994) Review of past and present techniques of measuring corneal topography. *Ophthalmic and Physiological Optics* 14(1):49-58.
- Freeman, D.E.L. (1990). A simple method for finding the valid ray-surface intersection. *In: International lens design conference*. SPIE, Vol 1354, pp 200-209.
- Fry, G.A. (1975). Analysis of photometric data. *American Journal of Optometry and Physiological Optics* 52(5):305-312.
- Gersten, M., Mammone, R.J., and Zelvin, J.L. (1989). System for topographical modelling of anatomical surfaces. US patent N 4863260.
- Gills, J.P.; Sanders, D.R.; Thornton, S.P.; Martin, R.G.; Gayton, J.L.; Holladay, J.T. and Van Der Karr, M. (1995). Corneal topography: the state of the art (USA: Slack incorporated).
- Gormley, D.J., Gersten, M., Koplin, R.S., and Lubkin, V. (1988). Corneal modelling. *Cornea* 7(1):30-35.
- Goss,D.A. (1991). Keratoscopy. In: Clinical procedures in Optometry, edited by Eskridge,J.B. ; Amos, J.F. and Bartlett,J.D. (Philadelphia: J.B. Lippincott Company).
- Grieve, B.A. (1926). Analytical geometry of conic sections and elementary solid figures, Part I (London: G.Bell and sons, ltd).
- Guillon, M.; Lydon, D.P.M. and Wilson, C. (1986). Corneal topography: A clinical model. *Ophthalmic & Physiological Optics* 6(1): 47-56.
- Gullstrand, A. (1966). Photographic-ophthalmometric and clinical investigations of corneal refraction. *American Journal of Optometry and Archives of the American Academy of Optometry* 43(3):143-214. (Translation by William M. Ludlam from the German original written in 1896).
- Halstead, M.A., Barsky, B.A., Klein, S.A. and Mandell, R.B. (1995) A spline surface algorithm for reconstruction of corneal topography from a

videokeratographic reflection pattern. *Optometry And Vision Science* 72(11):821-827.

- Hannush, S.B., Crawford, S.L., Waring III, G.O., Gemmil, M.C., Lynn, M.J., and Nizam, A. (1989) Accuracy and precision of keratomery, photokeratoscopy, and corneal modeling on calibrated steel balls. *Archives Of Ophthalmology* 107(8):1235-1239.
- Hecht, E. (1998). Optics. 3rd Edition Addison Wesley Longman, Inc, Massachusetts: 267-268.
- Higaki, S., Maeda, N., Watanabe, H., Inoue, Y., and Shimomura, Y. (1997). The efficacy of automated misalignment correction in videokeratography. *Investigative Ophthalmology & Visual Science (supplement)* 38(4):s849.
- Hilmantel, G., Blunt, R.J., Applegate, R.A., and Howland, H.C. (1997). Accuracy with which the TMS-1 can measure elevations of asymmetric surfaces. *Investigative Ophthalmology & Visual Science (supplement)* 38(4):s850.
- Hilmantel, G., Blunt, R.J., Garrett, B.P., Howland, H.C., and Applegate, R.A. (1999) Accuracy of the Tomey topographic modeling system in measuring surface elevations of asymmetric objects. *Optometry And Vision Science* 76(2):108-114.
- Hubbe, R.E. and Foulks, G.N. (1994). The effect of poor fixation on computer-assisted topographic corneal analysis - pseudokeratoconus. *Ophthalmology* 101(10):1745-1748.
- Kiely, P.M., Smith, G., Carney, L.G. (1982). The mean shape of the human cornea. *Optica Acta* 29(8):1027-1040.
- Klein, M. (1958). A new keratoscope with self-luminous Placido disk. *British Journal of Ophthalmology* 42:380-381.
- Klein, S.A. (1992). A corneal topography algorithm that produces continuous curvature. *Optometry And Vision Science* 69(11):829-834.
- Klein, S.A. (1997). Axial curvature and the skew ray error in corneal topography. *Optometry And Vision Science* 74(11):931-944.

- Klyce, S.D. (1984). Computer-assisted corneal topography - High-resolution graphic presentation and analysis of keratoscopy. *Investigative Ophthalmology & Visual Science* 25(12):1426-1435.
- Klyce, S.D. (2001). Fundamentals of topography and aberrometry. *Journal of Refractive Surgery* 17(2):265.
- Knoll, H.A. (1961) Corneal contours in the general population as revealed by the photokeratoscope. *American Journal of Optometry Archives of the American Academy of Optometry* 38:389-397.
- Laskin, A.V. and Puryayev, D.T. (1995). New keratoscope optical system. *Optics And Laser Technology* 27(3):157-162.
- Legeais, J.M., Ren, Q., Simon, G., and Parel, J.M. (1993). Computer-assisted corneal topography: Accuracy and reproducibility of the Topographic Modelling System. *Refractive And Corneal Surgery* 9:347-357.
- Levene, J.R. (1962). An evaluation of the hand held keratoscope as a diagnostic instrument for corneal astigmatism - Part II. *British Journal of Physiological Optics* 19(4):237-251.
- Levene, J.R. (1965). The true inventors of the keratoscope and the photokeratoscope. *British Journal of the History of Science* 2(8):324-342.
- Lindsay, R.; Smith, G. and Atchison, D (1998). Descriptors of corneal shape. *Optometry And Vision Science* 75(2):156-158.
- Longhurst, R.S. (1973) Geometrical and Physical Optics. 3rd Edition Longman Scientific and Technical, England: 406-407
- Ludlam, W.M. and Wittenberg, S. (1966a) Measurement of the ocular dioptric elements utilising photographic methods, Part II Cornea - Theoretical considerations. *American Journal of Optometry* 43:249-267.
- Ludlam, W.M. and Wittenberg, S. (1966b). The effect of measuring corneal toroidicity with reference to the line of sight. *British Journal of Physiological Optics* 23:178-185.
- Mammone, R.J., Gersten, M., Gormley, D.J., Koplin, R.S. and Lubkin, V.L. (1990) 3-D Corneal modelling system. *IEEE Transactions Biomedical Engineering* 37(1):66-72.

- Mandell, R.B. and St.Helen, R. (1971) Mathematical model of the corneal contour. *British Journal of Physiological Optics* 26:183-197.
- Mandell, R.B. (1992) The enigma of the corneal contour. *the CLAO Journal* 18(4):267-272.
- Mandell, R.B., Horner, D.G., Soni, P.S., Heath, G.G., Gerstman, D.R., and Wheeler, W.H. (1992). Alignment errors in video keratoscopy. *Investigative Ophthalmology & Visual Science (supplement)* 33(4):993.
- Mandell, R.B (1994). Apparent pupil displacement in videokeratography. *the CLAO Journal* 20(2):123-127.
- Mandell, R.B., Chiang, C.S., and Klein, S.A. (1995). Location of the major corneal reference points. *Optometry And Vision Science* 72(11):776-784.
- Mandell, R.B., Chiang, C.S., and Yee, L. (1996). Asymmetric corneal toricity and pseudokeratoconus in videokeratography. *Journal of the American Optometric Association* 67(9):540-547.
- McCarey, B.E., Zurawski, C.A., and O'Shea, D.S. (1992). Practical aspects of a corneal topography system. *the CLAO Journal* 18(4):248-254.
- Mejia-Barbosa, Y. and Malacara-Hernandez, D. (2001) A review of methods for measuring corneal topography. *Optometry And Vision Science* 78(4):240-253.
- Mellinger, M.D., Greivenkamp, J.E., Snyder, R.W., Bechara, S., Schwiegerling, J.T., Lowman, A.E., Miller, J.M., and Palmer, M.L. (1993). Toric surface measurement comparison of the Computed Anatomy and EyeSys laboratories videokeratoscopes. *Investigative Ophthalmology & Visual Science (supplement)* 34(4):1252.
- Munnerlyn, A., Tang, V., and Shimmick, J. (2000). Measurement of decentred features by corneal topography. *Investigative Ophthalmology & Visual Science (supplement)* 41(4):s678.
- Nieves, J.E. and Applegate, R.A. (1992). Alignment errors and working distance directly influence the accuracy of corneal topography measurements. *Investigative Ophthalmology & Visual Science (supplement)* 33(4):993.
- Oltrup, T., Jean, B., and Bende, T. (1997). Automated compensation of defocusing errors in videokeratography. *The CLAO Journal* 23(3):157-160.

- Penney, C.M., Maloney, R.K., Gailitis, R.P., Thompson, K.P., and Warring III, G.O. (1990). Sensitivity of videokeratoscopy to errors in centration and focusing. *Investigative Ophthalmology & Visual Science (supplement)* 31(4):479.
- Plácido, A. (1880a) Novo instrumento de exploração da córnea. *Periódico de Oftalmologia Prática* 2(2):27-30.
- Plácido, A. (1880b) Novo instrumento para análise imediata das irregularidades de curvatura da córnea. *Periódico de Oftalmologia Prática* 2(5):44-49.
- Plácido, A. (1881). Alterações de simetria da superficie da córnea. *Periódico de Oftalmologia Prática* 3(1):41-55.
- Press, W.H., Teukolsky, S.A., Vetterling, W.T., Flannery, B.P.(1992). Numerical recipes in C: the art of scientific computing.(2nd edition Cambridge: Cambridge University Press: 129-138).
- Rabinowitz, Y.S., Garbus, J., and Mcdonnell, P.J. (1990) Computer-assisted corneal topography in family members of patients with keratoconus. *Archives Of Ophthalmology* 108(3):365-371.
- Rabinowitz, Y.S., Garbus, J.J., Garbus, C., McDonnell, P.J. (1991) Contact lens selection for keratoconus using a computer assisted videokeratoscope. *CLAO Journal* 17(2):88-93
- Rabinowitz, Y.S. (1995) Corneal Topography. *Current Opinion in Ophthalmology* IV(6):57-62.
- Rand, R.H., Howland, H.C., and Applegate, R.A. (1997). Mathematical model of a Placido disk keratometer and its implications for recovery of corneal topography. *Optometry And Vision Science* 74(11):926-930.
- Reynolds, A.E. and Kratt, H.J. (1959), The photo-electronic keratoscope. Contacto 3(3):53-59.
- Roberts, C. (1994a). Characterisation of the inherent error in a spherically-biased corneal topography system in mapping a radially aspheric surface. *Journal Of Refractive And Corneal Surgery* 10:103-116.

- Roberts, C. (1994b). The accuracy of 'power' maps to display curvature data in corneal topography systems. *Investigative Ophthalmology & Visual Science* 35(9):3525-3532.
- Roberts, C. (1996). Corneal topography: A review of terms and concepts. *Journal Of Cataract And Refractive Surgery* 22:624-629.
- Rowsey, J.J., Reynolds, A.E., and Brown, R. (1981). Corneal topography - corneascope. *Archives Of Ophthalmology* 99(6):1093-1100.
- Rowsey, J.J ; Isaac, M.S (1983). Corneoscopy in keratorefractive surgery. *Cornea* 2(2):133-142.
- Sayegh, S.I., Hart, J.D., Juhasz, T., and Kurtz, R.M. (1998). Correction of focus errors in videokeratoscopy. *Investigative Ophthalmology & Visual Science (supplement)* 39(4):s1111.
- Smith, W.J. (1966). Modern Optical Engineering. (New York: McGraw-Hill: 393).
- Stone, J. (1962) The validity of some existing methods of measuring corneal contour compared with suggested new methods. *British Journal of Physiological Optics* 19:205-230.
- Suchecki, J.K., Ehlers, W.H., and Donshik, P.C. (1995). Poor fixation and focus result in artifactual readings in computerised corneal topography. *Investigative Ophthalmology & Visual Science (supplement)* 36(4):s304.
- Szczotka, L.B. (1997) Evaluation of a topographically based contact lens fitting software. *Optometry and Vision Science* 74(1): 14-19.
- Townsley, M.G. and Ridge III, P. (1967). New equipment and methods for determining the contour of the human cornea. *Contacto* 11:72-81.
- Townsley, M.G. (1970). New knowledge of the corneal contour. *Contacto* 14:38-43.
- Uozato, H. and Guyton, D.L. (1987). Centring corneal surgical procedures. *American Journal Of Ophthalmology* 103(2):264-275.
- van Saarloos, P.P. and Constable, I.J. (1991). Improved method for calculation of corneal topography for any photokeratoscope geometry. *Optometry And Vision Science* 68(12):960-965.

- Wang, J., Rice, D.A., and Klyce, S.D. (1989). A new reconstruction algorithm for improvement of corneal topographical analysis. *Refractive and Corneal Surgery* 5:379-387.
- Wang, J., Rice, D.A., and Klyce, S.D. (1991). Analysis of the effects of astigmatism and misalignment on corneal surface reconstruction from photokeratoscopic data. *Refractive and Corneal Surgery* 7:129-140.
- Waring III, G.O. (1989). Making sense of keratospeak II: Proposed conventional terminology for corneal topography. *Refractive & Corneal Surgery* 5:362-367.
- Welford, W.T. (1986). Aberrations of optical systems. (Bristol and Boston: Adam Hilger Ltd.)
- Wilson, S.E., Verity, S.M., and Conger, D.L. (1992) Accuracy and precision of the corneal analysis system and the topographic modelling system. *Cornea* 11(1):28-35.
- Wittenberg, S. and Ludlam, W.M. (1966). Derivation of a system for analysing the surface from photokeratoscopic data. *Journal of the Optical Society of America* 56(11):1612-1615.
- Wittenberg, S. and Ludlam, W.M. (1970). Planar reflected imagery in photokeratoscopy. *Journal of the Optical Society of America* 60(7):981-985, 1970.